The influence of glacial boundary conditions on the climate system during the Last Glacial Maximum

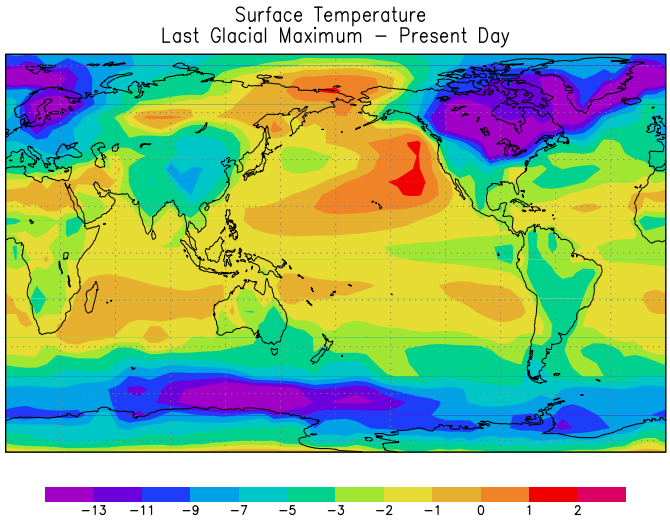

Dissertation
zur Erlangung des Doktorgrades
der Mathematisch-Naturwissenschaftlichen Fakultät
der Christian-Albrechts-Universität
zu Kiel

vorgelegt von
Flávio Barbosa Justino
aus
São Paulo-Brasilien

Kiel, April 2004

ABSTRACT

The aim of this thesis is to explore and understand some major climate mechanisms that were responsible for atmospheric and oceanic changes during the LGM (21,000 years ago).

A coupled global atmosphere ocean model of intermediate complexity is used to study the influence of glacial boundary conditions on the climate system during the LGM in a systematical manner. A web of atmospheric interactions is disentangled which involves changes of the meridional temperature gradient and an associated modulation of the atmospheric baroclinicity. This in turn drives anomalous transient eddy momentum flux which feedback onto the zonal mean circulation. Moreover, the modified transient activity, weakened (strengthened) in the North Pacific (Atlantic), leads to a meridional re-organization of the atmospheric heat-transport, thereby feeding back to the meridional temperature structure.

Furthermore, it is argued that modifications of the large-scale atmospheric circulation during the LGM may have led to a slowdown of the Pacific subtropical gyre as well as to an intensification of the Pacific subtropical cell. These oceanic circulation changes generate an eastern North Pacific warming, an associated cooling in the Kuroshio area, as well as a cooling of the tropical oceans, respectively. The tropical cooling pattern resembles a permanent La Niña state which in turn forces atmospheric teleconnection patterns that lead to an enhancement of the subtropical warming by reduced latent and sensible cooling of the ocean. In addition, the radiative cooling due to atmospheric CO_2 and water vapour reductions imposes a cooling tendency in the tropics and subtropics, thereby intensifying the permanent La Niña conditions. Hence, a delicate balance between oceanic circulation changes, remotely induced atmospheric flux anomalies as well as local radiative cooling is established which controls the tropical and the North Pacific temperature anomalies during the LGM.

The LGM simulation exhibits an intensified Atlantic overturning cell, associated with an enhanced formation of North Atlantic Deep Water. This enhancement can be attributed to the strong surface cooling in high latitudes and brine release in areas of seasonally varying sea-ice extent. In turn, the intensified meridional overturning circulation leads to an enhanced poleward heat transport that is required to equilibrate the strong tropical-extratropical temperature contrast during the LGM. The modeling results compare well with some recent paleoreconstructions.

ACKNOWLEDGEMENTS

I would like to express my gratitude to Dr. Axel Timmermann and Prof. Dr. Jürgen Willebrand, for giving me the opportunity to carry out this study at the Leibniz Institute of Marine Research. Furthermore, I am very grateful to Prof. Dr. Friedrich Schott for his overall support.

I wish to thank all my collegues for stimulating and pleasant atmosphere at the Institute of Marine Research. Especially, Drs. Jan Abshagen, Ute Merkel, Oliver Timm, Noel Keenlyside and Uta Krebs for stimulating discussions, their valuable suggestions and scientific advice. I can not forget to thank my wife, Vânia, for her never ending patience, encouragement, and support throughout all the highs and lows.

This work was supported by CAPES-Brasilia, Grant 0794023 and by the Deutsche Forchungsgemeinschaft (DFG) through the collaborative research project.

CONTENTS

LIST OF FIGURES

LIST OF TABLES

1. INTRODUCTION

How much was the world cooling in the distant past?
How much is the world warming?
(IPCC 2001)

1.1 Why paleo-modeling?

The past 10,000 years have been anomalous in the history of our planet. This period, during which civilisation developed, was marked by reduced global climate variability, unlike during any similar time span of the past 100 millennia *(Broecker 1995a)*. High-resolution records from ice and sediments cores and other sources have revealed that in the past rapid climate changes occurred at the time-scale of human lives. Some of the most pronounced regional and large-scale climate changes (involving, for example, a regional change in mean annual temperature of several degrees Celsius or dramatic changes in precipitation patterns) occurred within a few centuries, and often within a few decades, or even just within a few years *(Alley 2000; Peterson et al. 2000; Haug et al. 1998; Dansgaard et al. 1993)*. As documented by records from early civilisations these decadal-time-scale transitions had a strong impact on human living and societies. For instance, the collapse of the Mayan civilisation which occurred around 800 years before present (BP) can be attributed to decadal-scale climate shifts *(Haug et al. 2001; Hodell 1995)*. It has also been suggested that alternating wet and dry periods influenced the rise and fall of coastal and highland cultures of Ecuador and Peru *(Thompson et al. 1995)*. As suggested by *Seidov et al. (2001)*, these sudden climate transitions are also a threat scenario for our future climate, which is expected to be significantly different than today's climate due to anthropogenic emissions of greenhouse gases *(IPCC 2001)*.

Currently, there is evidence for a global warming trend which many scientists consider to be a witness of anthropogenic climate changes. Other researchers, however, argue that the same trend is a natural adjustment of the global climate system recovering from the Little Ice Age, the last major climate deterioration that ended 100 years ago *(Seidov and Maslin 2001)*.

Although state-of-the-art coupled general circulation models (CGCM) are able to realistically simulate both the present annual mean climate and the climatological seasonal cycle, an accurate simulation of current climate does not guarantee the ability of a model to simulate past or future climate changes properly. Climate models have been successful in simulating climate trends since 1850 assuming a combination of greenhouse gas, aerosol and solar forcing, but these changes are fairly small compared to many projections of climate change of the 21st century, as addressed by the *IPCC*

(2001). An important motivation to simulate the past climatic conditions is that such experiments provide opportunities for evaluating how models respond to large changes in forcing. This may help to assess the validity of future climate forecasts.

By simulating past climates we can also increase our understanding of mechanisms of climate change. For example, the climate of the Last Glacial Maximum (*LGM*) (about 21kyr ago) is an interesting test case to study the importance of climate feedbacks. During the *LGM*, land characteristics were different from those observed today. The atmospheric CO_2 concentration was about 150 ppm less than today's and the global surface albedo differed from today due to the increased sea ice area, the presence of ice caps and a different vegetation pattern. The extent of sea ice represents one of the most variable and sensitive parameters of the global climate system because it strongly influences the amount of reflected solar radiation and the exchanges of heat, mass and momentum between ocean and atmosphere in high latitudes *(Budyko 1969; Saltzman 1983)*. Therefore, the understanding of, for instance, the sea ice-albedo feedbacks during the *LGM* is an important component towards an assessment of potential future climate changes.

Furthermore, the coupled atmosphere-ocean system in the tropics has been very sensitive to changes in wind direction and strength due to the presence of atmosphere-ocean instabilities *(Philander 1985)*. At the heart of this coupling is the El-Niño Southern Oscillation (ENSO) phenomenon. *Sarnthein et al. (1981)* and *Molina-Cruz (1977)* documented evidence for stronger equatorial Pacific trade winds during the *LGM*, which in turn probably triggered a distinct equatorial air-sea coupling. Thereby, paleoclimate simulations can help to gain a deeper understanding of the prominent processes acting in the tropical atmosphere-ocean system. This has been illustrated in a recent study by *An et al. (2003)*. In this study it was found that the *LGM* background supported large-amplitude self-sustained inter-annual ENSO variations in the tropical Pacific. In addition, their analyses indicated that off-equatorial climate conditions as well as a shoaling of the thermocline play a crucial role in amplifying the *LGM* ENSO mode. Paleo studies also enable us to disentangle the mechanisms of rapid climate changes and millennial-scale oscillations inferred from paleodata and ice cores. Modeling simulations also indicate that oscillations of this type may be triggered by greenhouse warming *(Knutti and Stocker 2002)*.

1.2 A Brief of Earth's Climate History: The Last 100 kyr

Centennial to millennial scale changes in global climate over the last 100 kyr were discovered for the first time in the Greenland Ice Core Project, (GRIP) *(Dansgaard et al. 1993; 1989; 1984)*. Further analyses revealed that instability mechanisms of the ice sheets around the North Atlantic and of the thermohaline circulation are prime candidates to trigger such changes *(Sarnthein et al. 2001; Broecker 1997; Oeschger et al. 1984)*. The Earth's climate exhibited large and rapid climatic changes during the last glacial period occurring on millennial timescales *(Sarnthein et al. 2001; Grootes and Stuiver 1997)*. Temperature variations as derived from $\delta^{18}O$ records during the last glacial period changed considerably during the transition toward the present Holocene. Moreover, in glacial times temperatures were far more variable than today, although,

the amplitude of the glacial-interglacial temperature change (cold phases-warm phases) was lower in tropical and equatorial regions than in mid- and high latitudes *(McManus et al. 1999; Schneider et al. 1996; Rostek et al. 1993)*.

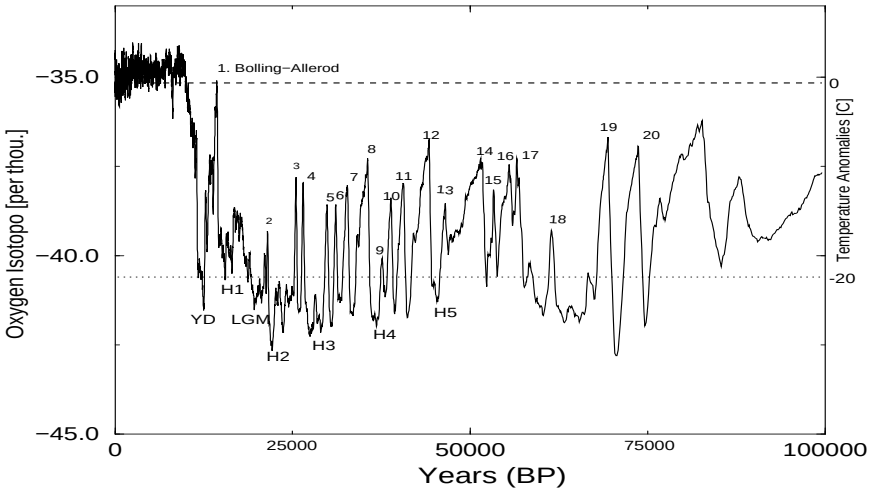

Fig. 1.1: *$\delta^{18}O$ record showing numbered interstadials (Dansgaard-Oeschger events), and Heinrich events (H1 to H5), and the Younger Dryas (YD). The approximate temperature range is given on the right. Data from GRIP ice core (Dansgaard et al. 1984).*

The series of rapid oscillations (Fig. 1.1) called Dansgaard-Oeschger events (D-O) (numbered labels in Figure 1.1) and Heinrich events (HE), were associated with local temperature changes over Greenland of up to 15°C *(Lang et al. 1999)* within a decade. Many of these swings in the climate system were not just a local phenomenon, but had global impact with evidence in South America *(Lowell et al. 1995)*, the North Pacific *(Kotilainen and Shackleton 1995)*, the Santa Barbara Basin *(Behl and Kennett 1996)*, the Arabian Sea *(Schulz et al. 1998)* and the South China Sea *(Wang 1999)*.

In between the HE there is variability of much higher frequency, with a timescale of about 1500 years *(Schulz et al. 2002; Bond et al. 1997; Dansgaard et al. 1993)*, the so-called Dansgaard-Oeschger events. These events are perhaps the most pronounced climate changes that occurred during the past 100 kyr.

Recently, several models have been used in order to explain the rapid temperature jumps during the last glacial period *(Claussen et al. 2003; Timmermann et al. 2003; Schulz et al. 2002; Ganopolski and Rahmstorf 2001; Paillard and Labeyrie 1994; MacAyeal 1993a,b; Broecker and Denton 1989; Broecker et al. 1985)*. So far, two main theories for the causes of the Heinrich and D-O events have been discussed. It has been suggested that either external forcing of the thermohaline circulation *(e.g. Claussen et al. 2003)* or internal instabilities of the Laurentide ice sheet or the thermohaline circulation *(Timmermann et al. 2003; MacAyeal 1993a,b)* may be responsible for the

generation of these events. Moreover, it has been established that low frequency climate fluctuations associated with orbital forcing between glacial and interglacial periods are controlled externally (e.g. *Imbrie et al. 1992; Imbrie et al. 1984; Berger 1988*). In addition, *(Broecker 1994; Hagelberg et al. 1994)* argued that there are harmonics of the orbital variations which correspond to the timing of the HE.

Broecker et al. (1985) attribute these climate shifts (D-O events) to the bistability of the thermohaline circulation. North Atlantic Deep Water is active during the warm phase whereas it is shutoff during cold phases, and some external/internal forcing causes mode switches between these two states. This idea is based on the bistability found in Stommel's classic model *(Stommel 1961)*. However, this hypothesis is at odds with more recent sediment data showing North Atlantic Deep Water formation during stadial (cold phases) and shutdown only during or after HE. A second hypothesis is associated to the shifts of convection between the Nordic Seas and the mid-latitude Atlantic Ocean *(Rahmstorf 1994)*. In this mechanism, the rapid warming phase results from a northward intrusion of warm water into the Nordic Seas. Some trigger is required to start the event. However, the exact nature of this trigger remains unknown. Another hypothesis does not involve the thermohaline circulation. *Clement et al. (2001)* highlighted the importance of orbitally-driven changes of the El Niño-Southern Oscillation phenomenon in triggering abrupt climate transitions in the extra-tropics. Via changes in the atmospheric planetary-wave pattern.

HE are the second major type of climatic event that occurred in the last ice age. They are characterised by large input of ice-rafted detritus to the North Atlantic ocean induced by iceberg discharges over the last 60 kyr *(Sarnthein et al. 2001; Bond et al. 1997; Bond and Lotti 1995; Labeyrie et al. 1995; Heinrich 1988)*. Detailed studies of the sequence of events in ocean sediments and ice cores showed that HE occurred on an average timescale of 7,200 $\pm$ 2400 calender years *(Sarnthein et al. 2001)* within the time interval between about 70 and 10.5 kyr.

One of the first approaches to explain the HE was put forward by *MacAyeal (1993a,b)*. It suggests that the temperature jumps were caused by internal instabilities of the Laurentide ice sheet. As the ice sheet expanded the geothermal heat from the Earth's crust together with heat due to friction of ice moving over ice, was trapped by the insulation effect of the overlying ice. When this occurred the sediment became soft, and thus lubrificated the base of the ice sheet causing a massive outflow of ice through the Hudson Bay. This, in turn, led to a sudden loss of ice mass, which reduced the insulating effect and led to re-freezing of the basal ice. According to *MacAyeal (1993a,b)*, this system of progressive ice build-up, melting and surge has an approximate periodicity of 7000 kyr, which is similar to the interval between the last five HE shown in the Figure 1.1.

Furthermore, it has been found in several modeling studies *(Timmermann et al. 2003; Bjornsson and Mysak 2001; Sakai and Peltier 1999; Winton and Sarachik 1993)* that centennial to millennial scale climate variability can be triggered by noise and internal oceanic process. The overall idea is that a stable stratified polar water column, for instance during a HE, becomes destabilised by advection/diffusion of warm subsurface water. Once deep convection triggered from below reinitiates, it increases the THC rapidly leading to a so-called THC flush. The third suggested cause of HE is

the destabilisation of the Laurentide ice sheet triggered by sea level changes induced by the 1500 years D-O cycles *(Sarnthein et al. 2001; van Kreveld 2000)*.

At the end of the last glacial (12,800-11,500 BP), a particularly interesting abrupt climatic change took place, the so-called Younger Dryas (YD) event. Air temperature had already warmed to near-interglacial conditions and continental ice sheets were retreated, when within a few decades the climate in the North Atlantic switched back to glacial conditions for more than thousand years. *Broecker (1995b)* argued that the retreat of the ice front associated with the interglacial opened a channel to the east, triggering a catastrophic drop in level of the Lake Agassiz, a very large lake trapped in the topographic depression created by the weight of the retreating ice cap in North America. The water released during this breakthrough flooded across Canada into the St. Lawrence River and discharged directly into the region of deep water formation. This could have caused a shutdown of the Atlantic thermohaline circulation. Alternatively, the Younger Dryas may simply have been the last cold stadial period of the glacial following a temporary D-O warming event, as addressed by *Schulz et al. (2002)*. During the present interglacial, the climate system has been much more stable than during the last glacial. However, one abrupt event appeared around 8200 yr as a cold spike in GRIP ice cores (Fig. 1.1).

One of the most important findings in the study of millennial-scale climate events is the out-of-phase climate response of the two hemispheres -the bipolar seesaw. This bipolar seesaw can be controlled by the atmosphere *(Broecker 1998; Webb et al. 1997)*, by the ocean *(Stocker, 1998, 1994)* or a combination of both *(Broecker 1998)*. *Broecker (2000)* suggests that for rapid climate changes to be initiated there must be a trigger for a sudden "switching off" or a strong decrease in the rate of deep water formation in either the North Atlantic or the Southern Ocean. This must be due to a decrease in the density of surface water. Changes of the density could result from changes in salinity (changes in fresh water) and/or increased temperatures *(e.g. Ganopolski and Rahmstorf 2001; Seidov and Maslin 2001; Dickson et al. 1998; Rahmstorf 1995)*.

Recently, *Maslin et al. (2001)* have proposed a combined hypothesis to explain the origin of abrupt climate jumps (Fig. 1.2). It is quoted below:

> *The meltwater associated with the D-O cold event could reduce the North Atlantic Deep Water (NADW), which in turn changes the direction of the hemispheric heat transport and thus the Southern Hemisphere warms up. This increased warmth in the Southern Hemisphere at some point triggers a melting of sea ice and/or a surging of the Antarctica ice sheets. This reverses the process reducing the Antarctic Bottom Water and hence strengthening the NADW. This in turns warms the North Atlantic and triggers another D-O melting event. Eventually after a certain number of D-O cycles the sea level rise associated with them would be significant to undercut the Laurentide ice sheet, causing a HE. The HE would then also influence the Southern Hemisphere and cause a further bipolar climate swing. Hence once initiated this deep water oscillating system could continue without need for any external influences.*

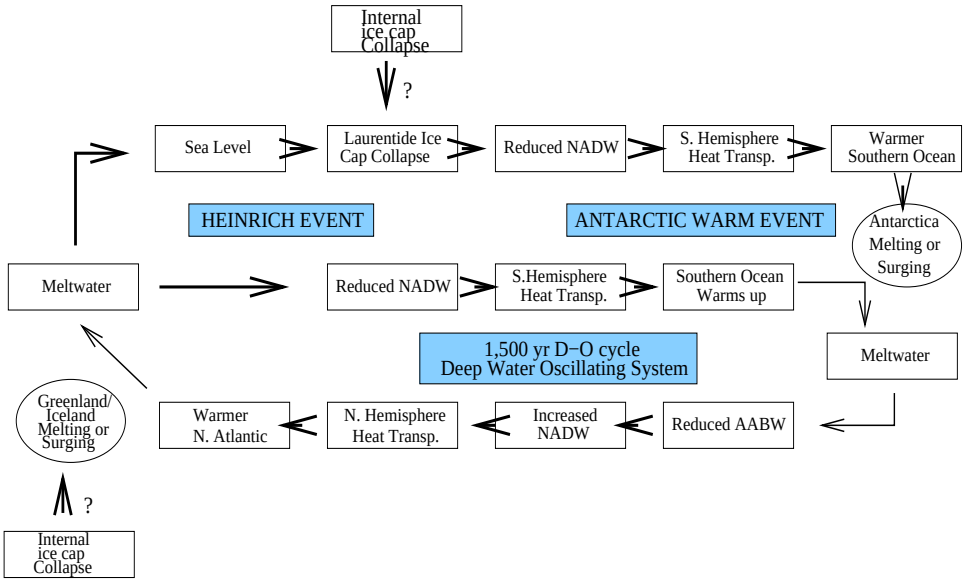

Fig. 1.2: *Schematic diagram showing the proposed theory to explain the origin of the abrupt climate jumps. After Maslin et al. (2001).*

1.3 Climate Reconstruction - An Overview

During the *LGM*, land characteristics were different from those observed at present, in the sense that e.g. parts of North America and northern Europe were covered by ice caps *(Peltier 1994)*. In addition, the global surface albedo differed from today's due to the presence of ice caps and different vegetation patterns *(Crowley, 1995)*. The atmospheric CO_2 concentration was about 150ppm less than today (*Neftel et al. 1982)*, but only minor changes in solar radiation occurred associated with the orbital parameters *(Berger, 1978)*. These modified boundary conditions are expected to lead to significant shifts in the mean climate as compared to present-day climate.

A pioneering reconstruction of the *LGM* boundary conditions was accomplished by *The Climate: Long-range Investigation, Mapping, and Prediction (CLIMAP 1981)* project. This reconstruction effort includes micropaleontology, carbonate percentages, ^{14}C ages dates, sea surface temperature estimates, and oxygen and carbon isotopic data. However, further investigations have shown inconsistencies of CLIMAP estimations of SST, the extent of land/sea ice and paleotopography with other paleodata sources *(e.g. Peltier 1994; Denton and Hughes 1981)*.

Estimates of the temperature distribution during the *LGM* can be based on different types of proxy data e.g. planktonic foraminifera in sediment cores (microfossil assemblages) *(CLIMAP 1981)*, stable isotope in ice cores *(Dansgaard et al. 1993)*, alkenone measurements in sediments cores *(Herbert et al 2001)*. Furthermore, pollen grains have been used to reconstructed paleo-vegetation patterns, the mean temperature of the coldest month and soil moisture (*Farrera et al. 1999; Prentice et al. 1992; Woodward 1987)*.

Microfossil assemblages can be used to reconstructed temperatures as recognised early in the history of oceanography. John Murray, naturalist of the CHALLENGER Expedition (1872-1875) discovered that planktonic foraminifera found in the sediments on the sea floor, and in particular their species compositions, store information on the temperature of the water which they lived in *(Murray 1887)*. The methods to derive surface temperatures from microfossil assemblages are well established. The SST is directly estimated from statistical differences of fossil assemblages from modern assemblages. Three methods have been used: the transfer function equations (TF) *(Barb et al. 1987)*, the modern analog technique, and the revised analog method (RAM) *(Waelbroeck et al. 1998)*. All of these methods are dependent on extensive reference data sets that must be calibrated with present-day SST (for example, COADS). Therefore, an improvement of the paleotemperature depends also on the quality of the reference data set.

The basis for temperature reconstructions in sediment cores is that oxygen incorporated into carbonates (such as in foraminifera microfossils), includes both major isotopes (^{18}O and ^{16}O), of which ^{16}O is the most abundant. The ratio of these two isotopes in water is temperature dependent and follows predictable geographic trends in the oceans, atmosphere, and glaciers. The ratio is altered whenever water undergoes a phase change. When sea water evaporates, for example, the heavier isotope ^{18}O is preferentially left behind in remaining sea water, while the resulting water vapour is depleted in ^{18}O . The oxygen-isotope composition of a water sample is expressed in $\delta^{18}O$ (Eq. 1.1) units per mil (1 permil = 0.1%) of relative concentrations with respect to the ratio of standard mean ocean water (*smow*).

$$\delta^{18}O = \frac{\frac{^{18}O}{^{16}O} - smow}{smow} \times 1000 \tag{1.1}$$

By definition, $\delta^{18}O$ is zero for standard mean ocean water. A value of $\delta^{18}O$ = -10 thus means the sample has an $^{18}O/^{16}O$ ratio 10 permil (or 1%) less than smow. The amount of water or ice required for analysis is small (5-10 g), and stable isotopes can be measured quite accurately using mass spectrographic techniques.

Under present conditions, the volume of land ice is relatively small, and this ice has $\delta^{18}O$ values around -30. During glacial periods, however, much isotopically light water was removed from oceans and stored in glaciers on land. This caused slight enrichment of ^{18}O in sea water to about $\delta^{18}O = +1.5$, while glacier ice had even lower $\delta^{18}O$ values of around -40. The oxygen-isotope values during past glaciations are preserved in glacier ice and in fossils buried on the sea floor. These isotopic records are primarily a measure of changing volume of glacier ice.

Oxygen-isotope ratios are also affected by temperature, for example, the water temperature in which e.g. formanifera grow or the air temperature in which snow crystallizes.

Based on the theory of postglacial relative sea level change and the static rebound, *Peltier (1994)* derived a paleotopography to the LGM (ICE-4G) that exhibits a similar extent but a much lower elevation, by as much as 1000 to 1500 meters than the previous *CLIMAP (1981)* reconstruction. Recently, a new global ice sheet reconstruc-

tion (ICE-5G) became available *(Peltier 2004)*. This data set differs significantly from the previous ICE-4G at all Northern Hemisphere locations that were glaciated during the LGM. These locations include all of northwestern Europe/Eurasia *(Peltier 2004)*, the British Isles *(Peltier et al. 2002)*, Greenland and the North American continent *(Tarasov et al. 2002; Peltier 2002)*. For instance, the Laurentide ice sheet is by about 1000 m higher whereas the Greenland ice sheet is about 500 m lower. Furthermore, the topographic feature associated with the Siberian ice sheet as captured in ICE-4G is absent in the ICE-5G data set.

In areas of permanent snow accumulation another kind of paleoreconstruction is commonly used, the equilibrium line altitude (ELA). The ELA marks the cross-section where total accumulation equals total ablation. The amount of ice entering into the section equals the amount of ice flowing out. Observations of modern glaciers indicate that the ELA approximates the height at which the accumulation area of the glaciers occupies 70% of its total area *(Bradley 1999)*. Mapping the differences between modern and paleo-ELA can provide useful insights into past climatic conditions. For example, in a pioneering study *Rind and Peteet (1985)* compared a GCM experiment driven by CLIMAP boundary conditions to pollen-inferred temperature data at low latitude and alpine ELA analyses. They showed that the model does not produce as much cooling at low latitudes as is implied by the terrestrial evidence. This has raised the question about the CLIMAP warming in the tropics.

Compared to today, the main conclusions of the *CLIMAP (1981)* reconstruction is that SSTs were similar or even higher in tropical regions than today. More recently, the reliability of the *CLIMAP (1981)* reconstruction has been questioned, based on findings that the tropics (high-latitudes) should have been colder (warmer) during the *LGM* than inferred from the CLIMAP reconstruction *(Sarnthein et al. 2003; Schäfer-Neth and Paul 2003; Stute et al. 1995; Guilderson et al. 1994; Broecker and Denton 1989)*. *Farrera et al. (1999)* suggested that tropical temperatures were on average 2.5 to 3°C lower than today at modern sea level. However, the magnitude of this cooling was not uniform. For instance, according to *Stute et al. (1995)*, Central America and northern South America were 5-6°C colder than today. This finding is, however, inconsistent with alkenone evidence that inferred *LGM* tropical SSTs to be only slightly colder than today *(Barb et al. 1997; Sikes and Keigwin 1994; Lyle et al. 1992)*.

In addition, modeling studies of the *LGM* have provided conflicting results concerning the tropical cooling. The eight AGCM used by PMIP *(Pinot et al. 1999; Joussane and Taylor 1995)* show a weak cooling over ocean and land and the simulated increase in continental aridity is less than shown by paleo-environmental data *(Pinot et al. 1999)*. Recent, Atmosphere-Ocean-Global Climate Model (AOGCM) simulations *(Shin et al. 2003; Kim et al. 2003; Kitoh et al. 2001; Bush and Philander 1999)* show also a disagreement in simulated tropical and the North Pacific temperatures. While *Kitoh et al. (2001)* simulate a warming of the subtropical Pacific, very similar to the CLIMAP SSTs anomalies, *Shin et al. (2003)* and *Bush and Philander (1999)* simulate a homogeneous North Pacific cooling. Using an AGCM coupled to a mixed layer *Broccoli (2000)*, obtained tropical SSTs that were 2°C lower than at the present, whereas *Kim et al. (2003)* simulate a tropical cooling of about 8°C. It is unclear which of uncertainties is largest: errors in the SST reconstructions, limitations

in the representativeness of the available terrestrial/oceanic data, or problems in the model projections themselves.

1.4 Concept and Structure of the Thesis

Despite intensive research on atmospheric circulation changes during the glacial period, the individual roles of the *LGM* boundary conditions in forcing the atmospheric and oceanic circulations have not been quantified systematically using coupled *atmosphere-ocean-sea-ice* models. Moreover, it is not clear whether these boundary conditions tend to produce similar responses in the climate system, or whether they are in some sense working against one another.

The most part of previous *LGM* modeling experiments have been performed with AGCM using either fixed SST or mixed layer slab ocean models *(Broccoli 2000; Webb et al. 1997; Manabe and Broccoli 1985)*. These models neglect oceanic upwelling, horizontal advection and dynamical ocean-atmosphere interactions that strongly affect the climate, in particular the equatorial/mid-latitudinal interplay. Furthermore, these *LGM* simulations neglected the potential role of land-surface albedo feedbacks on glacial climates. Except for the ice sheet albedo, land-surface conditions in both the PMIP simulations and in the recent AOGCM *LGM* simulations land-surface present conditions were used *(Shin et al. 2003; Kim et al. 2003; Kitoh et al. 2001; Bush and Philander 1999)*. *Levis et al. (1999)* using a dynamic vegetation model coupled to an atmosphere-mixed layer ocean model, showed that the impact of the land-albedo feedbacks on *LGM* climate, regionally and globally may play an important role.

1.4.1 Objectives and Questions to be addressed

The aim of this thesis is to investigate the atmospheric and oceanic circulations during the *LGM* as well as the responsible dynamical mechanisms leading to glacial climate anomalies. This study employs a coupled ocean-atmosphere-sea ice climate model (ECBilt-Clio) to study past climate changes.
The main questions addressed here are:

- What is the impact of the glacial boundary conditions on the atmospheric and oceanic circulations?
- Which mechanisms are responsible for glacial SST changes in the Pacific Ocean?
- How does the thermohaline circulation respond to glacial boundary conditions?

1.4.2 Structure of the Thesis

The model description and performance as well as the experimental design are presented in Chapter 2. Chapter 3 focuses on the atmospheric response to the individual *LGM* boundary conditions. The interaction between the transient eddies and the mean circulation is also highlighted. Part of this chapter has been submitted to the *Journal of Climate (Justino et al. 2004)*. Chapter 4 describes the changes of the wind-driven

and thermohaline circulations. The first part *(Timmermann et al. 2004)* describes the responsible mechanism for the simulated SST changes in particular the warming in the North Pacific and cooling in the equatorial Pacific. Moreover, the changes in sea ice, surface salinity, overturning circulation and the heat transport are explored. Finally, I summarise the main findings of this thesis in Chapter 5.

2. THE MODEL

Sometimes it is necessary to take a step backwards in order to go forwards.

Anonymous

2.1 Model Description - ECBilt-Clio

The simulations are performed with the intermediate global coupled atmosphere-ocean-sea-ice model ECBilt-Clio version 2. The atmospheric component is ECBilt *(Opsteegh et al. 1998)* a global spectral quasi-geostrophic (QG) model with three vertical levels (200, 500 and 800 hPa) and a horizontal resolution of approximately 5.6° (T21) *(Marshall and Molteni 1993)*. As an extension to the quasi-geostrophic equations, an estimate of the neglected terms in the vorticity and thermodynamic equations is incorporated. This ageostrophic forcing is computed from the diagnostically derived vertical motion and from the rotational component of the horizontal velocity (Eq. 2.2). The agestrophic terms are included in order to simulate the Hadley circulation properly. This has important consequences for the strength and position of the jet-stream and for the transient eddy activity *(Opsteegh et al. 1998)*.

2.1.1 Atmospheric Model: dynamics and physics

The **adiabatic** core of the atmospheric model is based on the vorticity equation, which reads,

$$\frac{\partial \zeta}{\partial t} + V_\psi \cdot \nabla(\zeta + f) + f_0 D + k_d \nabla^8 \zeta = -F_\zeta \tag{2.1}$$

where $\zeta = \nabla^2 \psi$ is the vertical component of the vorticity vector, ψ is the streamfunction, V_ψ is the rotational component of the horizontal velocity, D is the divergence of the horizontal wind, f is the Coriolis parameter, f_0 is f at 45° north and south, $k_d \nabla^8 \zeta$ is a highly scale selective diffusion and F_ζ contains the ageostrophic terms in the vorticity equation. F_ζ is expressed in terms of,

$$F_\zeta = V_\chi \cdot \nabla(\zeta + f) + \zeta D + \omega \frac{\partial \zeta}{\partial p} + \mathbf{k} \cdot \nabla\omega \times \frac{\partial V_\psi}{\partial p} \tag{2.2}$$

where, V_χ is the divergent component of the horizontal wind, $\omega = \frac{\partial p}{\partial t}$ is the vertical velocity in isobaric coordinates. Estimates of F_ζ are used to represent the effect of the ageostrophic circulation on the tendency of the geostrophic vorticity.

The **diabatic** core of the model is based on: the thermodynamic equation, which reads,

$$\frac{\partial}{\partial t}\frac{\partial \psi}{\partial p} + V_\psi \cdot \frac{\partial \psi}{\partial p} + \frac{\sigma}{f_0}\omega + k_d \nabla^8 \frac{\partial \psi}{\partial p} + k_R \frac{\partial \psi}{\partial p} = -\frac{RQ}{f_0 p c_P} - F_T \tag{2.3}$$

where $\sigma = -\frac{\alpha}{\theta}\frac{\partial \theta}{\partial p}$ is the static stability, α is specific volume, θ is the potential temperature, k_R is a Rayleigh damping coefficient, R is the gas constant, p is pressure, c_P is the specific heat for a constant pressure, Q is the diabatic heating and F_T is the advection of temperature by the ageostrophic winds.

$$F_T = V_\chi \cdot \nabla \frac{\partial \psi}{\partial p} \tag{2.4}$$

Equations (2.1), (2.3) and the continuity equation can be combined into one equation for the quasi-geostrophic potential vorticity q by eliminating ω and D. It leads to,

$$\frac{\partial q}{\partial t} + V_\psi \cdot \nabla q + k_d \nabla^8 \frac{\partial}{\partial p}\left(\frac{f_0^2}{\sigma}\frac{\partial \psi}{\partial p}\right) = -\frac{f_0 R}{c_p}\frac{\partial}{\partial p}\left(\frac{Q}{\sigma p}\right) - F_\zeta - \frac{\partial}{\partial p}\left(\frac{f_0 F_T}{\sigma}\right) \tag{2.5}$$

where q is defined as:

$$q = \zeta + f + f_0^2 \frac{\partial}{\partial p}\left(\sigma^{-1}\frac{\partial \psi}{\partial p}\right) \tag{2.6}$$

ECBilt uses simplified parametrisations for the diabatic heating due to radiative fluxes (Eqs. 2.7, 2.8). The diabatic heating is computed at 650 and 350 hPa from the various diabatic process as follows:

$$Q_{350} = \frac{g}{c_p \Delta p_u}(LW_2 - LW_1 + SW_u + LH_u) \tag{2.7}$$

$$Q_{650} = \frac{g}{c_p \Delta p_l}(\sigma T^4 - LW_s - LW_2 + SW_l + LH_l + SH) \tag{2.8}$$

See Figure 2.1 for the symbols of the different terms in the longwave radiation (LW). LH_u and LH_l refer to the release of latent heating in the upper and lower layer respectively. Here the latent heat release is due to dynamic and convective rain. The sensible heat SH is released in the lower layer. Δp_u and Δp_l are the layer depths of the upper (350 hPa) and lower (500 hPa) layer respectively.

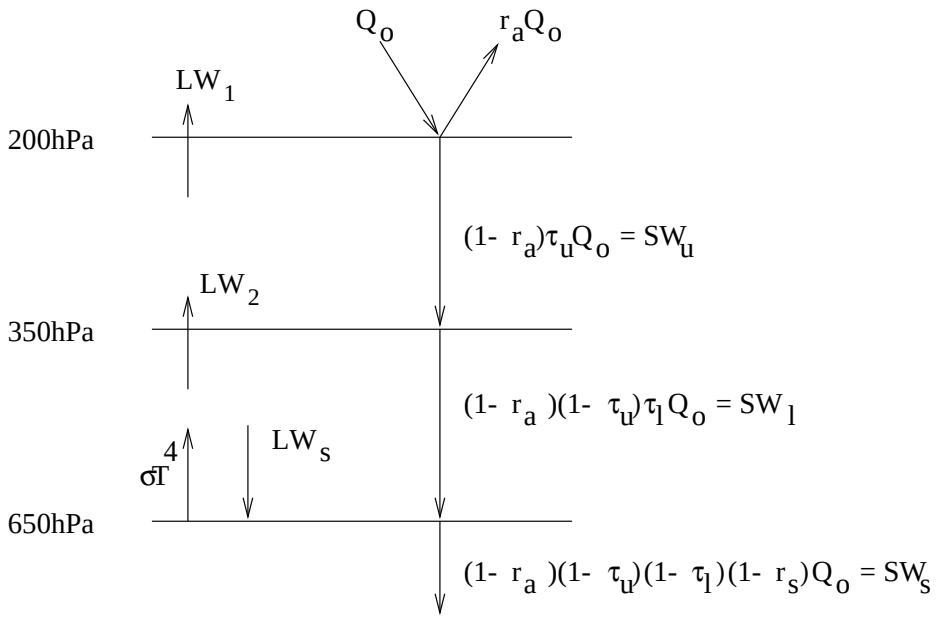

Fig. 2.1: *Radiation scheme of the atmospheric model (ECBilt). The subscripts l and u denote the upper and lower layer, and s the surface layer, respectively. SW_u and SW_l are the shortwave radiation. Q_0 is the incoming solar radiation, r_a is the planetary albedo, τ_u and τ_l are the absorption coefficients. r_a, τ_u and τ_l are given as a function of latitude and time of the year. The surface albedo r_s is determined by the surface characteristics.*

2.1.2 Model Discretisation

In deriving the discretised form of the quasi-geostrophic potential vorticity (Eq. 2.5), ECBilt starts from equation 2.1 and equation 2.3. The vorticity equation 2.1 is applied at the three vertical levels, 200 hPa, 500 hPa and 800 hPa whereas the temperature equation 2.3 is applied at the intermediate levels 650 hPa and 350 hPa. At the top of the atmosphere (p=0 hPa) the rigid lid $\omega = 0$ is applied. The lower boundary condition for ω is:

$$\omega_s = -\rho_s g \left(\frac{C_D}{f_o} \zeta_s - V_{\zeta s} \cdot \nabla h \right) \tag{2.9}$$

where ζ_s and $V_{\zeta s}$ are the vorticity and the rotational velocity at the top of the boundary layer respectively, for which the values at 800 hPa are chosen, C_D is the surface drag coefficient, ρ_s is the density at the surface and h is the orography height. The QG equation is solved using a fourth-order Runda-Kutta scheme. The physics is integrated using a forward scheme and is computed on grid-points at the gaussian grid.

2.1.3 The Coupled Model

The sea-ice ocean component is the Clio model (Coupled Large-scale Ice Ocean Model). It is based on the primitive equations and employs a free-surface ocean general circulation model. The horizontal resolution is 3° x 3°, and there are 20 unevenly spaced vertical levels in the ocean. The ocean component includes a relatively sophisticated parametrisation of vertical mixing and bottom boundary layer processes. Clio contains a 3-layer dynamic-thermodynamic sea-ice model that simulates the changes of snow and ice thickness in response to surface and bottom heat fluxes. The coupled model has realistic topography and bathymetry. Furthermore, the ocean model CLIO includes mixing along isopycnals and it captures the effect of meso-scale eddies on the transport *(Gent and McWilliams 1990)* as well as the dense water flow down topographic features *(Campin and Goosse 1999)*. The individual models are coupled by exchanging momentum, freshwater and heat. The ECBilt-Clio model contains a full hydrological cycle including a land bucket model for soil moisture. The time step of the atmospheric model is 4 hours, whereas the ocean model has a time step of 1 day, implying 6 atmosphere time steps for one ocean time step. During these 6 time steps the ocean surface is kept constant. The atmospheric model is two orders of magnitude faster than state-of-the-art AGCM.

The main advantage of ECBilt-Clio compared to coupled AGCMs is its computational efficiency (a 1000 years model run takes approximately 7 days CPU time on a Compaq Alpha workstation XP1000), while it still provides a realistic representation of the large scale dynamics. Hence, it is possible to perform millennial-scale simulations to study the behaviour of the coupled atmosphere-sea-ice-ocean system on a multi-centennial time-scale, as well as to explore the climate sensitivity associated with changes in boundary conditions and the physical processes.

Some limitations of ECBilt-Clio originate from the set-up of the atmospheric model, which is based on the quasi-geostrophic approximation, from the employment of a weak freshwater flux correction, and from using just three atmospheric layers. Another disadvantages of ECBilt-Clio is that due to the low resolution of the atmospheric component and quasi-geostrophic approximation tropical dynamics is not captured properly.

2.2 Model Performance

In order to analyse the difference between the climate during the *LGM* and a pre-industrial reference state, a series of sensitivity experiments is performed. As a reference experiment, the model is run for 10000 years (CTR) using early industrial atmospheric CO_2 concentrations (288 ppm) and present-day albedo and topography boundary conditions. After about 1000 years of integration the model reaches a quasi-equilibrium state, in global surface temperature (Fig. 2.2). The evaluation of the ECBilt-Clio climatology is done by comparing it to NCEP/NCAR Reanalysis data *(NCEP, 2002)*. Given the simplicity of the atmospheric model, good agreement is found for annual mean temperature pattern at 2m (t2m) (Fig. 2.3a,b); and in particular for the zonal mean (Fig. 2.3c). In addition, the annual cycle of northern hemisphere

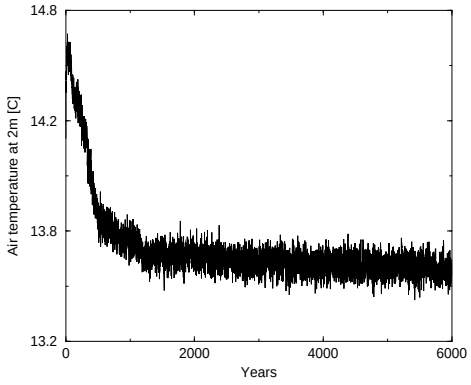

Fig. 2.2: *Global mean annual air temperature at 2m in the ECBilt-Clio control simulation [°C].*

Air temperature [°C] NH summer	NH winter	Error	Model
15.0	12.9	-	Observations
14.9	12.8	0.10	ECBilt-Clio
15.7	12.3	0.65	Uvic
15.5	12.6	0.40	COLA
15.6	13.0	0.35	GISS
19.6	15.5	3.60	NCAR

Tab. 2.1: *Coupled model simulations of air temperature at 2m and the absolute error from NCEP Reanalysis. Adapted from Weaver et al. (2001).*

temperature is captured realistically, as compared to other models (Table 2.1). The global mean annual model t2m (13.6°C) differs from the NCEP data (13.9°C) by 0.3°C. There are, however, regions in the model where the differences are larger (see Fig. 2.3). For example, simulated eastern Antarctica temperature is lower than in the Reanalysis while temperature in western Antarctica is higher. Over most parts of the highest mountains (e.g. Tibetan Plateau, Greenland, Rocky Mountains) and over the Arctic the simulated temperature is lower than in the NCEP Reanalysis data. This effect is more pronounced in partially snow- or ice covered regions. Another discrepancy is the simulated meridional thermal gradient at the east coasts of North America and Asia. The thermal gradients simulated by ECBilt-Clio are much weaker. In addition, over the eastern equatorial Pacific the model does not reproduce properly the oceanic cold tongue (see Figs. 2.3a,b). In the zonal mean, however, the ECBilt-Clio compares well with the observed patterns. The largest difference between the model and the observations is located to the north of 65°N (Fig. 2.3c). Anomalous low temperatures are in large part a result of the overestimation of ice thickness that insulates the atmosphere and cuts off the direct sensible heat flux from the warmer ocean below. The seasonal model variability is analysed by computing the amplitude of the first harmonic of air

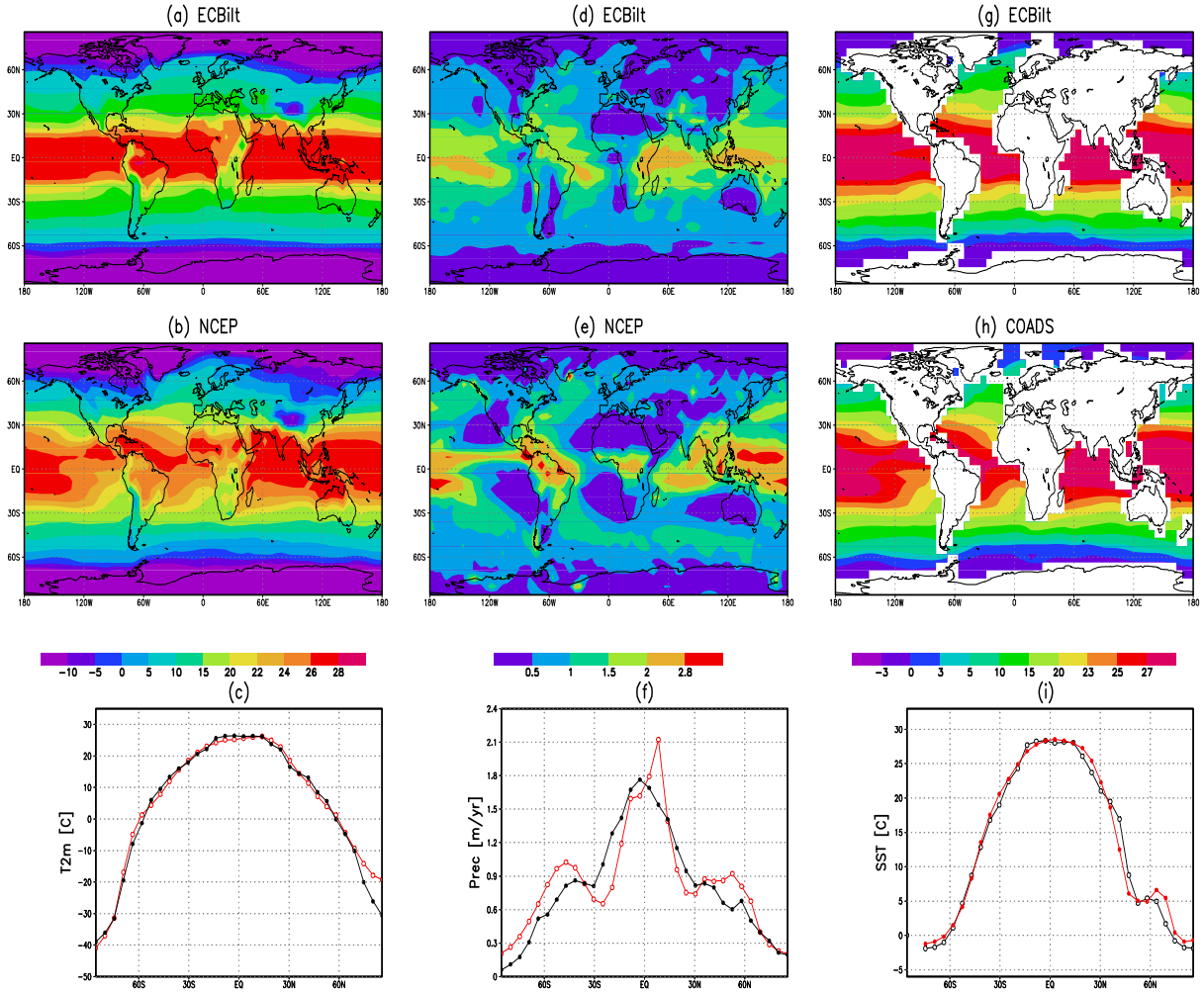

Fig. 2.3: *Annually-averaged air temperature at 2m [°C]. a) simulated by the ECBilt-Clio, b) NCEP Reanalysis and c) black line: zonal average of the ECBilt-Clio, red line zonal average of NCEP Reanalysis. d), e) and f) the same as a,b,c but for precipitation and g,h,i for SST.*

temperature at 2m (Fig. 2.4). Compared to NCEP Reanalysis data, ECBilt-Clio is able to reproduce both, the pattern and the amplitude of annual variability. As a result of the Northern Hemisphere winter bias, the model annual cycle is more pronounced over eastern Asia. Over North America, Europe and in the tropics, the model and NCEP show a surprisingly good agreement.

The simulated precipitation (PPT) patterns exhibits the most significant characteristics evident in the NCEP data. The observed and simulated values over the equatorial regions associated with the Inter-tropical Convergence Zone (ITCZ) exceed 1.5 myr^{-1} (Fig. 2.3d,e). The most notable discrepancies can be seen over the western subtropical Pacific where the PPT associated with convection in the warm pool is underestimated, over the rain forest in Brazil and in central Africa where PPT is about 35% lower than in the observations. Dryer conditions are also simulated in both hemispheres around

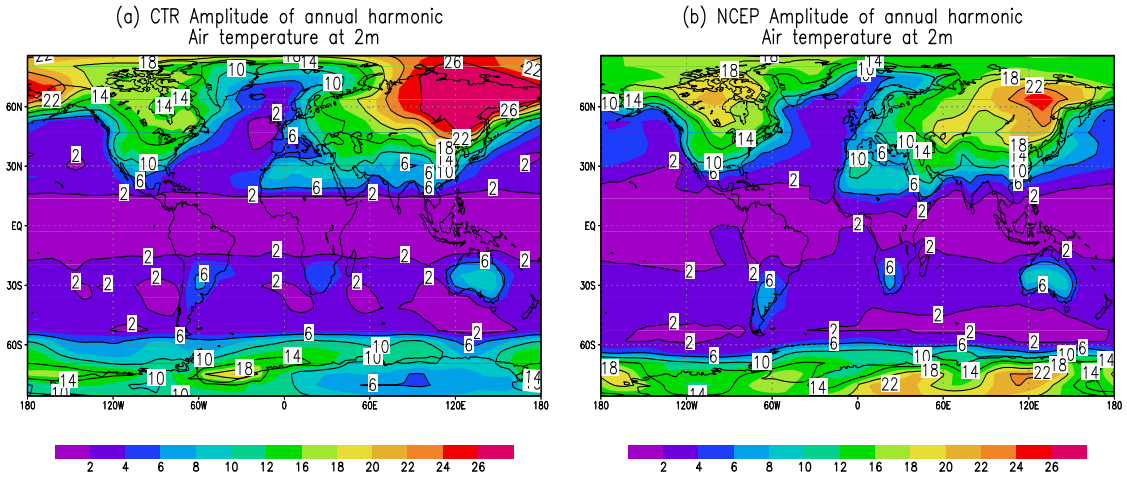

Fig. 2.4: *Amplitude of the first harmonic of air temperature at 2m (°C). (a) ECBilt-Clio (b) NCEP.*

45°N and 45°S as a result of weaker modeled storm tracks (Fig. 2.3f). When averaged globally the simulated PPT (0.86 myr^{-1}) is similar to the NCEP Reanalysis (0.87 myr^{-1}), as well as the results from other models as seen in Table 2.2.

The simulated sea surface temperature (SST) and the COADS observations *(da Silva et al. 1994)* are in good agreement (Fig. 2.3 g,h,i), given the simplicity of the atmospheric model. Nevertheless, as a result of the cooling in high latitudes, the simulated global mean SST (17.7°C) is approximately 0.5°C lower as compared to the global mean SST observed from COADS. The model simulates slightly warmer conditions in

PPT m/yr	Error	Model
0.87	-	Observations
0.86	0.01	ECBilt-Clio
1.06	0.03	MRI M1
0.99	0.04	Uvic
0.96	0.07	COLA
1.14	0.11	GISS
1.37	0.34	NCAR

Tab. 2.2: *Coupled model simulations of globally-averaged PPT and the absolute error from NCEP Reanalysis. Adapted from Weaver et al. 2001, Kitoh et al. 2001*

.

the North Atlantic, Nordic Seas and the Oyashio area. This warming is likely a result of weaker cold air advection from east Siberia and Canada during the boreal winter. In addition, the simulated Kuroshio and Gulf Stream, separate from the American coast near New Foundland, rather than at Cape Hatteras. This typical low-resolution model

feature is associated with an enhanced heat transport into the extra-tropics. In the subtropics, the model shows warmer conditions in the east Pacific and Atlantic as a consequence of the underestimation of the surface zonal wind, which in turn, reduces the upwelling and the evaporative cooling. The model and observations also disagree in areas of marine stratus-cumulus formation i.e. over the west coast of Africa and South America. These areas typically exhibits strong upwelling, that is underestimated in the model. In the zonal mean (Fig. 2.3i), the model and COADS SST patterns exhibit almost the same shape and magnitude. This suggests that despite the local SST differences between ECBilt-Clio and the observations zonally averaged the atmospheric dynamics linked to the meridional thermal gradient might be not affected. One should not expect an EMIC system, like ECBilt-Clio, to properly simulate the oceanic features associated with small-scale coupled processes like upwelling, in particular along the western coast of the continents. In general, the problems and caveats mentioned above also have been found in other atmosphere-ocean-sea-ice models, as discussed in *(IPCC, 2001)*.

The zonally averaged vertical distribution of the zonal wind and its observational counterpart from NCEP Reanalysis are displayed in Figure 2.5a,b, respectively. In general, model and observations exhibit a large degree of similarity. Nevertheless, compared to the NCEP data, the simulated jet stream maximum is weaker and shifted poleward by approximately 10°N. This weaker jet is in part a consequence of simulated weaker transient and stationary eddies, as will be discussed in Chapter 4. The weakening of the zonal wind is also observed in the Southern Hemisphere (SH) around 45°S. The simulated global wind at 500hPa and the NCEP observations are depicted in Figure 2.6. During December, January, February (DJF) the simulated wind is quite similar to the observations in terms of magnitude and directions. However, as a result of an overestimation of Aleutian low, the model simulation disagrees with the observations over northeast Asia, showing a northwesterly wind component while the NCEP data display a southerly flow. In the SH the anticyclonic winds associated to the high pressure systems are well placed by the model and have almost the same magnitude as in the NCEP Reanalysis. In ECBilt-Clio the trade winds have an artificially strong zonal component, as a result of dynamical simplification adopted in the model. In the extra-tropics, the model can well reproduce the shape and position of the westerlies, although, their strength is slightly weaker. During June, July, August (JJA) (Fig. 2.6b,d) the similarities between ECBilt-Clio and NCEP become evident in particular in mid-latitudes between 60°W and 60°E.

Figure 2.7a shows the simulated stationary waves at 500 hPa during the Northern Hemisphere (NH) winter. Some of the distinct observed feature of stationary waves, i.e. the Aleutian low, the low over Hudson Bay and the high over the west coast of North America and Europe are well reproduced by ECBilt-Clio. Large differences between model and observations can be seen in particular over North America and Greenland. Furthermore, the simulated Aleutian low is shifted northward as compared to the observations (Fig. 2.7a,c). A weakening of the stationary wave amplitude in the NH can lead to a substantial weakening of the poleward heat transport, as discussed by *Jackson (1999)*. Low surface temperature bias simulated at high latitudes can be partially attributed to the underestimation of the heat transport by the modeled

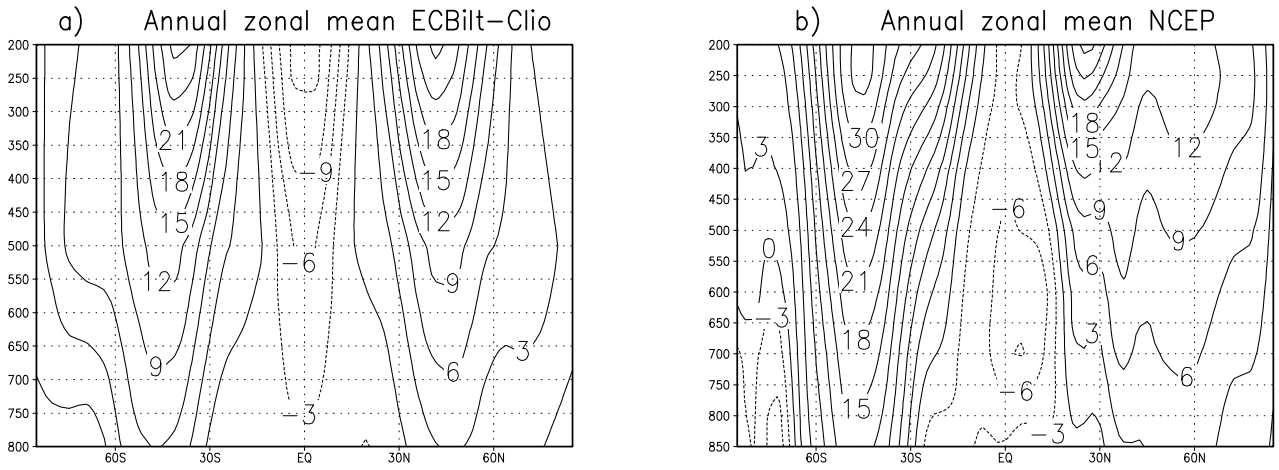

Fig. 2.5: *Simulated zonally averaged zonal wind [m/s] (a) ECBilt-Clio and (b) NCEP.*

Sea-ice cover	Season	Observed	Simulated
Nor. Hem.	JJA	11.5	10.4
	DJF	14.5	14.3
Sou. Hem.	JJA	16.0	21.3
	DJF	7.0	9.7

Tab. 2.3: *Simulated and observed sea-ice area* $[10^6 \times km^2]$.

stationary waves. With the exception of the Atlantic ridge that is much weaker, the simulated ridges bear good agreement with the NCEP Reanalysis having almost the same amplitude. The simulated stationary waves in the SH are weaker than in the NCEP observation and shifted southward.

During the NH summer the NCEP data (Fig. 2.7d) show a trough over southeastern Asia extending onto the central north Pacific. In the simulation there is almost no stationary wave activity in the region (Fig. 2.7b). Over North America, the observed pattern is reproduced somehow better, showing a ridge (trough) at the western (eastern) coast. In the SH the model can reproduce the wave train around Antarctica with a trough over the eastern hemisphere and a ridge over the Pacific Ocean. *Opsteegh et al. (1998)* attributed the weaker stationary waves in ECBilt-Clio to the underestimated mean potential vorticity (PV) forcing. They have found very good climate representation by forcing the model with observed PV. It is important to note that the model can reproduce reasonably well the annual mean and seasonal variations of the observed pattern. In the analyses of the glacial climate one should keep in mind the shortcomings of the model simulation in terms of the representation of the stationary waves.

As a result of the simulated wind bias associated with the anomalous Aleutian low, the ice transport and sea-ice thickness are overestimated over the central Arctic.

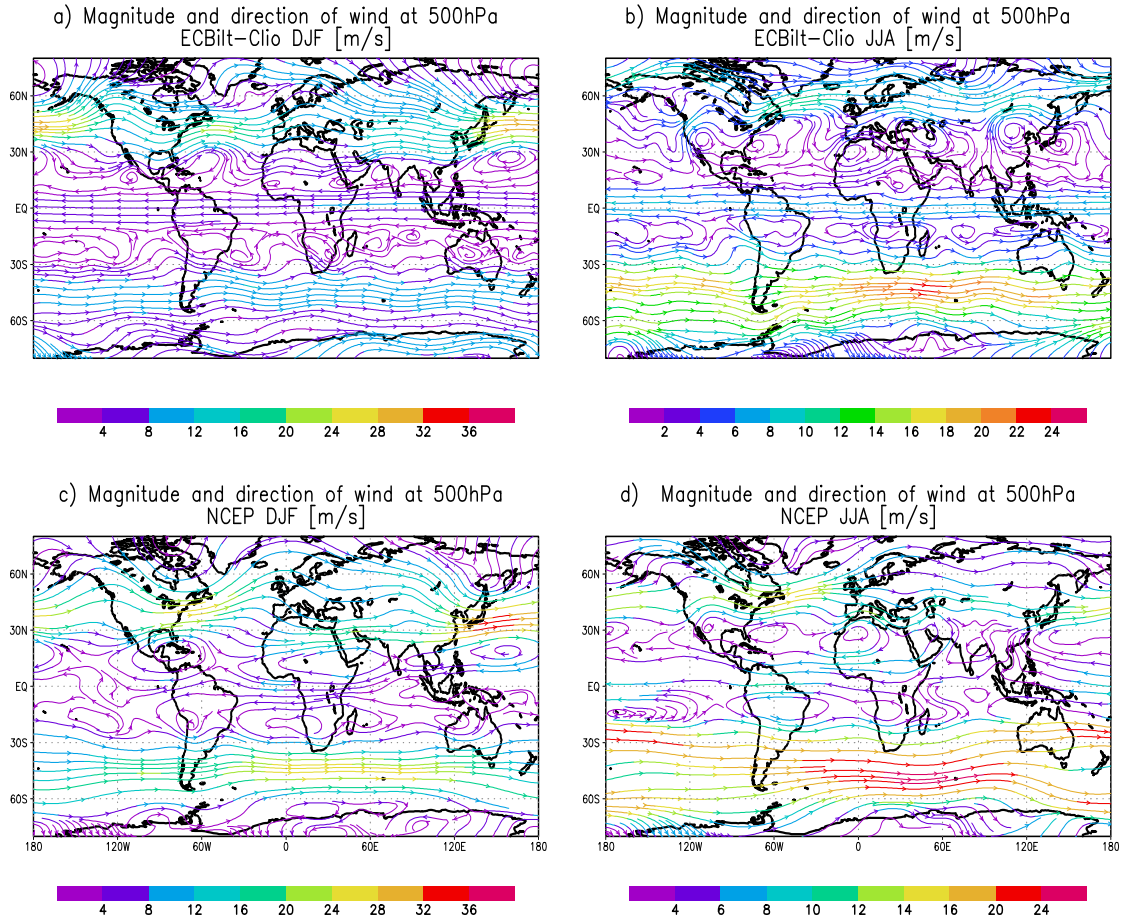

Fig. 2.6: *Global distribution of wind [m/s] at 500hPa in DJF for (a) ECBilt-Clio (c) NCEP data, (b) and (d) the same as (a), (b) but for JJA.*

The modeled sea-ice maxima are located in the Kara and the Barents Seas. This is opposite to the inference of ice thickness derived from climatological surface air temperature *(McFarlane et al. 1992)* that shows the sea-ice thickness maximum to north of Greenland. It should be noted however that in the McFarlane's climatology, ice advection is not considered and the sea-ice thickness could hence be underestimated in some areas. On the other hand, the Antarctic ice distribution shows a reasonable agreement with the observations. The largest difference in the Weddell Sea occurs as a consequence of the lower SST and the unrealistic easterly winds pushing sea-ice to the Antarctic Peninsula. The estimated sea-ice area is very close to the observations (Table 2.3), except during the SH winter. It should be noted also that very few measurements of the sea-ice distribution are available and a reliable climatology does not exist.

Although the atmospheric model is based on the quasi-geostrophic assumption and employs just three vertical levels and a T21 resolution. The analyses above clearly revealed the capability of ECBilt-Clio to reproduce basic climatic features satisfactorily at relatively low computational coast. Therefore, ECBilt-Clio can be used to examine

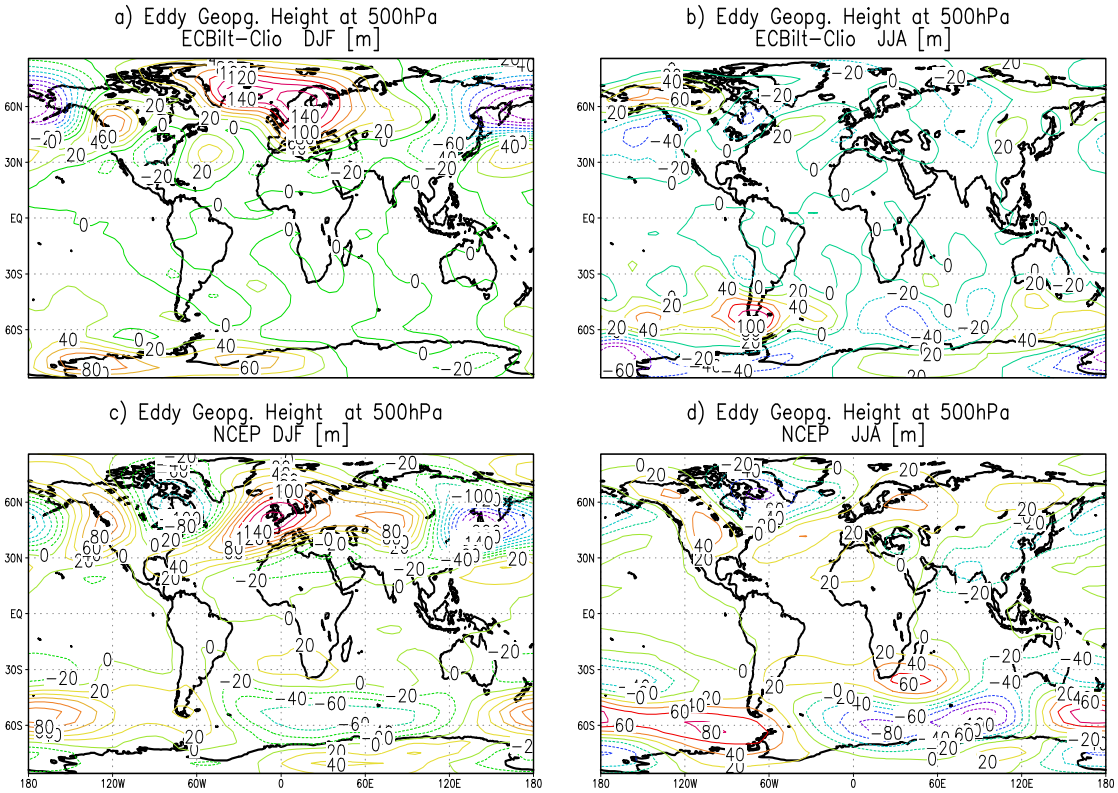

Fig. 2.7: *Eddy geopotential height at 500hPa [m] CTR in DJF (a) and JJA (b) and NCEP in DJF (c) and JJA (d)*

the sensitivity of a particular process or subcomponent of the climate system across a wide range of parameters.

2.3 Experimental Design

In order to analyse the climate during the *LGM* 17 experiments are performed (Table 2.4). In total this corresponds to 21600 model years. The first six simulations are the main core of the experimental design. They are used to quantify the climate response to the *LGM* boundary conditions. The other experiments were conducted to examine the climate sensitivity to a particular process (e.g. atmospheric response to tropical SST (ENSO-EXP), stationary waves in a flat Earth (TOPO-0), Heinrich events ($0.47FI$)).

LGM boundary conditions

In order to simulated the *LGM* climate the Paleoclimate Modelling Intercomparison Project *(PMIP, Joussaume and Taylor, 1995)* recommended to modify four major boundary conditions i.e. orbital parameters (hereafter ORB), reduced atmospheric

Main Simulations		
Simulations	Boundary condition	Model Years
CTR	Pre-industrial	10000
LGM	LGM	6000
TOPO	LGM Topography	1000
ALB	LGM Albedo	1000
CO2	LGM CO_2	1000
ORB	LGM Orbital forcing	1000
TOTAL		20000
Secondary Simulations		
Simulations	Climate feedback	Model Years
FF	Forest fraction	50
ALB-aging	Old ice albedo	50
ENSO-EXP	Atmospheric response	300
TOPO-NH	Topography	50
TOPO-SH	Topography	50
TOPO-0.5	Topography	50
TOPO-1.5	Topography	50
TOPO-2	Topography	50
TOPO-0	Stationary waves	50
0.19FI	Heinrich event	300
0.38FI	Heinrich event	300
0.47FI	Heinrich event	300
TOTAL		1600

Tab. 2.4: *Summary of the coupled simulations.*

CO_2 (hereafter CO2), ice sheet albedo (hereafter ALB), ice sheet topography (hereafter TOPO). The combined effect will be abbreviated as LGM = ALB + CO2 + TOPO + ORB (hereafter LGM). Based on previous experience from coupled *LGM* simulations, the role of sea-level changes is disregarded here. Furthermore, due to the large uncertainties in the ice sheet mass balance during the glacial period *(Marshall and Clark 1999)* ablation process and changes of the ice sheet runoff are also disregarded.

Changes of the orbital parameters (eccentricity, obliquity and precession) have a significant effect on the amount of solar radiation that reaches the top of the atmosphere. The eccentricity of the Earth's orbit varies between near-circularity and slight ellipticity at periods of about 100 kyr and 400 kyr. Changes in eccentricity cause only very minor variations, approximately 0.03% in the total annual insolation. The obliquity (the tilt of the Earth's rotational axis), varies between 22° and 25° at a period of 41 kyr. The changes in obliquity tend to amplify the seasonal cycle in the high latitudes of both hemispheres. For instance, the climate around 6 kyr BP was strongly affected by obliquity changes. It was influenced by enhanced summer insolation over the NH due to an increase of obliquity (24.1° rather than 23.4° today). The third orbital effect in the orbital forcing is the precession of the equinoxes. It affects the date of

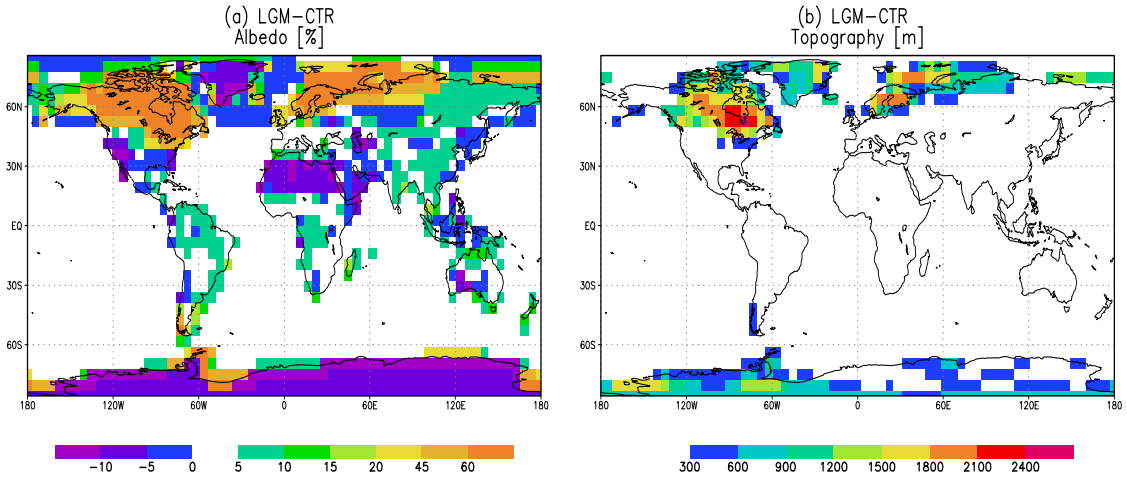

Fig. 2.8: *Albedo anomalies LGM - CTR [%] (a) and topography anomalies LGM - CTR [m] (b).*

	LGM	Present Day
Long. of Perih.	114.42	102.04
Obliquity	22.95	23.44
Eccentricity	0.019	0.016
Date of Perihelion	Jan. 15	Jan. 3

Tab. 2.5: *LGM and Present-day orbital parameters (Berger, 1978).*

perihelion and occurs with a main period of about 21 kyr causing warmer winters and cooler summers in one hemisphere while doing the opposite in the other hemisphere. The strength of this effect is largest at the equator and decreasing towards the poles. A climate effect is only present for large eccentricity values. Hence, precessional cycle is amplitude modulated by eccentricity cycle, yielding distinct periods of 19 kyr and 23 kyr. Except for a slight reduction in summer insolation caused by reduced obliquity during the *LGM*, the changes in solar forcing due to *LGM* changes in the orbital parameters are very weak. The respective present day and *LGM* values of the orbital parameters are shown in Table 2.5.

In addition to the orbital changes, paleo proxy-data indicate that during the *LGM* the atmospheric CO_2 concentration was reduced by about 150ppm compared with its actual concentration (*Neftel et al. 1982)*. The other two prominent changes refer to the land albedo and the ice-sheet topography. In this study, the land albedo is derived from a reconstructed *LGM* vegetation mask *(Crowley 1995)* where the deforested soils and plant cover are replaced by their respective albedo (Fig. 2.8a). Despite the uncertainties in the *LGM* land cover, *Adam and Faure (1997)* suggest that the rainforest may have been one third or less of its area today. The difference is also observed over Eurasia where the actual forest has changed to desert, semi-desert and tundra. In addition, as a result of the changes from present-day sand desert and barren land to

desert during the *LGM*, northern African and southern Australian albedo have been reduced.

The ice-sheet topography (ICE-4G) is inferred from more than 400 time series of relative sea level history based upon the ^{14}C dating of raised and submerged marine shorelines *(Peltier, 1994)*. These time series contain information on both the internal rheology of the Earth and the space- and time-dependent thickness of the ice. This data base contains 203 time series inferred from ice-covered locations. Figure 2.8 shows the differences (LGM - CTR) in topography and land albedo used in the sensitivity experiments. It is important to note that both topography and albedo files were interpolated to T21 resolution using bi-linear interpolation *(GrADS 1990)*. The ice sheet topography in TOPO and LGM experiment is included as an anomaly between the ICE-4G reconstruction and present-day topography. This anomaly field is added to the default topography pattern of the atmospheric model ECBilt.

When averaged globally the land albedo in LGM is 7% higher than in the CTR. However, the inclusion of ice sheet parameters over North America and Europe increases the albedo by more than 60% in those areas. Moreover, the ice caps create a topographic barriers to atmospheric flow of about 2000m. Changes in the land surface characteristics (albedo, topography) have a large impact on the atmospheric circulation during the *LGM*, as will be discussed in following sections.

3. ATMOSPHERIC CHANGES DURING THE LAST GLACIAL MAXIMUM

Formerly the earth produced all sorts of fruits, plants and roots. But now almost nothing grows...

Olafur Einarsson, (1573-1659)

3.1 Introduction

The climate of the Last Glacial Maximum (about 21,000 years ago) is an interesting test case to study the importance of climate feedbacks. During the *LGM* land surface characteristics were different from those observed today. As an example, parts of North America and Northern Europe were covered by ice caps, the atmospheric CO_2 concentration was about 150ppm lower than today and the global surface albedo was different from today's due to the presence of ice caps and a different vegetation pattern. Global climate simulations driven by *LGM* boundary conditions are a helpful tool to understand why glacial climates were so different from today's climate.

The *LGM* climate has been the subject of several modeling studies focusing on the glacial-interglacial variations *(e.g. Peltier and Hyde 1984; Suarez and Held 1979)* and the response of the atmospheric circulation to *LGM* boundary conditions *(Kitoh et al. 2001; Dong and Valdes 1998; Cook and Held 1988; Rind 1987; Manabe and Broccoli 1985)*. Recently, coupled atmosphere-ocean general circulation models (AOGCM) *(Shin et al. 2003; Hewitt et al. 2001; Bush and Philander 1999)* and intermediate coupled models *(Ganopolski and Rahmstorf 2001; Weaver et al. 1998)* have been used to improve our understanding of mechanisms of past climate change.

A thorough paleo-proxy-data-climate-model comparison can be a first step towards an assessment of model performances in significantly different climates. Ultimately this type of research will help to assess also the potential of climate models, to forecast future climate changes. Despite extensive research on atmospheric circulation changes triggered by glacial boundary conditions, their *relative* roles in forcing the atmospheric changes, to my knowledge, have not been quantified systematically using coupled atmosphere-ocean-sea-ice models.

Two pioneering studies by *Cook and Held (1988)* and *Rind (1987)* revealed that the glacial wintertime circulation in the northern hemisphere is most strongly influenced by topographic forcing. The Laurentide ice sheet imposes an upstream blocking situation whereas the downstream low interacts with the upstream high generated by the European ice sheet.

In this chapter, the impact of glacial boundary conditions on the simulated LGM

mean climate is explored. Moreover, I focus on stationary and transient eddies activities. Transient eddies provide an important contribution to the atmospheric heat, momentum and moisture transport. Hence, they are a key element in driving large-scale climate changes and the stability of ice caps *(Bromwich et al. 1993)*, which in turn feedback to the atmospheric circulation through diabatic and orographic forcing.

3.2 Changes in Radiative Forcing

LGM boundary conditions have a direct impact on the radiation budget of the climate system. Changes in land albedo, for instance, affect the net incoming solar radiation due to high albedo of snow and ice. In addition, as shown above, *LGM* albedo is increased over Laurentide and Scandinavian ice sheets. Moreover, the reduction of atmospheric CO_2 concentration exerts an important influence on the long wave radiation. In order to determine the magnitude of the radiative forcing anomalies associated with changes in boundary conditions a method described in *IPCC (2001)* is used. The difference between annual mean outgoing and incoming radiation for sensitivity experiments and pre-industrial control simulation (Eq. 3.1) is computed.

$$\Delta R = \Delta S + \Delta F \tag{3.1}$$

Where, the annual mean radiative forcing is R, the annual mean net incoming solar radiation is denoted by S $(down - up)$ and the annual mean net outgoing longwave radiation $(down - up)$ is given by F. Δ denotes the anomalies between the sensitivity experiments and the pre-industrial CTR run. In fact, the radiative forcing due to the introduction of an agent (e.g., LGM boundary conditions) is calculated at the tropopause AFTER allowing for stratospheric temperatures to readjust to radiative equilibrium, but with surface and tropospheric temperatures and state held fixed at the unperturbed values. The analyses are based on the last 300 years of 1000-year-long each simulation. Table 3.3 shows the radiative forcing anomalies for each experiment. When globally averaged, all runs except for ORB, generate a negative radiative forcing that tends to cool the climate system. The changes in R are largest when changes of land albedo (ALB) are considered. This effect is mostly due to the higher ice sheet albedo and thus to a decrease in the absorption of solar radiation in the NH. The NH cooling tendency is twice as strong as in the SH. This is reasonable since the albedo changes are mainly placed in the NH. These results agree with previous estimates (*Hewitt and Mitchell 1997)* as well as with results obtained by *Hansen et. al., (1993)* and *Hoffert and Covey (1992)* which were based on the CLIMAP ice sheet reconstruction. *Hansen et. al., (1993)* estimate the radiative forcing due to the ice sheets and vegetation to be -3.5 $\pm$ 1Wm^{-2}, while *Hoffert and Covey (1992)* estimate the forcing to be -3.0 $\pm$ 0.5Wm^{-2}.

The TOPO experiment reveals that both NH and SH topography changes contribute to local hemispheric cooling. It should be noted that the changes in TOPO account only for the topographic characteristics of the ice sheet (elevation) and not the albedo. Therefore, radiative forcing due to changes of the topography are weak as compared to those triggered by glacial albedo anomalies. The radiative changes produced by

the reduced CO_2 show that the NH is more sensitive to CO_2 changes than the SH, in agreement with other *LGM* studies *(e.g. Broccoli and Manabe 1987)*. However, the ECBilt-Clio response to reduced CO_2 is smaller by a factor of 2 compared to the results of *Hewitt and Mitchell (1997)* and *Broccoli and Manabe (1987)*. Glacial changes of orbital parameters are associated with the weakest radiative forcing anomalies. ORB is the only simulation which generates a very weak positive radiative forcing anomaly due to the enhanced insolation in the tropics. The total radiative forcing anomaly as obtained from the combination of all *LGM* boundary conditions amounts to -4.3 W/m^2, associated with a global surface cooling of -2°C. The inclusion of all *LGM* boundary conditions produces radiative changes of comparable magnitude in the NH and SH. At a first glance, one would expect much larger changes in the NH due to the ice sheet topography and albedo changes. Although an explanation for this common cooling tendency is not trivial, it be can argued that the increased sea-ice around Antarctica (higher albedo), reduces the amount of absorbed shortwave radiation and plays an important role in strengthening the radiative forcing anomaly in the SH.

Temperature anomalies simulated by TOPO, ORB and CO2 do not linearly reflect the changes in the magnitude of radiative forcing directly. Although TOPO simulates a larger radiative forcing than the CO2, the global cooling in TOPO is not as strong as in CO2. On the other hand, the weak forcing in ORB produces almost the same temperature response as in TOPO. It turns out that changes in atmospheric and oceanic circulations associated with the boundary conditions can enhance or damp the climate response to the radiative forcing.

Sensitivity Exp.	ΔR $[W/m^2]$ and t2m [°C]		
	Global	NH	SH
TOPO	-1.09 (-0.34)	-1.13 (-0.46)	-0.96 (-0.22)
ALB	-2.58 (-0.51)	-3.46 (-0.85)	-1.70 (-0.17)
CO2	-0.42 (-0.45)	-0.58 (-0.52)	-0.25 (-0.39)
ORB	0.09 (-0.24)	0.01 (-0.25)	0.21 (-0.22)
LGM	-4.26 (-2.09)	-4.42 (-2.09)	-4.18 (-2.09)

Tab. 3.1: *Radiative forcing area-averaged anomalies in the respective experiments with respect to CTR. Numbers in brackets indicate the temperature anomalies at 2m in the respective region.*

3.3 Mean Atmospheric Changes

3.3.1 Air Temperature

In this section, the simulated atmospheric changes between LGM and pre-industrial climate are discussed and compared to paleodata. The globally averaged air temperature at 2m (t2m) as well as the t2m anomalies between the experiment ALB, CO2, ORB, TOPO, LGM and CTR are shown in Figures 3.1 and 3.2. The simulated global mean t2m in the LGM takes approximately 3000 years to equilibrate and it is about 2°C

lower compared to CTR (Fig. 3.1). As a result of changes in the orbital parameters, temperature anomalies simulated by ORB show the maximum cooling over high latitudes decreasing in magnitude equatorward (Fig. 3.2a). This extra-tropical cooling is associated with the well known temperature-albedo feedback that is enhanced in ORB due to an enhancement of snow and sea-ice cover. Moreover, the negative shortwave radiation balance in high latitudes leads to additional cooling through the reduction in the net radiation. In the tropics, the temperature differences between ORB and CTR are relatively small.

The air temperature anomalies at 2m between ALB and CTR are depicted in Figure 3.2b. As shown in Table 3.3, the ALB experiment has the largest negative radiative forcing among the experiments, except for LGM, as well as the largest globally averaged t2m anomaly (-0.5°C) (Table 3.3). Regionally, the cooling exceeds 8°C over the Laurentide ice sheets, 11°C over the Labrador Sea and 6°C in Scandinavia/Eurasia. To a large part, surface albedo changes are responsible for the cooling. It increases by around 60% over the *LGM* ice sheets, and more than 10% in Eurasia partially due to the enhanced snow accumulation. In addition, the radiative cooling associated with a dryer atmosphere enhances the global cooling tendency in the ALB experiment.

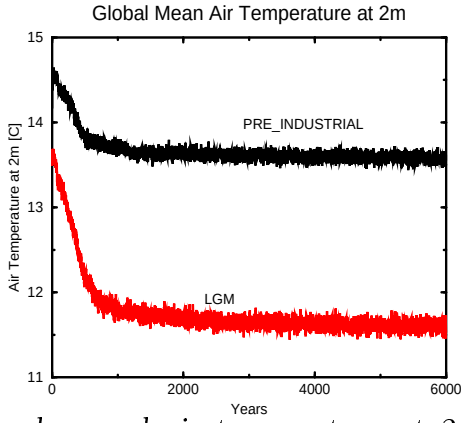

Fig. 3.1: *Globally averaged annual air temperature at 2m [°C]. LGM (red), CTR (black).*

Over tropical continents, the largest changes are due to an albedo changes originating from African and Amazon forests. Air temperature at 2m drops by up to 1.5°C in northern South America due to the bright glacial vegetation (see Fig. 2.8a), which in turn, reduces the amount of absorbed solar radiation by about $15\text{W}/m^2$. It should be noted here that the albedo changes reflect the changes in vegetation which are prescribed in ECBilt-Clio, rather than dynamically modeled. The opposite effect is observed in northern Africa and southwestern Australia, where the glacial albedo leads to an increase of absorbed surface solar radiation by $20\text{W}/m^2$ resulting in positive temperature anomalies. This LGM warming pattern in these areas is very similar to the one obtained by *Levis et al. (1999)* using a biogeochemical model. Reduced albedo generates also warmer conditions around Antarctica, but these changes are not statistically significant at the 95% level. Due to the difference in heat capacity be-

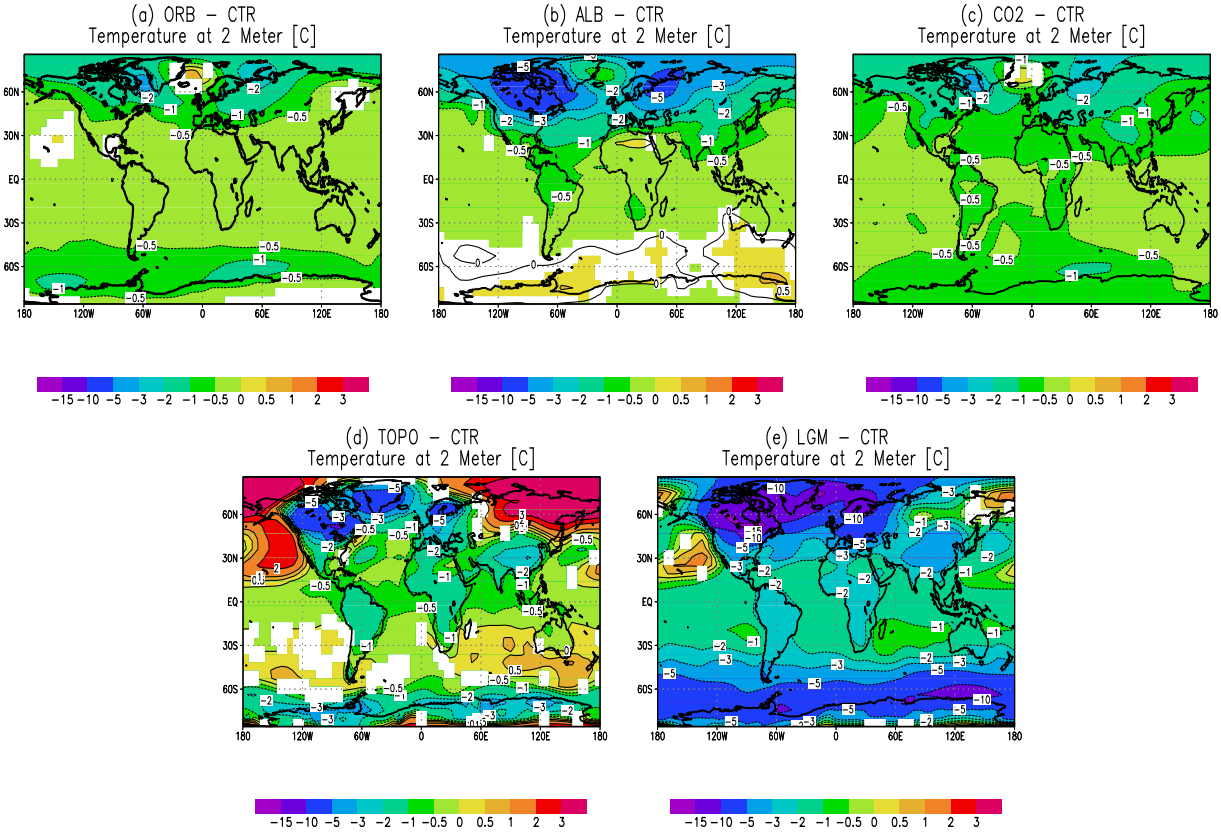

Fig. 3.2: *Annual mean air temperature at 2m [°C] ORB-CTR (a) ALB-CTR (b) CO2-CTR (c) TOPO-CTR (d) LGM-CTR (e). Shaded areas are statistically significant at 95% level based on calculations of student's t-test with 300 degrees of freedom.*

tween land and ocean, cooling over the ocean is smaller than over land. Between 30°N and 30°S, the temperature in ALB is 0.5 lower than in CTR with increasing negative anomalies towards the poles. Strong negative anomalies in the North Atlantic are the results of an extended sea-ice area as well as of cold air advection cooling the ocean and the overlying air. The t2m anomalies over the North Pacific can be attributed to an enhanced cold air advection since the sea-ice margin hardly changes.

The response of t2m to reduced CO_2 concentration (Fig. 3.2c) is characterised by a cooling in high latitudes of the same magnitude as observed in the ORB experiment (Fig. 3.2a). However, cooling over the ocean is stronger than in the ORB simulation. The cooling exceeds 0.5°C over large parts of the tropical continents. The reason for this tropical cooling can be explained in terms of a reduced longwave radiation at the surface, whereas in high latitudes ice-albedo effects can lead to local amplification of the cooling tendency.

Figure 3.2d shows the t2m anomalies as a result of including the *LGM* ice sheet topography. Regions of large cooling, by up to -10°C, can be found over North Amer-

ica, Scandinavia and over the adjacent oceans. Over land, this is simply a result of the temperature-height relationship of a stratified atmosphere. Studying this effect *Kitoh (1997)* also found that an increase in tropospheric cloudiness linked to a mountain uplift contributes to a reduction of the t2m due to its influence on the shortwave radiation. In comparison with the CTR run, the simulated cloud cover in TOPO does not increase significantly. Another mechanism responsible for the cooling resulting from the ice sheets was proposed by *Rind (1987)*. He attributed the decrease of t2m to the reduction in the mass of the atmosphere above the elevated ice sheets which reduces the greenhouse capacity and decreases the absorption of surface emitted longwave radiation. Topographically induced cooling is not homogeneous: Strong positive anomalies are simulated from northeastern Asia to the northeastern Pacific, in particular in the NH winter (not shown). In order to investigate in more details these positive t2m anomalies is shown in Figure 3.3a the radiative forcing anomalies between the TOPO and CTR. It is clearly seen (Fig. 3.3a), large positive radiative forcing anomalies from eastern Asia to northeast Pacific/Alaska leading to a warming tendency. Whereas, over North America/Greenland the negative radiative anomalies are associated with the cooling tendency. The individual contribution of net shortwave and longwave radiation for the radiative forcing anomalies (Fig. 3.3b,c) shows that the positive (negative) radiative anomalies are primary driven by changes in the longwave (shortwave) radiation. In addition to the radiative feedback, those higher t2m in the TOPO are also a consequence of stronger t2m advection resulting from the wind changes generated by the Laurentide and the eastern Siberian ice sheets (not shown).

In the SH, the negative temperature anomalies in the TOPO simulation are smaller than in the NH. They are primarily located around Antarctica as a result of a more extensive and thicker sea-ice and enhanced ice sheet topography. In the tropics, the t2m anomalies follow the SST changes, i.e. cooler (warmer) air over the North Atlantic (Pacific). Some aspects of the SST changes are discussed in the following Chapter.

The changes in t2m simulated as a result of the inclusion of the four *LGM* boundary conditions are shown in Figure 3.2e. The simulated global mean t2m for the LGM is 2.09°C lower than in CTR (Table 3.3). This cooling is consistent with that simulated by other GCM simulations *(e.g. Shin et al. 2003; Wyputta et al. 2001; Rind 1987)*.

As discussed above, the presence of the ice sheets cools the climate mainly as a result of the lapse rate and albedo effects, and reduced greenhouse capacity of the atmosphere. *Rind 1987* argued that the increased land ice elevation cools the surface in winter, while the albedo changes cool the surface in summer. The changes in CO_2 and in orbital parameters play a secondary role. The maximum near surface cooling in LGM exceeds 20°C in high latitudes in both hemispheres. In the NH, the largest decrease in temperature is located over the ice sheets and the North Atlantic while in the SH it is simulated around Antarctica. The higher temperatures over land in Eurasia and the North Pacific as simulated by TOPO are also captured in LGM. Including *LGM* albedo, reduced atmospheric CO_2 concentration and orbital forcing leads to reduced warming in the LGM with respect to TOPO. Although the link between the *LGM* topography and the warmer North Pacific is evident (Fig. 3.2d,e), the changes are more complicated over other oceanic areas. For instance, the temperature response to reduced CO_2 concentration and the changes in orbital parameters oppose the tempera-

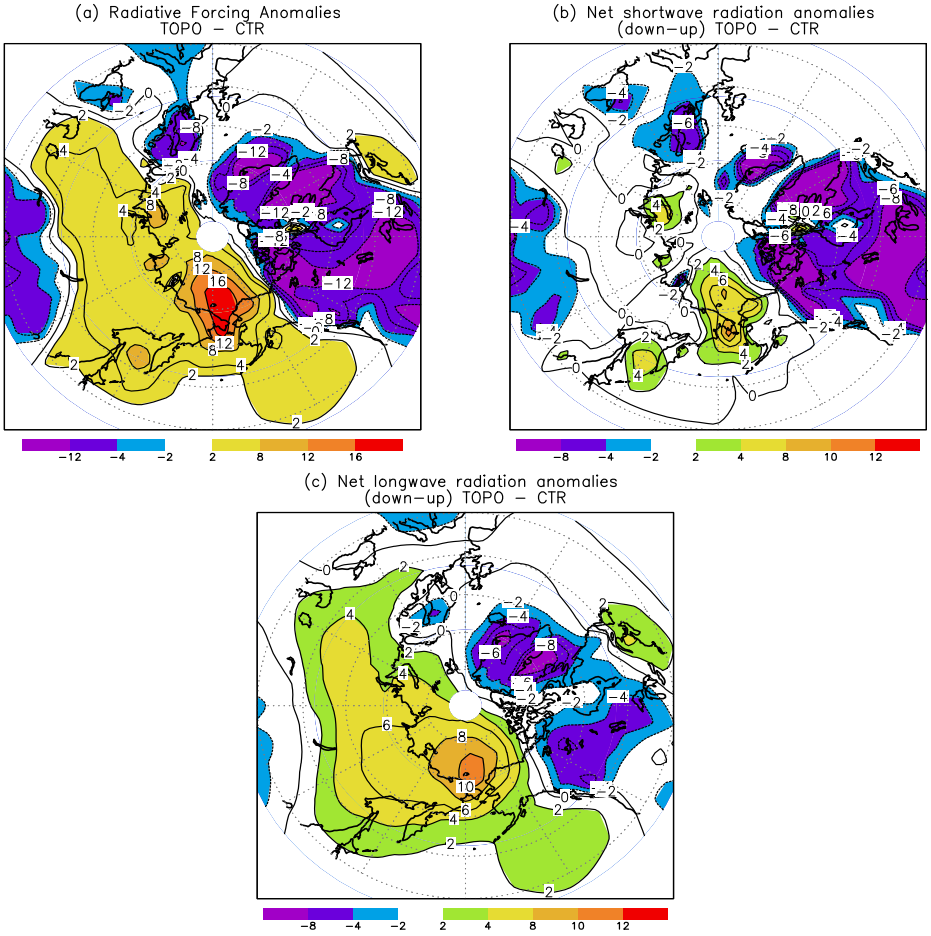

Fig. 3.3: *Radiative forcing anomalies [Wm^{-2}] between TOPO and CTR (a), and the respective contribution of the net shortwave radiation (b) and net longwave radiation (c).*

ture response due to topographic forcing over the SH oceans, where warmer conditions in TOPO are replaced by cooler conditions in LGM. This illustrates that despite the weaker temperature response to reduced CO_2 concentration and orbital changes these boundary conditions are crucial to establish the temperature pattern in the LGM.

The t2m anomalies between LGM and CTR for DJF and JJA are shown in Figure 3.4a,b. As expected, the largest changes are simulated over the NH. During DJF, the temperature drops by up to 15°C over North America/Atlantic and central Europe. The anomalies in the tropics are smaller, in particular over the Pacific Ocean. These temperature changes are linked to changes of the atmospheric circulation, and an increase in snow cover and sea-ice associated to the well-known temperature-albedo feedback. On the other hand, the higher temperature simulated in DJF (Fig. 3.4a) extending from eastern Asia to Alaska is a result of three major effects: (1) radiative forcing changes, (2) weakened latent and sensible heating due to a weakening of the

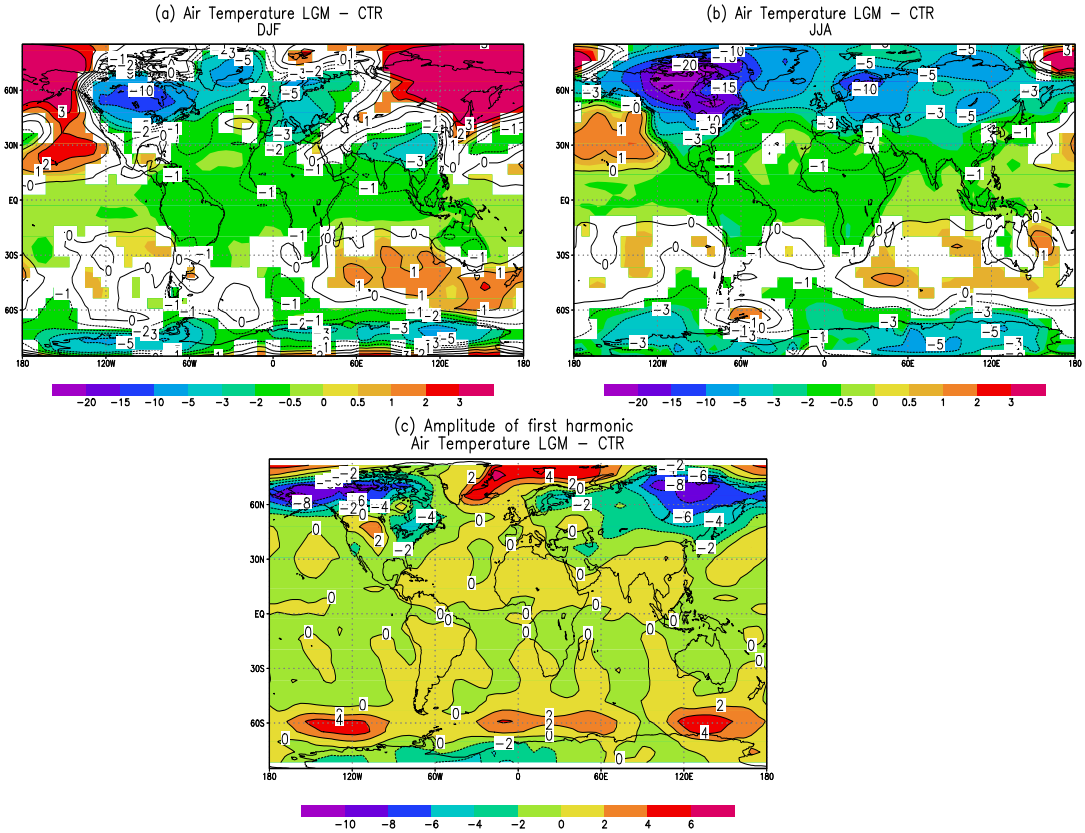

Fig. 3.4: *Air temperature anomalies at 2m [°C] for LGM-CTR (a) DJF (b) JJA and (c) amplitude of the first harmonic. Shaded areas in (a) and (b) are statistically significant at 95% level based on calculations of student's t-test with 300 degrees of freedom.*

westerlies and (3) changes of ocean dynamics. In the tropics, however, the simulated temperature changes are mainly a result of the ocean dynamics and a reduction of water vapour in the atmosphere that reduces the backscattering of longwave radiation. Changes in specific humidity are addressed in the next section. In the large part of the SH, the temperature changes are not statistically significant at 95% level[1] , except for Antarctica and in the Indian/southern Australia sector. This region shows an unexpected warming that has not been found in other *LGM* simulations. It may be a result of weaker westerlies associated with the presence of Antarctica ice sheet. Figure 3.4b depicts the temperature anomalies in JJA. Compared to DJF, JJA shows an enhanced cooling in the extra-tropics with temperature anomalies lower than -20°C over the Laurentide ice sheet. In addition, the cooling is extended equatorward over land. This is the result of an increase in snow accumulation to the south of the ice sheets in LGM that is not found in the CTR simulation. Another striking feature is the seasonality of the positive temperature anomalies over the Bering Strait region and

[1] A student's t-test is performed here using 300 degrees of freedom.

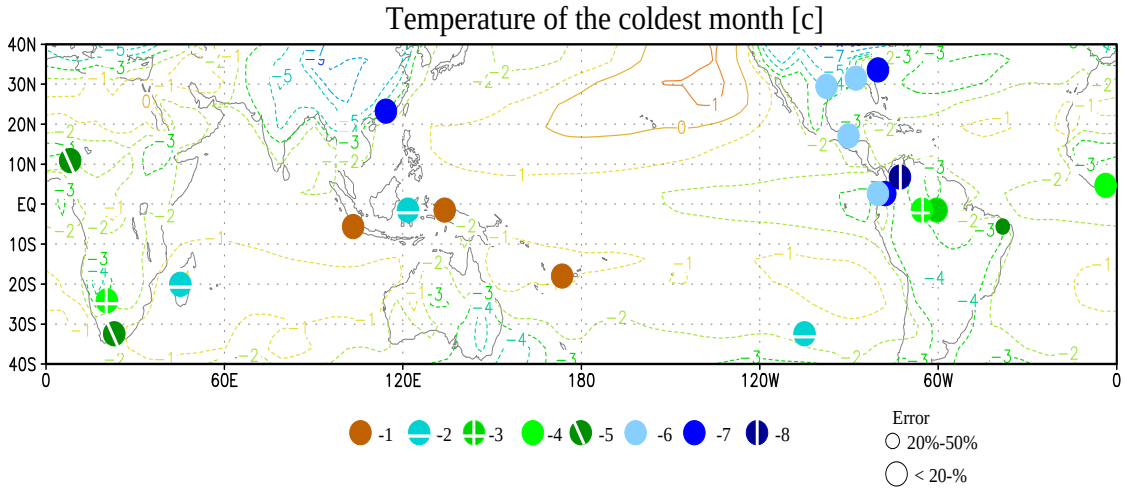

Fig. 3.5: *$\Delta MTCO$ [°C] (LGM - CTR) at sea level from Farrera et. al (1999) dots. Simulated LGM-CTR (contour).*

eastern Asia. In the tropics and the SH, the temperature changes are similar to those simulated during DJF.

Figure 3.4c shows the difference in amplitude of the first annual harmonic between LGM and CTR. This quantity provides an estimate of the temperature difference between the coldest and warmest months in the simulations. The figure reveals that during the *LGM*, the seasonal variability is strongly reduced over high latitudes in the NH. The analysis of the annual harmonic of the sensitivity runs (not shown), reveals that the seasonal variability over North America is mainly driven by modified albedo while over the east Asia/North Pacific the topographic changes play the most important role due to its impact on the mid-latitude westerly flow.

Based on records of vegetation changes and of noble gas in ground water measurements, *Farrera et al. (1999)* provide paleoclimate estimates of the changes of mean temperature of the coldest month (MTCO) in the area between 32°S and 33°N (Table 3.2, Fig. 3.5). These estimates indicate that during the *LGM* the MTCO was between 2 and 9°C cooler than at present. Table 3.2 shows the MTCO over some regions as defined by *Pinot et al. (1999)*. The comparison between the simulated temperature and the paleo-reconstructions shows good agreement in the equatorial zone. Over the subtropics, however, the model underestimates the cooling. As depicted by Figure 3.5, the magnitude of the cooling is not uniformly distributed. For instance, northeastern Brazil, northwestern South America and southeastern North America cooled by more than 5°C. This feature is not reproduced in the LGM experiment that shows much warmer temperatures over these areas. Compared to the NCAR-CCSM of *Shin et al. (2003)* the ECBilt-Clio LGM is in general warmer.

3.3.2 Moisture

Glacial temperature anomalies lead to a weakening of the global hydrological cycle. This in turn changes the amount of atmospheric water vapour. The specific humidity anomalies integrated from the surface to 500hPa in ALB show an increase in specific humidity in the tropics and the SH. Nevertheless, the inclusion of ice sheet albedo over North America and Scandinavia drastically reduces the water vapour content of the atmosphere over those areas.

The zonally averaged specific humidity anomalies for the sensitivity runs are shown in Figure 3.6. The reduction of atmospheric CO_2 concentration and the changes in orbital parameters only have a small impact on the atmospheric water vapour. Diagnosed changes in topography and albedo are mainly responsible for the dryer atmosphere in the NH in the LGM (Fig. 3.6). The structure in the SH is more complicated. Despite the positive anomalies in TOPO and ALB, the LGM shows a substantial reduction in the specific humidity. Comparing the zonal mean changes in specific humidity and surface temperature anomalies (see Fig 3.2) reveals that the amount of water vapour in the atmosphere is tightly coupled to the changes in air/sea temperatures. For example, in TOPO and ALB the surface temperature is warmer than in CTR in most parts of the SH, in agreement with the positive specific humidity anomalies. On the other hand, lower temperatures lead to negative humidity anomalies as a result of reduced evaporation in the LGM. In addition to this local effect also the atmospheric circulation contributes to humidity changes through the water vapour transport by winds. The relationship between humidity changes and transient eddy activity in particular will be discussed in the end of this Chapter.

$\Delta MTCO$	NCAR-CCSM Shin et al. (2003)	ECBilt-Clio area-average	Farrera et al. (1999) Minimum / Maximum
ESA	-3.5	-3.0	-3.0 / -8.0
EEA	-3.5	-1.9	-3.0 / -5.0
NG	-3.6	-1.2	-2.0 / -7.0
SSA	-5.0	-2.4	-3.7 / -6.5
SENA	-4.4	-1.9	-7.5 / -15.5

Tab. 3.2: *Glacial-age changes in mean temperature of the coldest month ($\Delta MTCO$) over Equatorial South America (***ESA** *- 50-75°W,10°N-2°S), Equatorial East Africa (***EEA** *- 25-45°E,10°N-10°S), New Guinea (***NG** *130-150°E,0-10°S), Subtropical South Africa (***SSA** *- 15-35°E,15-35°S) and Subtropical Eastern North America (***SENA** *- 75-85°W,30-35°N). The minimum and maximum represent the minimum and maximum $\Delta MTCO$ within the regions among the proxy-data. The simulated $\Delta MTCO$ in the LGM experiment is shown for comparison. The table is derived from Shin et al. (2003).*

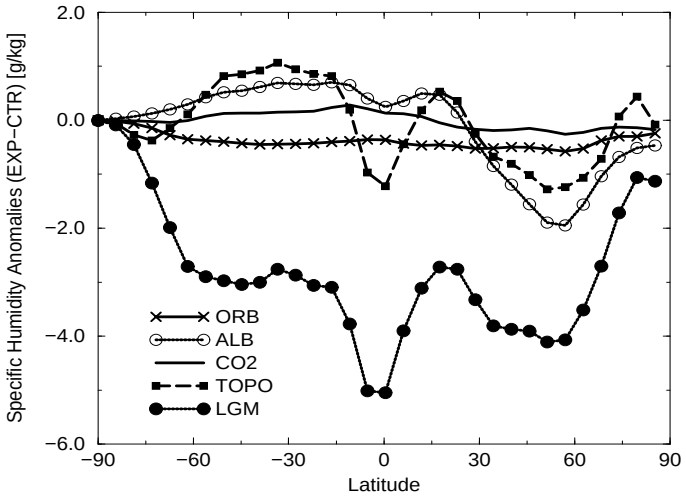

Fig. 3.6: *Time averaged annual zonal mean specific humidity anomalies with respect to CTR in the different sensitivity experiments [g/kg].*

3.3.3 Stationary Waves

As discussed by *Cook and Held (1988)* glacial ice sheets increase the zonal asymmetries - stationary waves - of the atmospheric circulation. Furthermore, the other *LGM* boundary conditions affect the stationary waves through the diabatic forcing and vorticity flux anomalies. To analyse the response of stationary waves to the *LGM* boundary conditions the simulated anomalies in eddy geopotential height[2] at 500 hPa between CTR and the sensitivity experiments are shown in Figures 3.7 and 3.8. During DJF, the anomalies between ALB and CTR (Fig. 3.7b) show an enhanced wave train across Canada into Greenland that represents an amplification of the ridge-trough pattern simulated in CTR. Furthermore, the high pressure over Europe weakens in ALB as compared to CTR.

Most changes due to reduced atmospheric CO_2 concentration are not statistically significant at a 95% level (Fig. 3.7c) except for the low pressure systems over Canada and Europe. The changes due to the *LGM* orbital parameters (Fig. 3.7d) are very similar to those described for CO2 and ALB. Changes in the geopotential height in ALB, CO2 and ORB seem to be related to the diabatic heating changes, since these experiments show similar diabatic heating pattern (not amplitude) as a result of increased albedo feedback. In the SH, ALB, CO2 and ORB show very weak eddy geopotential anomalies in DJF. Now the changes in JJA are discussed for these experiments, leaving discussion of the DJF for TOPO and LGM experiments for the end of this section. During JJA, the striking feature in ALB is the intensification of the trough over the Laurentide ice sheet (Fig. 3.8b). This anomalous trough creates a cyclonic cell with northward (southward) flow over eastern (western) North America, which induces at the eastern (western) coast of North America slightly higher (lower) surface air tem-

[2] The eddy geopotential height is defined as the geopotential height with the zonal mean removed.

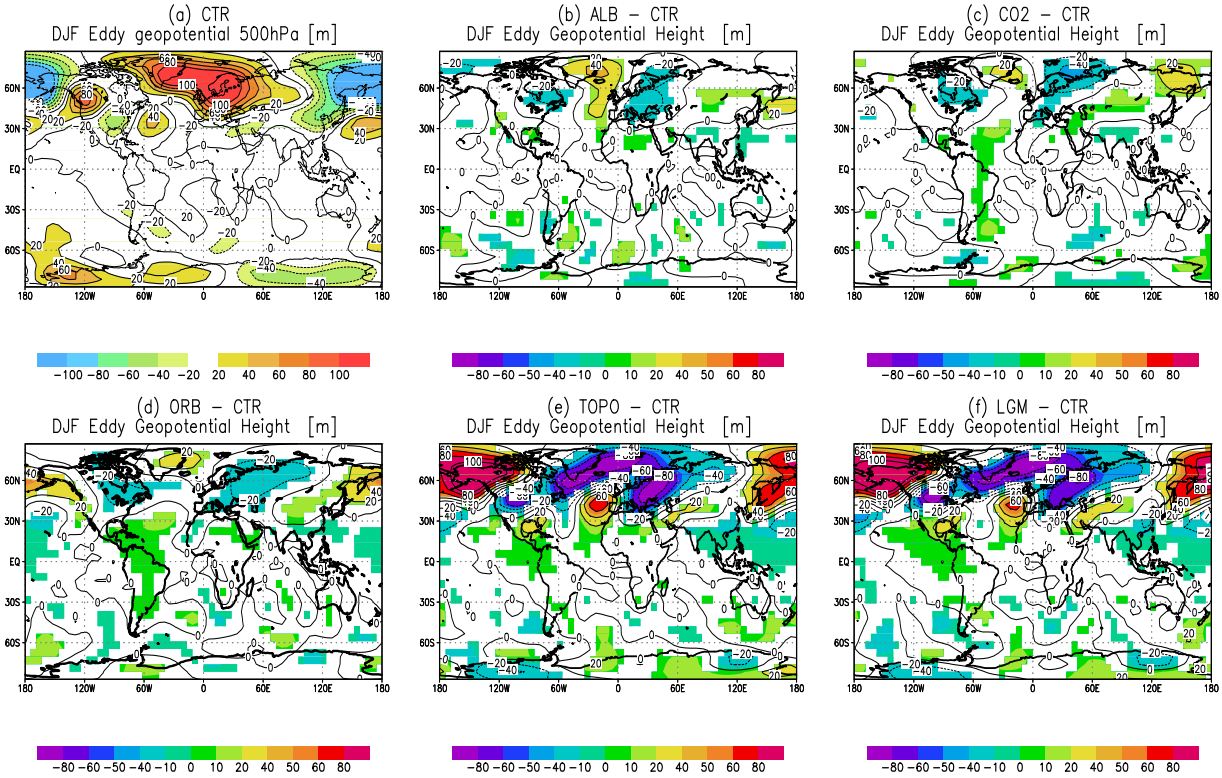

Fig. 3.7: *DJF eddy geopotential height at 500hPa [m] in CTR (a) and the differences ALB-CTR (b) CO2-CTR (c) ORB-CTR (d) TOPO-CTR (e) LGM-CTR (f). Shaded areas are statistically significant at 95% level based on calculations of student's t-test with 300 degrees of freedom.*

perature, as also found by *Rind (1987)*. A ridge over the North Pacific is established in response to the diabatic forcing of ALB. The generation of the low pressure system over North America in ALB can be explained in terms of geopotential tendency and omega equations as described by *Holton (1972)*. It is a direct consequence of positive vorticity and differential thickness advection. The differential thickness advection is defined as the rate of decrease of temperature advection with height. The fall in geopotential height in ALB can be understood as a result of the increase in the cold air advection into the air column below the 500hPa trough. It leads to a reduction of the thickness of the column, and hence the height of the 500hPa surface decreases. This mechanism is discussed in more detail in the paragraphs concerning the LGM. The stationary wave anomalies due to changes in CO_2 and the orbital parameters are very similar and confined to high latitudes. It emphasises the influence of changes in these boundary conditions in the extra-tropics.

To investigate the eddy geopotential anomalies resulting from changes in topography, a series of additional experiments in which the Laurentide ice sheet height is

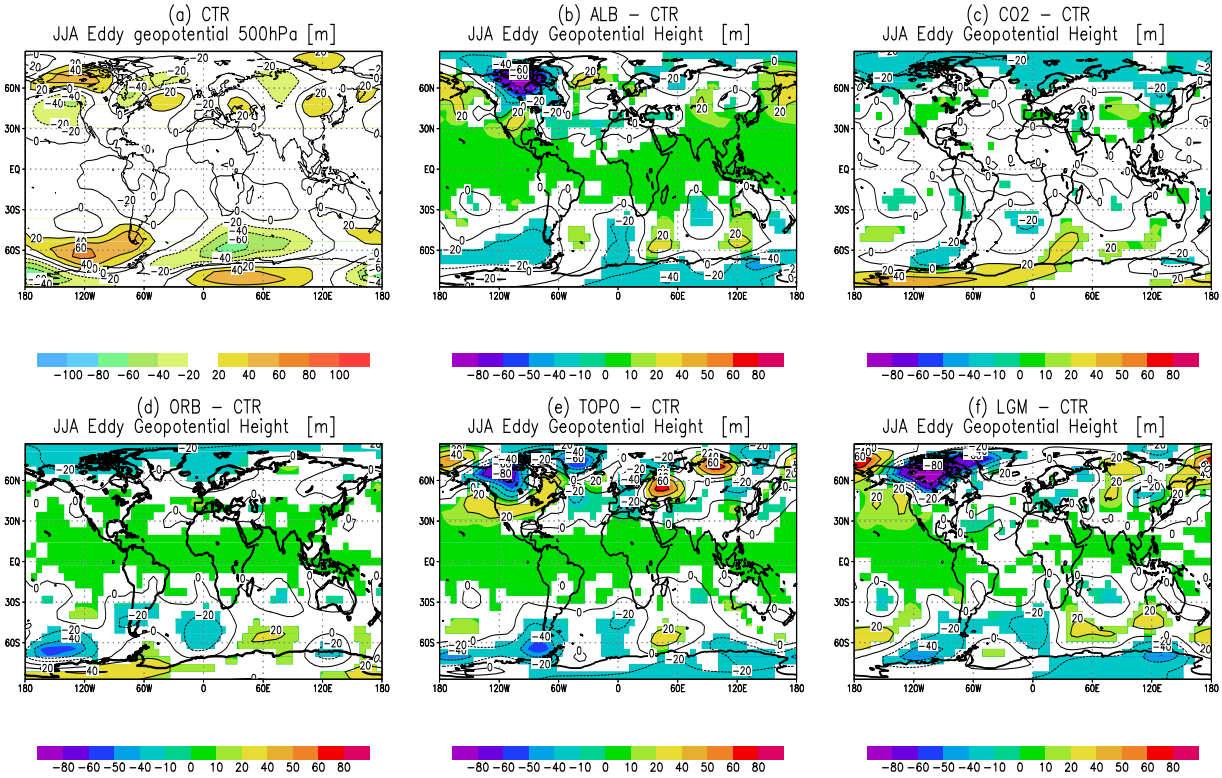

Fig. 3.8: *JJA eddy geopotential height at 500hPa [m] in CTR (a) and the differences ALB-CTR (b) CO2-CTR (c) ORB-CTR (d) TOPO-CTR (e) LGM-CTR (f). Shaded areas are statistically significant at 95% level. Based on calculations of student's t-test with 300 degrees of freedom.*

multiplied by a factor of 0.25, 0.5, 1.5 and 2 (hereafter 0.25an, 0.5an, 1.5an and 2an) is performed. Elsewhere the topography is kept as in LGM (factor = 1). Figure 3.9 shows the zonally averaged topography of North America for each experiment. LGM and CTR are also plotted for comparison. The main conclusion from previous studies concerning the atmospheric response to topographic barriers, such as the Laurentide ice sheet *(Cook and Held 1992; Cook and Held 1988; Rind 1987)*, is that the Laurentide ice sheet enhances the upstream long wave ridge and the downstream long wave trough, as depicted in Figure 3.7e. *Cook and Held (1992)* argued that the stationary waves' response to small topographic changes can be satisfactorily reproduced by a linear model. In contrast, it is found that for large mountains the linear response breaks down. Figure 3.10 shows the eddy geopotential height anomalies simulated by the topography experiments. In the 0.25an experiment (Fig. 3.10a) there is a clear stationary wave train with an enhanced anticyclonic flow to the west and a cyclonic flow to the northeast of the topography anomalies. A similar but weaker wave train is also found over North America in 0.5an experiment (Fig. 3.10b). This weakening in the ridge-trough pattern depicted in 0.5an reveals that decreasing the height of topo-

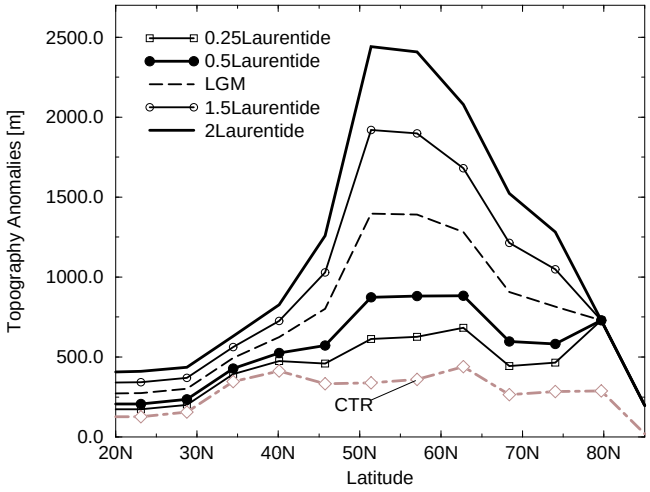

Fig. 3.9: *Zonally averaged topography in North America for different topographic experiments [m].*

graphic barrier with respect to LGM tends to reduce the amplitude of the downstream low and the upstream high.

From an increase of the height of Laurentide ice sheet (Fig. 3.10c,d), one can conclude that the low pressure system located over northern North America in LGM is replaced by a high pressure. In addition, a trough over the Nordic Seas and Greenland replaces the ridge simulated in 0.25an and 0.5an experiments. The development of the high pressure system over North America can be understood as a result of a cold high at surface and a divergent (anticyclonic) induced flow due to the downward vertical velocity (*Holton 1972).* The topographic experiments performed here show that the generated wave train in the LGM is tightly related to the topographic barrier height.

The comparison of the sensitivity experiments shows that in DJF the topographic changes play the most important role to set up the glacial stationary wave pattern (Fig. 3.7). The changes in CO_2 and the orbital parameters also play an important role to intensify the trough over Europe as well as the ridge over the North Pacific. During JJA, however, the stationary waves are strongly affected by the ice sheet albedo in particular over North America. The role of reduced CO_2 and the orbital parameters during the austral winter is secondary to the stationary waves in the LGM. These results are consistent with AGCM result of *Rind (1987).*

As briefly discussed for ALB experiment, the negative temperature and the positive vorticity advections contribute to reduce the geopotential height in 500hPa according the geopotential tendency equation (Eq. 3.2).

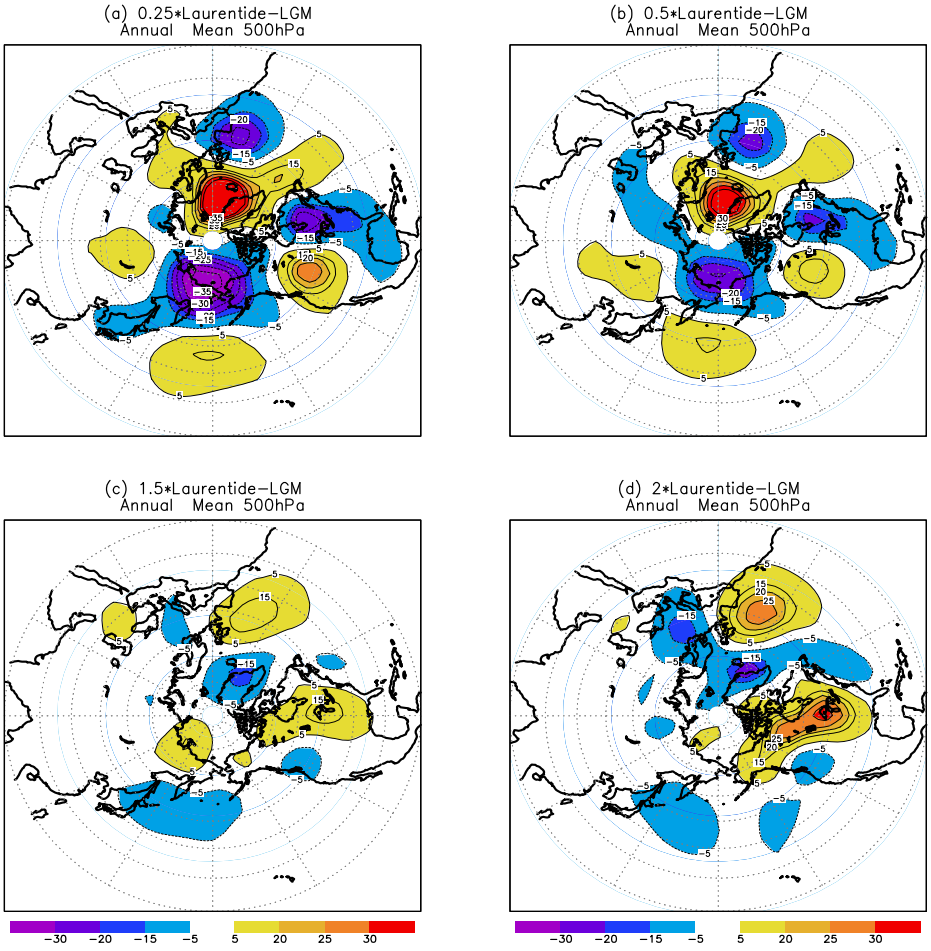

Fig. 3.10: *Time averaged annual mean eddy geopotential height anomalies at 500hPa between the topographic experiments and LGM [m]. See text for details.*

$$\underbrace{\left[\nabla^2 + \frac{\partial}{\partial p}\left(\frac{f_0^2}{\sigma}\frac{\partial}{\partial p}\right)\right]}_{A}\chi = \underbrace{-f_0 \mathbf{V_g}\cdot\nabla\left(\frac{1}{f_0}\nabla^2\Phi + f\right)}_{B} \underbrace{-\frac{\partial}{\partial p}\left[\frac{f_0^2}{\sigma}\mathbf{V}_g\cdot\nabla\left(\frac{\partial\Phi}{\partial p}\right)\right]}_{C} \tag{3.2}$$

where the geopotential tendency $\chi \sim \frac{\partial\Phi}{\partial t}$

The geopotential tendency equation provides a relationship between the local change of geopotential and the distribution of vorticity and thickness advection as can be seen by analysing the three terms labelled A,B, and C, respectively. The term B, vorticity advection term, cannot change the strength of synoptic system at the levels where

the advection is occurring but only acts to propagate the disturbance horizontally and spread it vertically. The major mechanism for amplification or decay of the midlatitudes synoptic system is contained in term C. This term, the thickness advection, tends to be largest in magnitude in the lower troposphere beneath 500 hPa trough and ridge. As discussed by *Holton (1972)* since $\frac{\partial \Phi}{\partial p}$ is proportional to temperature, the thickness advection is proportional to the temperature advection. Thus, term C in (3.2) is proportional to the rate of temperature advection with respect to the height. This term is usually referred as the differential temperature advection. In order to

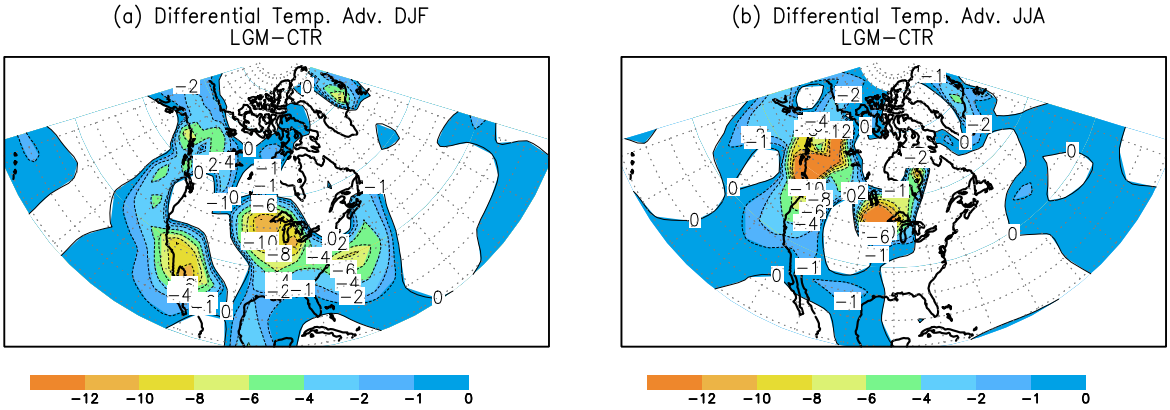

Fig. 3.11: *Rate of change of temperature advection with respect to height. Differences between LGM and CTR experiments* $[10^{-5} \times {}^{\circ}C\ s^{-1}]$ *(a) DJF (b) JJA.*

examine the influence of the differential temperature advection on the changes in the eddy geopotential height anomalies over North America, is shown in Figure 3.11 the differential temperature advection anomalies between the LGM and CTR experiments. The differential temperature advection is the difference between the temperature advection at 650 hPa and the temperature advection at the surface for the respective simulation (i.e., $V_{650} \cdot \nabla T_{650} - V_{sur} \cdot \nabla T_{sur}$). The Figure 3.11 shows a reduction in the differential temperature advection over the most part of North America, in particular during DJF. It represents an increase of cold temperature advection. Thereby, cold air into the air column below the 500 hPa trough reduces the thickness of the column and hence decreases the geopotential height. It is important to note that the contribution of the diabatic heating is neglected in the Equation 3.2, even though it may be very important to intensify the trough in particular over the North Atlantic.

3.3.4 Baroclinic Instability

Large-scale temperature and atmospheric circulation changes have the potential to modify also the statistics of transient waves. These are predominantly generated by baroclinic instabilities of the background flow. In order to investigate changes in baroclinic instability due to glacial boundary conditions is studied the simulated changes of the Eady growth rate (σ_{BI}) *(Lindzen and Farell, 1980)*. It is a measure for baroclinicity in the atmosphere and can be used to quantify the potential for instability

and cyclone growth. The Eady growth rate estimates baroclinic instability through the vertical wind shear and the static stability in the atmosphere. It is defined as $\sigma_{BI} = 0.31\frac{f}{N}|\partial\mathbf{v}/\partial z|$ where f is the Coriolis parameter, N the Brunt-Väisälä frequency, z the upward vertical coordinate and $\mathbf{v}$ the horizontal wind. Based on observational data, one observes that the growth rate is high over the North Pacific and North Atlantic during the boreal winter season. Furthermore, it is shifted with respect to the storm track maxima. The storm track maxima can be found to the east coast of Asia and North America. *Hall et al. (1994)* attributed the spacial extension in high values of σ_{BI} from southern Asia to Pacific to changes in static stability and the meridional temperature gradient. In order to quantify the role of the meridional temperature gradient and static stability, both terms are analysed separately. The ECBilt-Clio simulation suggests that the long "tail" of σ_{BI} over eastern Asia originates from the strong vertical wind shear, rather than from the atmospheric stratification. The static stability contributes to σ_{BI} amplitude but do not control their spacial distribution. Comparing Figure 3.12a with Figure 1a of *Paciorek et al. (2002)* reveals that the simulated σ_{BI} is reproduced quite well in comparison to the NCEP reanalysis. The two storm track regions are well represented over the western Atlantic and the Pacific. They reflect high baroclinic instability with potential to drive storm track dynamics.

Figure 3.12b shows the σ_{BI} anomalies between ALB and CTR during DJF. The changes in surface albedo are associated to lower growth rates in the Pacific storm track region and slightly higher growth rates over Scandinavia/central Asia and parts of North America. These features are a consequence of the changes in wind shear that decreases (increases) over the Pacific storm track (Eurasia and North America) (not shown). The contribution of the static stability (not shown) also reinforces the σ_{BI} due to smaller vertical thermal gradient in the ALB simulation. In agreement with the weaker meridional thermal gradient in the SH (see Fig. 3.2), a reduction of σ_{BI} can be found over Antarctica between the date line and 90°W.

The differences between the simulated Eady growth rate under reduced atmospheric CO_2 concentration and the CTR run are shown in Figure 3.12c. In general, the CO2 run exhibits similar anomalies as the ALB experiment. The strengthening in baroclinic instability over North America in the CO2 run may have played a crucial role in the maintenance of the Laurentide ice sheets in the real world (I come back to this point in more detail in the section concerning the transient eddies). The enhancement of the vertical wind shear over North America generates positive anomalies in σ_{BI}. Substantial changes in baroclinic instability are also simulated by ORB, as shown in Figure 3.12d. Comparing ORB and CO2 with ALB (Fig. 3.12b,c,d), one concludes that the climate mechanisms acting in ALB also take place in ORB and CO2. Positive σ_{BI} in these experiments results partially from an enhanced snow coverage and higher albedo, thereby, steeping the meridional thermal gradient.

As found by *Hoskins and Valdes (1990)*, also changes in the stationary waves have a direct impact on the baroclinicity and dynamics of the storm tracks. Since the stationary waves are directly affected by topographic changes such those imposed by the NH ice sheets during the *LGM (Cook and Held 1988, Broccoli and Manabe 1987, Rind 1987)*, one may expect larger changes of σ_{BI} in the TOPO experiment. Figure 3.12e displays the σ_{BI} anomalies between TOPO and CTR during DJF. In comparison with

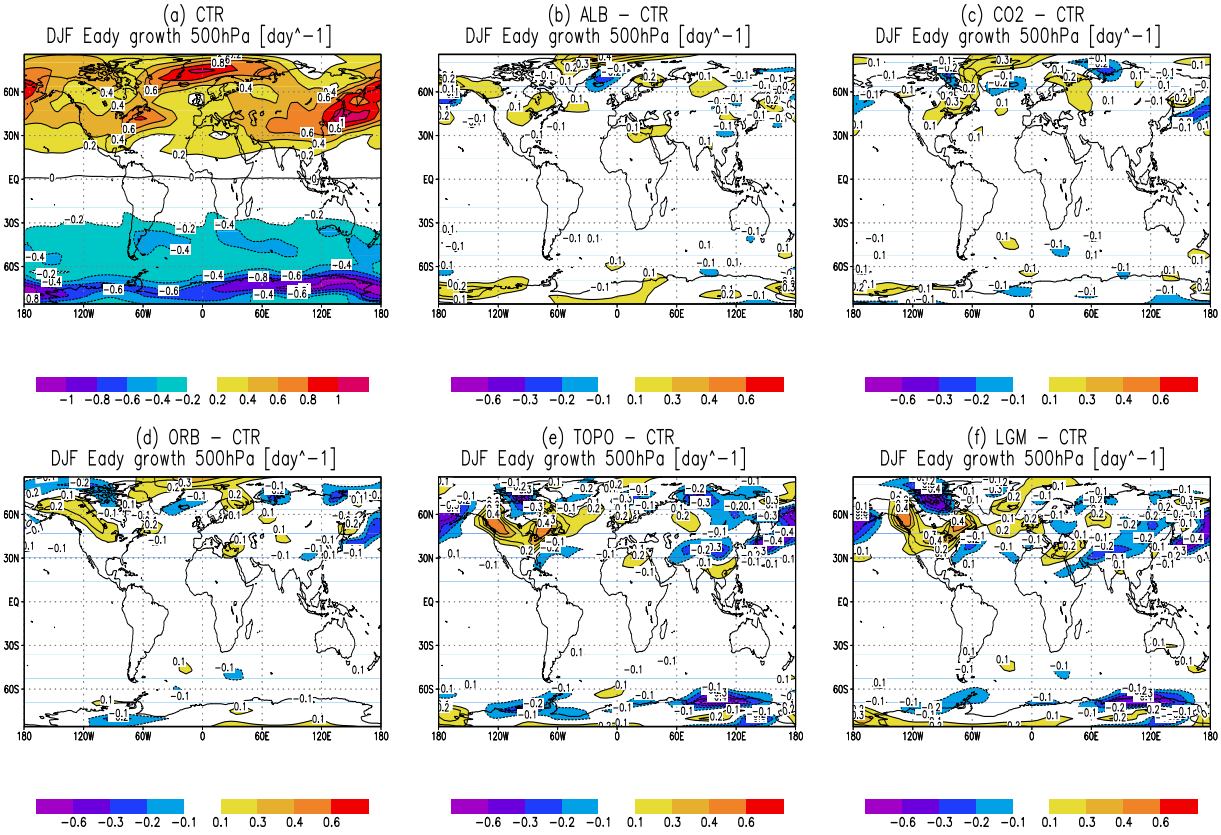

Fig. 3.12: *Time averaged Eady growth rate in DJF [day^{-1}] in CTR (a) and the sensitivity experiments anomalies. ALB-CTR (b) CO2-CTR (c) ORB-CTR (d) TOPO-CTR (e) LGM-CTR (f).*

ALB, CO2 and ORB, TOPO shows a much stronger baroclinic instability over North America. However, the changes in northern Europe are smaller than those simulated by ALB, CO2 and ORB suggesting a negative topographic feedback. The higher σ_{BI} anomalies over North America are a direct response to the enhanced meridional thermal gradient and vertical wind shear (not shown). The cold climate simulated over the northern North America in TOPO (Fig. 3.2d) is confined to the latitudes north to 40°N. Thus, an enhanced meridional temperature contrast leads to stronger vertical shear of the zonal wind due to the thermal wind relation. Over North America the wind shear in TOPO is twice stronger than in the ALB and almost three times stronger than that simulated in CO2 and ORB. This enhanced vertical wind shear and the weaker static stability resulting from the modified topography play a very important role in the maintenance of the *LGM* climate because they change both the shape and the position of the storm tracks, as found by *Bromwich et al. (1993)*. Nevertheless, in the LGM simulation the region of maximum baroclinic activity is reduced in the Pacific storm track region. In the SH, except over Antarctica, σ_{BI} hardly changes. The LGM anomalies are discussed at the end of section.

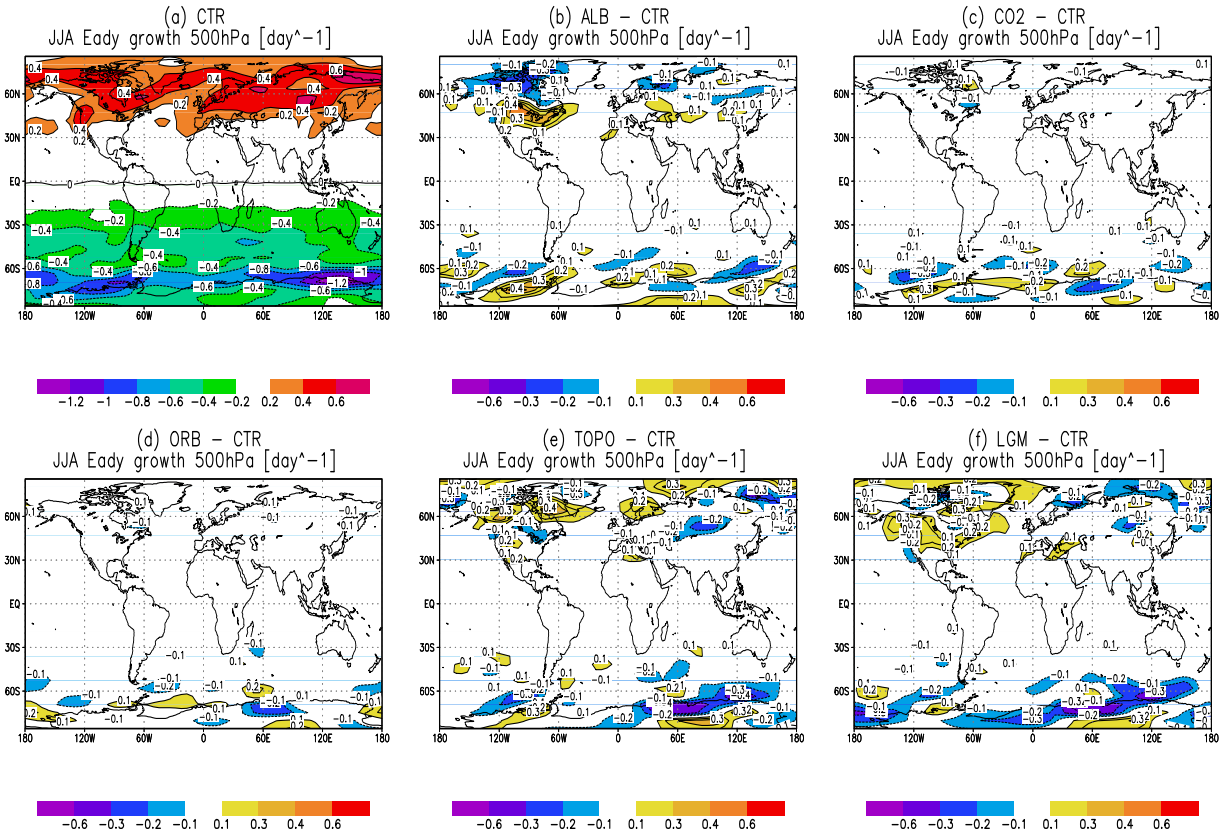

Fig. 3.13: *Time averaged Eady growth rate in JJA [day^{-1}] in CTR (a) and the sensitivity experiments anomalies. ALB-CTR (b) CO2-CTR (c) ORB-CTR (d) TOPO-CTR (e) LGM-CTR (f).*

In CTR run during the NH summer, σ_{BI} shows a higher growth rate over Scandinavia and Eurasia than during the NH winter (Figure 3.13a). In Eurasia the larger meridional thermal gradient between the warmer continent and the colder Arctic Ocean enhances the wind shear. However, in the storm tracks region, σ_{BI} is extremely reduced. In part, this reduction of synoptic activity can be attributed to reduced meridional temperature contrasts linked to the retreat of the sea-ice margin in the north North Atlantic. This retreat is even more important in the Labrador Sea and in the northwestern Pacific. A remarkable feature during JJA in the SH is the σ_{BI} split into two parts: one centred at about 35°S and another following the Antarctica sea-ice edge. This agrees with the dual westerlies structure during the SH winter as discussed by *Trenberth (1991)*.

A well defined baroclinic zone over North America results from the inclusion of *LGM* albedo (Fig. 3.13b). This region is affected by a reduction of the static stability (by more than 40%) as well as an increase in the vertical wind shear (by about 60%). The increased meridional thermal contrast over North America can be attributed to the albedo distribution, high albedo due to the ice sheet and lower albedo over southern

North America. ALB also shows an increase in σ_{BI} in Europe and western Asia. This intensification is not as strong as that simulated over North America. The relevance of the vertical wind shear in determining the baroclinic structure of the atmosphere is nicely illustrated in the area of the Canadian Islands. The strong reduction of the static stability in ALB is not able to create higher σ_{BI}, due to the reduction of vertical wind shear in this area (not shown). In the SH, the most important change between the ALB and CTR experiments is simulated close to the Antarctic sea-ice margin as found during the NH winter. The σ_{BI} anomalies CO2-CTR and ORB-CTR do not show any significant change. In TOPO, however, baroclinic instability is increased over north Canada and the Labrador Sea and extended to Scandinavia. (Figure 3.13e). The surface temperature anomalies in TOPO with respect to CTR have a particular structure in JJA (Fig. 3.2d) which leads to changes in the baroclinic instability. As discussed by *Rind (1987)*, the elevation of the ice sheets amplifies the cooling over land in DJF, while in JJA, slightly higher temperatures are found over Eurasia and North America as a result of the subsidence of air south and east of the ice sheets. Part of this warming may also be influenced by stronger northward flow. The cooling in the north and warming in the south provides the energy necessary to enhance the wind shear, thus, strengthening the baroclinic activity.

LGM Simulation

A comparison of the anomalies of σ_{BI} simulated by the LGM and simulated by the other sensitivity experiments reveals the dominance of topographic changes. This is in particular true over the NH during DJF. The anomalies of the vertical wind shear and of the simulated static stability in TOPO are also the predominant features in the LGM. The resulting σ_{BI} changes in LGM are slightly larger over North America, eastern North Atlantic and Nordic Seas than in TOPO. This suggests that the σ_{BI} response simulated by TOPO is amplified by the other glacial boundary conditions. This indicates that the contributions of the orbital forcing, CO_2 and albedo play a significant role to increase σ_{BI} over those areas (Figure 3.12f).

The baroclinic activity in the Pacific storm track region is extremely reduced in the LGM simulation as a result of the weakening of the vertical wind shear. The weaker wind shear results from the reduced meridional thermal gradient linked to warmer SST in the North Pacific that is simulated in ORB and TOPO. In the SH, the LGM changes are almost similar to those of TOPO capturing the difference of Antarctica topography between the LGM and CTR. Another source for circulation changes in the SH was discussed by *Rind (1987)*, it seems to result from increased stationary wave activity in the NH which affects the SH via cross equatorial energy transport, or through the meridional extent of the waves.

During JJA, the LGM anomalies seem to be mainly related to changes in land surface albedo. Over North America (Scandinavia), the LGM shows higher (lower) σ_{BI} than in CTR. Similar features are also observed in ALB (see Figures 3.13b, 3.13f). On the other hand, the enhanced baroclinic activity found in the LGM over the Labrador Sea and Greenland is basically driven by changes in topography. In the SH, the largest anomalies are confined to the Antarctic sea-ice margin where the changes in topography play the leading role.

3.4 Changes in Transient Eddy Activity

3.4.1 Diagnostics

The diagnostic work of *Blackmon (1976)* provides a framework to quantify the activity of extra-tropical cyclones. The well-known "storm tracks"[3] capture the areas of maximum transient wave activity. Evidence from paleoclimatic sources and modeling studies suggest that the *LGM* storm tracks contributed significantly to the high latitude ice sheet mass budget. Based on an analyses of oxygen isotopo *Kapsner et al. (1995)* concluded that the atmospheric circulation exerted the main control on snow accumulation in Greenland over the past 18 kyr, rather than the temperature. Furthermore, *Bromwich et al. (1993)* attributed the changes in snow accumulation in central Greenland during the period 1963-1988 to the position and strength of the storm track. In order to obtain an accurate estimate of the intensity of the storm tracks the statistics of the transient waves in investigated. In the following, transient eddy activity is analysed in terms of the low level eddy heat flux $[(\overline{v'T'})]$, the eddy kinetic energy $[EKE = \frac{1}{2}(\overline{u'^2 + v'^2})]$ and the E vector $[E = (\overline{v'^2 - u'^2}, \overline{-u'v'})]$, with the overbars denoting the time mean and primes the deviation therefrom. The transient eddies are extracted from daily model data and have been temporally filtered using a high-pass filter to include only systems with growth and decay with timescales smaller than 6 days.

The DJF $\overline{v'T'}$ pattern simulated in the CTR (Figure 3.14a) reproduces quite satisfactorily the observations except for an overestimation over the North Pacific as a result of the strong simulated zonal wind component. There are several reasons for why the zonal mean wind determines transient eddy activity. A strong jet is often associated with increased baroclinic and barotropic instability resulting in enhanced transient wave activity. Furthermore, *Trenberth (1991)* showed that a strong jet also advects transient wave activity further to the east.

The difference in $\overline{v'T'}$ between ALB and CTR is displayed in Figure 3.14b. Significant changes in ALB occur over Eurasia. In contrast to the negative correlation between v' and T' in the SH *(Trenberth 1991)*, v' and T' are positively correlated in the NH. In the SH, the simulated eddies in CTR are weaker during DJF than in the observations and the SH anomalies between ALB and CTR are neglectable. Comparing the $\overline{v'T'}$ resulting from the CO2 and ORB simulations with CTR (Fig. 3.14c,d), it can be concluded that the reduced CO_2 and the changes in the orbital parameters do not modify the eddies substantially. However, a slightly intensification of $\overline{v'T'}$ is found over northwestern Canada and over the North Atlantic in ORB (Fig. 3.14d).

The eddy heat flux anomalies between TOPO and CTR are displayed in Figure 3.14e. The northward heat flux resulting from glacial changes in topography exhibits a reduction of eddy activity over the storm track region whereas an intensification is found over central Asia and northern North Atlantic. The weaker eddy activity simulated over the North Atlantic, classical storm track region, is not in agreement with the strong meridional thermal gradient and with the σ_{BI} anomalies in TOPO

[3] Storm track is often defined by the regions of maximum variance of geopotential height z in the middle and upper troposphere arising from disturbances with periods less than about one week.

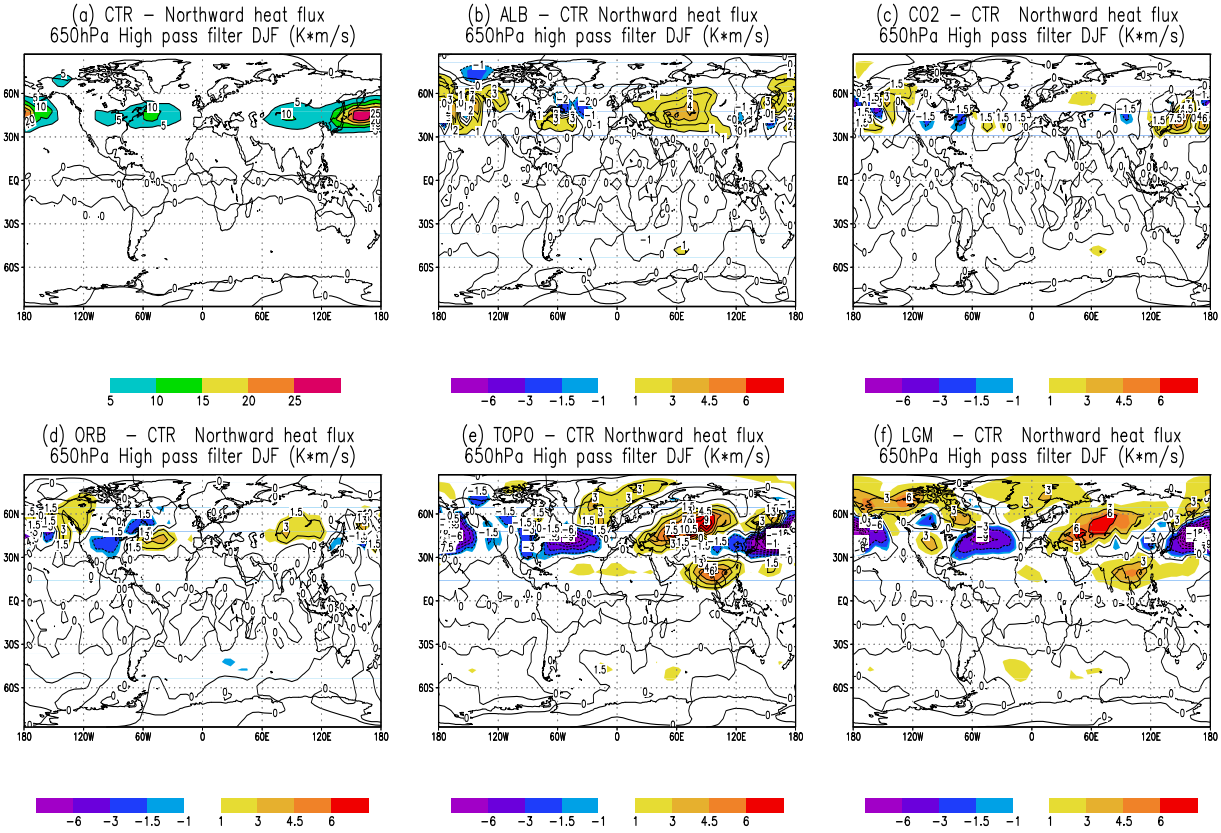

Fig. 3.14: *Northward eddy heat flux in DJF [$K \times ms^{-1}$] in CTR (a) and the sensitivity experiments anomalies. ALB-CTR (b) CO2-CTR (c) ORB-CTR (d) TOPO-CTR (e) LGM-CTR (f).*

(Fig. 3.12e). However, the dipolar structure in the North Atlantic corresponds to a northward shift of the storm track. Over the North Pacific, σ_{BI} and $\overline{v'T'}$ are well correlated and they are in agreement with the reduced meridional thermal gradient as a consequence of the warmer North Pacific (retreat of sea-ice margin). Over central Asia, the enhanced $\overline{v'T'}$ is a result of increased horizontally velocity shear downstream of the Eurasian ice-sheet, in response to topographic stationary wave forcing. It does not show up in the Eady growth rate which just captures the vertical wind shear and thus baroclinic instability. The northward shift of the North Atlantic storm track in TOPO has a significant effect on the snow accumulation in high-latitudes. In reality, a northward shift of the storm tracks may have influenced the ice sheet mass budget over eastern Greenland and Scandinavia, as discussed by *Kapsner et al. (1995).*

The LGM simulation reproduces the main features described for the TOPO simulation (Figure 3.14f), although, the other boundary conditions have significant contributions over the Canadian Islands, Nordic Seas and Alaska. The LGM also exhibits a small-scale increase in the storm track activity over central North America that has not been found in the isolated experiments. The eddy activity also strengthens from

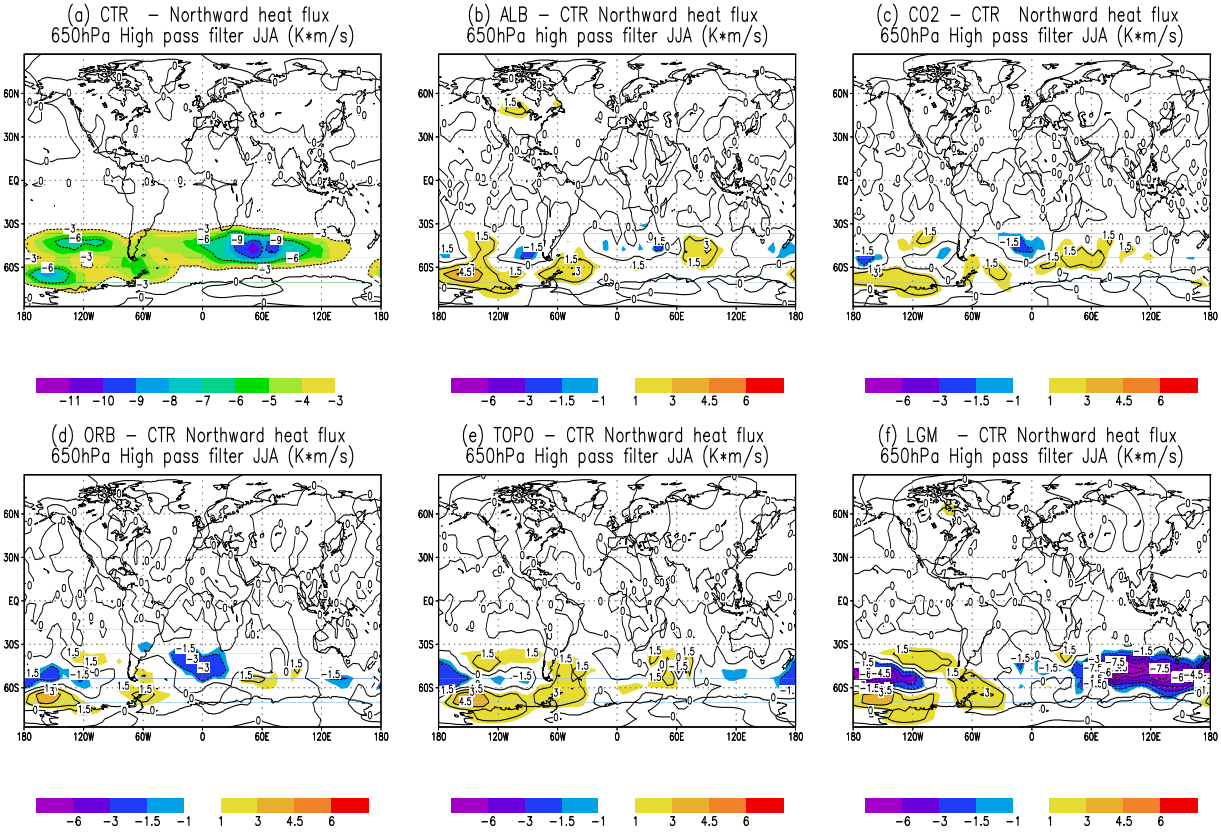

Fig. 3.15: *Northward eddy heat flux in JJA [$K \times ms^{-1}$] in CTR (a) and the sensitivity experiments anomalies. ALB-CTR (b) CO2-CTR (c) ORB-CTR (d) TOPO-CTR (e) LGM-CTR (f).*

southeastern Asia to the northwestern Pacific and might be a result of the downstream intensification of the low triggered by the topographic changes in Tibet.

During JJA, the simulated northward eddy heat flux in CTR is reduced in NH as compared to DJF. The strongest eddy activity is found in the SH with maximum southward heat transport in the ACC area between 20° and 120°E (Fig. 3.13a. Over some parts of the southeastern Pacific, a weakening of the southward heat transport can be found in all sensitivity experiments (Fig. 3.15). This weaker southward heat flux is in agreement with the reduced westerly flow (Fig. 4.1).

Although, the sensitivity experiments show only weak changes in $\overline{v'T'}$ during JJA, the LGM displays a pronounced strengthening in the southward heat flux around 45°S from the Indian to western Pacific Ocean (Figure 3.15f). This pattern seems to be a result of nonlinearities associated with the interaction among the different forcing terms.

The zonally averaged transient eddy heat flux is shown in Figure 3.16a for DJF. In the SH, only slight changes are simulated during DJF. Changes in the NH are stronger, and the reduced $\overline{v'T'}$ simulated by LGM is well captured by the TOPO experiment.

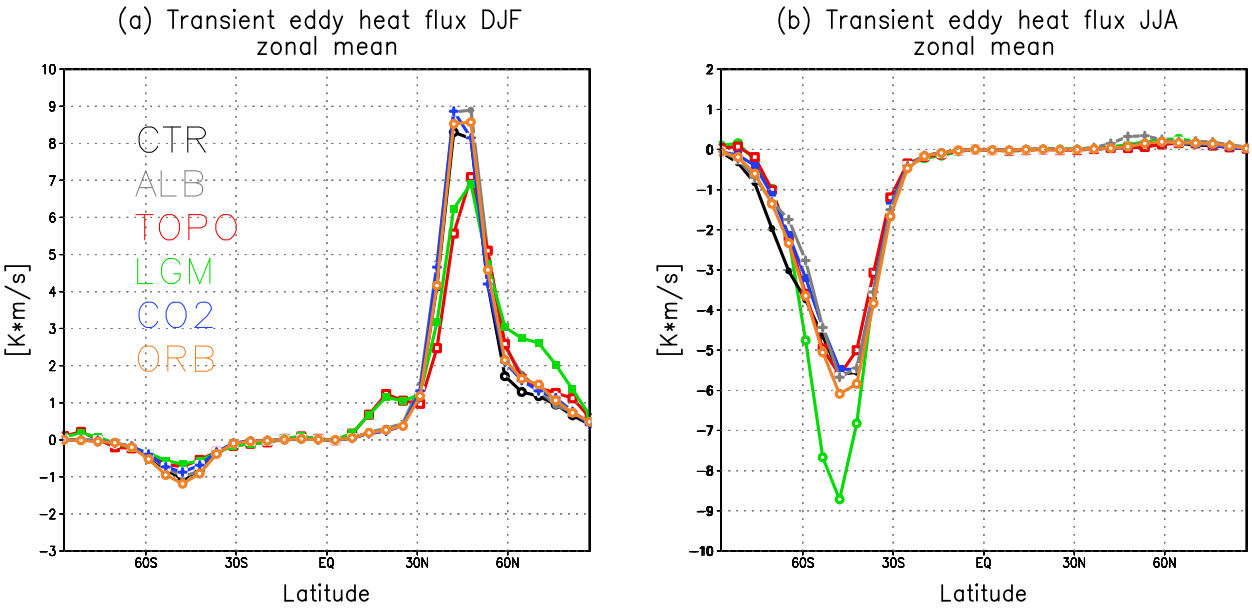

Fig. 3.16: *Zonally averaged northward eddy heat flux in CTR and the sensitivity experiments in DJF (a) and JJA (b) [$K \times ms^{-1}$].*

The effect of the topography is most evident in the reduction of $\overline{v'T'}$ around 45°N. The LGM exhibits an increase in the $\overline{v'T'}$ north of 60°N as a result of enhanced baroclinicity in this area. In JJA, the sensitivity experiments show almost the same zonal mean structure, except for the LGM. At the latitude belt of about 45°S, the southward transient eddy heat flux increases by more than 30% (Figure 3.16b).

Comparison between the eddy heat flux and Eady growth rate changes shows a good pattern correspondence between the low-level transient eddies and areas of reduced baroclinicity, in particular in the Pacific storm track region. The meridional heat flux due to transient eddies is one of the primary fluxes associated with baroclinic instability. *Trenberth (1991)* argued that the downgradient heat fluxes generate eddy available potential energy which is converted into eddy kinetic energy through the vertical velocity. In addition to the transient baroclinic eddies contribution, the Lorenz energy cycle shows that forced stationary topographic waves and free Rossby waves may also contribute substantially to the poleward heat flux (*Lorenz 1967, 1960).*

Another useful storm track diagnostic is the eddy kinetic energy (EKE) due to transient waves. The simulated present day EKE maxima are well placed in the ECBilt-Clio CTR simulation (Fig. 3.17a), in comparison with the ECMWF analysis shown by *Hoskins et al. (1989).* However, the EKE amplitude depends strongly on the model horizontal resolution *(Dong and Valdes 2000; Stendel and Roeckner 1998).* Since the simulations here are performed using a T21 atmospheric model, the amount of transient kinetic energy (wave activity) is very small. The EKE amplitude at 200hPa is underestimated by a factor of 2 over the eastern hemisphere and by about one third

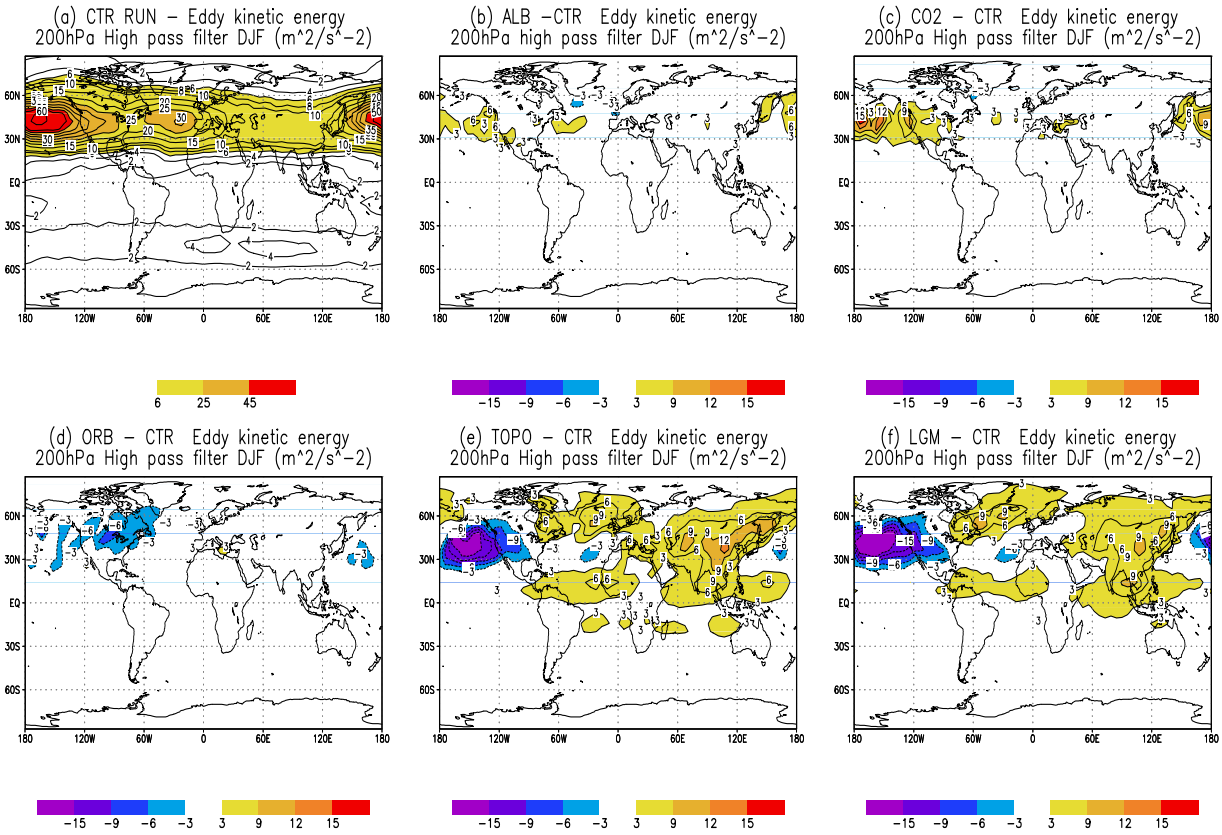

Fig. 3.17: *Time averaged transient EKE in DJF [$m^2 s^{-2}$] in CTR (a) and the sensitivity experiments anomalies. ALB-CTR (b) CO2-CTR (c) ORB-CTR (d) TOPO-CTR (e) LGM-CTR (f).*

over the North Atlantic as compared to observations. Larger values of EKE are an indication that more intense high and low pressure systems travel along the typical paths in midlatitudes. Due to the low resolution adopted in the experiments the amplitude between the high and the low pressure system is reduced, thereby showing a weakening of the upper level storm track activity. *Dong and Valdes (2000)* also attributed the weakening of the simulated storm track activity in a low-resolution model to the sluggish surface temperature gradients along the sea-ice edge. In spite of the regional differences with observations, the model can reproduce the observed EKE in the zonal average quite well (see Figure 7.22 of *Peixoto and Oort 1992).*

As addressed by *Chang et al. (2002)*, the storm track EKE attains its maximum somewhat downstream of the maximum of $\overline{v'T'}$. This is illustrated in Figures 3.14a and 3.17a. The anomalies between ALB and CTR during DJF exhibits a slight 10% increase in the EKE of Atlantic and Pacific storm tracks (Fig. 3.17b).

In comparison to CTR, the EKE resulting from reduced atmospheric CO_2 concentration shows an increase in the eddy activity over the central Pacific as well as a downstream intensification (Figure 3.17c). This enhancement is mainly a result of the

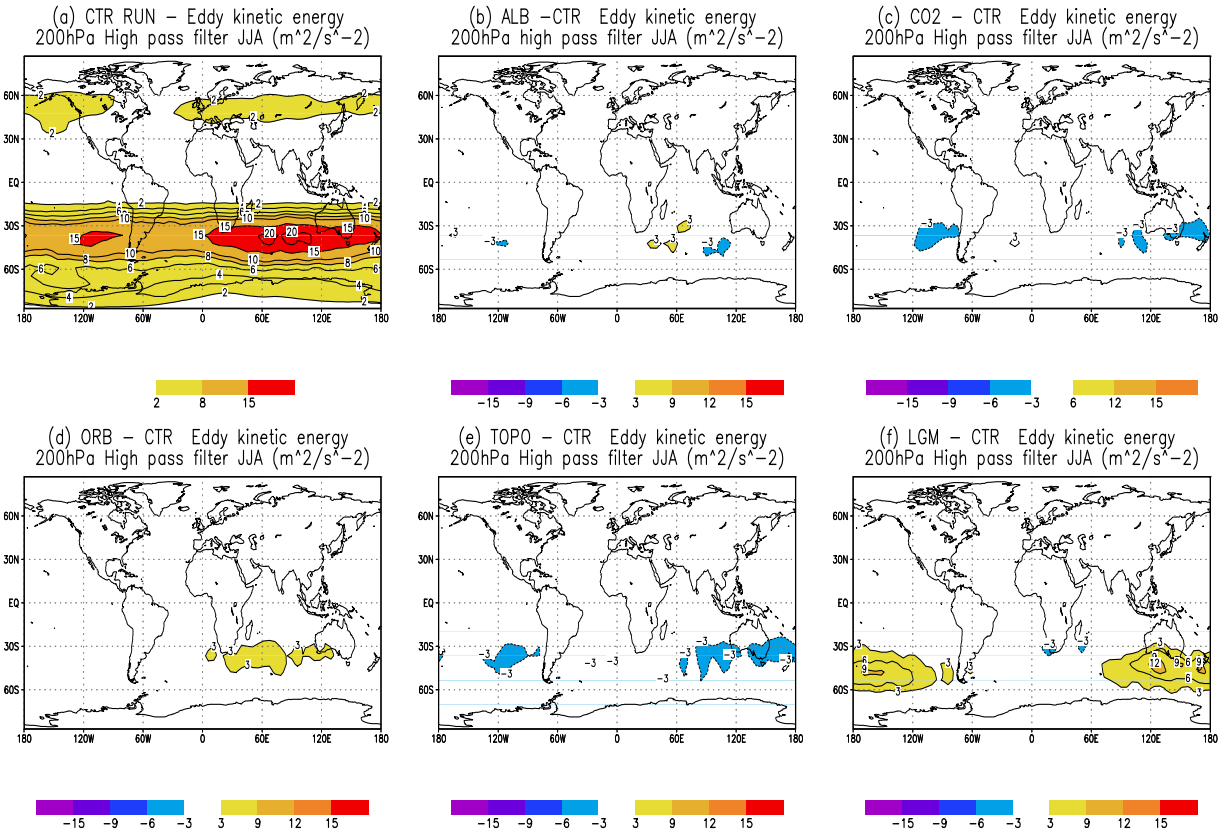

Fig. 3.18: *Time averaged transient EKE in JJA $[m^2 s^{-2}]$ in CTR (a) and the sensitivity experiments anomalies. ALB-CTR (b) CO2-CTR (c) ORB-CTR (d) TOPO-CTR (e) LGM-CTR (f).*

strengthening in $\overline{u'^2}$ component, rather than $\overline{v'^2}$. The stronger Pacific storm track simulated by CO2 has not been anticipated since previous experiments carried out under doubled present- day atmospheric CO_2 concentration reveal also an increase in eddy activity *(e.g. Hall et al. 1994)*. The anomalies in the SH are weaker than in the NH and in general show a decrease in the EKE maxima. The EKE response to the changes in the Earth's orbital parameters (Fig 3.17d) reveals a decrease over large parts of the North American continent.

The presence of the Laurentide and Fennoscandian ice sheets in TOPO leads to an increase in EKE in the eastern hemisphere (Fig. 3.17e). The storm track maxima increase by more than 60% over eastern Asia and by almost 40% over the northern North Atlantic. The enhanced topographically forced eddy activity has already been found in the low-level northward eddy heat flux. The topographic changes also enhance the EKE over Europe and the Mediterranean region. This is probably a result of the interaction between the Atlantic storm track and the stationary low pressure system over eastern Europe. Nevertheless, further work is necessary to better understand the main dynamical features responsible for the enhancement of the transient eddies over

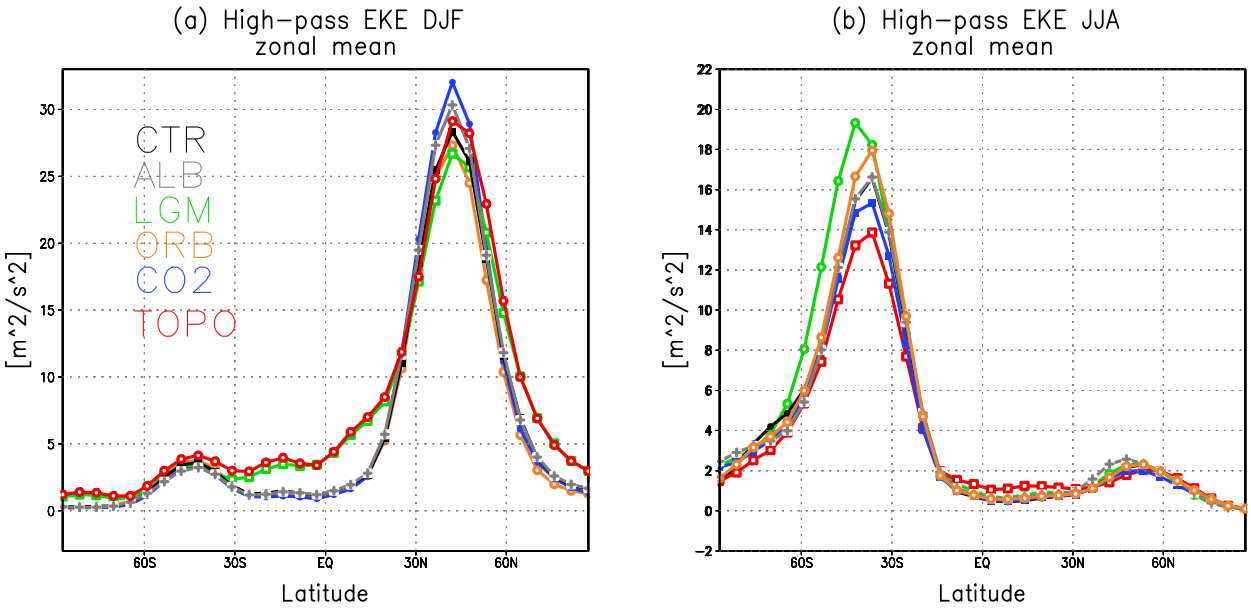

Fig. 3.19: *Zonally averaged transient EKE in CTR and the sensitivity experiments in DJF (a) and JJA (b) [$m^2 s^{-2}$].*

these areas. The DJF anomalies between the LGM and CTR are shown in Figure 3.17f. The LGM reproduces the main features simulated in TOPO, although some differences can be readily noted. For instance, the North Atlantic storm track is stronger and extended further northward in LGM as compared to TOPO. Furthermore, the interaction among the individual boundary condition changes weakens the EKE over Europe and eastern Asia in comparison to TOPO. Over the North Pacific the EKE response to the topographic forcing is opposite to the response simulated by CO2, as depicted in Fig. 3.17c,e. The CO_2 forcing tends to intensifies the EKE, whereas topographic forcing tends to suppresses the EKE. However, it is clearly seen that the later plays the leading role in the LGM climate.

Figure 3.18 shows the EKE anomalies for the JJA period. In CTR (Fig. 3.18a), the NH storm track activity is extremely reduced as compared to DJF. The storm track still exists but it is too weak and almost disappears over the North Atlantic. The largest amplitudes are simulated around 40°S. In the NH, the JJA EKE does not change substantially in any of the sensitivity experiments compared to CTR. In the SH, anomalies are mainly evident over the southern Pacific/Indian Ocean. Interestingly, none of the ALB, CO2, ORB or TOPO runs is able to capture the response simulated by the LGM with all the different forcing included. This nonlinearity is consistent with the nonlinear behaviour of $\overline{v'T'}$.

The zonally averaged EKE is displayed in Figure 3.19. The stronger DJF Pacific storm track in the CO2 simulation is well captured (Fig. 3.19a). The CO2 run simulates the largest eddy activity among the simulations of about 45°N. In the tropics, however,

the topography effect is responsible for an enhancement of EKE simulated by LGM. In the SH extra-tropics, the sensitivity runs display almost the same structure. It should be mentioned that during summer the model simulates very weak transient eddies in the NH (Fig. 3.19b). In the SH, the LGM (TOPO) displays the largest (smallest) EKE values. The changes of EKE resulting from modified Earth's orbital parameters, seem to play an important role in the amplification of LGM southern hemisphere storm track anomalies.

3.4.2 Eddy-Mean Flow Interactions

As shown in many studies *(e.g. Jeffreys 1926)*, the transient eddies may feed back to the zonal and time-mean flow circulation. The momentum budget in the atmosphere requires a two-sided interaction between eddies and the mean circulation. It can be shown that the zonal mean circulation is decelerated/accelerated by the meridional convergence/divergence of the zonally integrated eddy momentum fluxes ($\overline{u'v'}$). The meridional and zonal wind components of transient eddies are highly correlated which leads to a net meridional transport of zonal momentum in the atmosphere. In turn, a modified mean circulation has the potential to modify the eddy characteristics both in a barotropic and baroclinic framework. Here, an attempt is made to quantify this interaction for the sensitivity experiments described above. The analysis focuses on the ALB, TOPO and LGM experiments during DJF since the changes in CO2 and ORB seem to play a secondary role in the NH.

Figure 3.20 depicts the zonally integrated eddy momentum flux of the high-pass filtered transient eddies and its convergence in the CTR, as well as the TOPO and LGM anomalies with respect to CTR.

As a consequence of topographic forcing, a large negative gradient of the eddy momentum flux is simulated near 30°N. This leads to an intensification of the upper-level westerlies at about 30°N following the relation $\dot{u} = \frac{\partial}{\partial y} < \overline{u'v'} >$, thereby opposing the total zonal mean wind reduction (see Fig. 4.6b). From the experiments, it can be shown that the zonally integrated eddy momentum flux anomaly of the stationary eddies waves is about 2 times larger *(see Timmermann et al. 2004)* than that of the transient waves and of opposite sign. The stationary wave momentum flux convergence leads to a weakening of the zonal mean jets, in accordance with the Figure 4.6b,c.

In order to obtain more regional information on the eddy-mean flow interactions further diagnostic methods are used. *Hoskins et al. (1983)* proposed a diagnostic framework to interpret the relationship between eddies and the mean flow in terms of the $\vec{E}$ vector [$\vec{E} = (\overline{v'^2 - u'^2}, \overline{-u'v'})$]. It quantifies the shape, propagation and mean-flow interaction of transient eddies. Furthermore, it also measures the propagation of meridionally elongated eddies relative to the westerly mean flow *(Hall et al. 1994)*. In regions where $\vec{E}$ is divergent (convergent) there is a forcing of the mean horizontal circulation consistent with a tendency of the eddies to increase (decrease) the westerly mean flow. Figure 3.21 shows the 200hPa high-pass $\vec{E}$ superimposed on the time-mean 200 hPa zonal wind. The $\vec{E}$ pattern in CTR is predominantly zonal with maxima downstream of the storm tracks. The $\vec{E}$ vector over the North Atlantic shows a divergence downstream of the jet maximum and this pattern is maintained until it turns

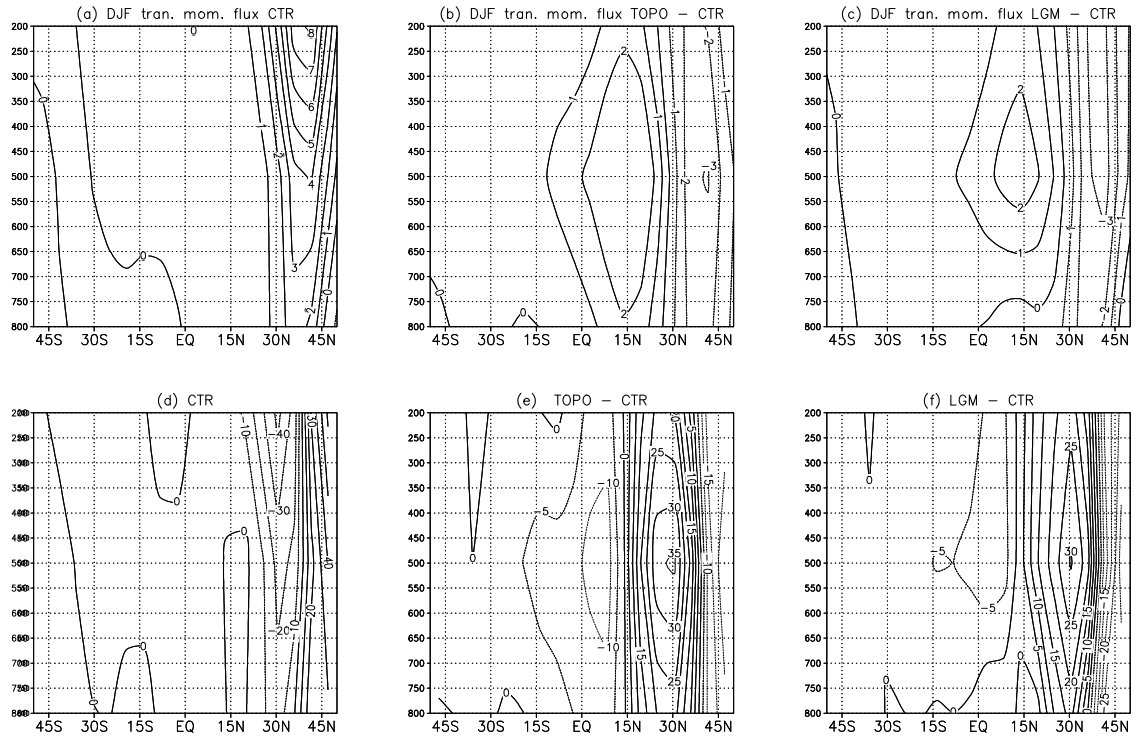

Fig. 3.20: *DJF zonal mean of transient eddy momentum flux $[m^2 s^{-2}]$ in CTR (a) and the anomalies between TOPO-CTR (b), LGM-CTR (c), and the transient eddy momentum flux convergence (negative divergence) $[10^{-6} \times m^2 s^{-2}]$ in CTR (d) and the anomalies between TOPO-CTR (e) LGM-CTR (f).*

to converge as it reaches central Europe. Over the north Pacific the $\vec{E}$ vector diverges from the middle to the end of the storm track. In LGM (Fig. 3.21b), the $\vec{E}$ vector is very similar to that of the CTR, but it has a weaker magnitude over the North Pacific. However, the LGM exhibits stronger $\vec{E}$ over the northern North Atlantic. This is further illustrated by the difference plot of $\vec{E}$ between LGM and CTR (Fig. 3.21c). Over the North Atlantic the LGM exhibits stronger divergence of $\vec{E}$ and a strengthening on the northward flank over the Nordic Seas, thereby, favouring the intensification of the jet stream over the northern North Atlantic. According to the relationship between eddy momentum flux divergence and the zonal mean flow acceleration, the northward anomalies of $\vec{E}$ over the North America are associated with a deceleration of the jet stream and acceleration south of it. The slowing down of the zonal mean circulation originates from several contributions. The topographic barrier of the Laurentide ice-sheet creates an upstream blocking situation in the North Pacific which slows down the westerlies. Furthermore, the weaker meridional thermal gradient in eastern Pacific also leads to changes in the vertical wind shear, slowing down upper level westerlies. In turn, this leads to a reduced meridional eddy momentum transport and a weaker zonal component of the E-vector in the northwestern Pacific (Fig. 3.21c), providing

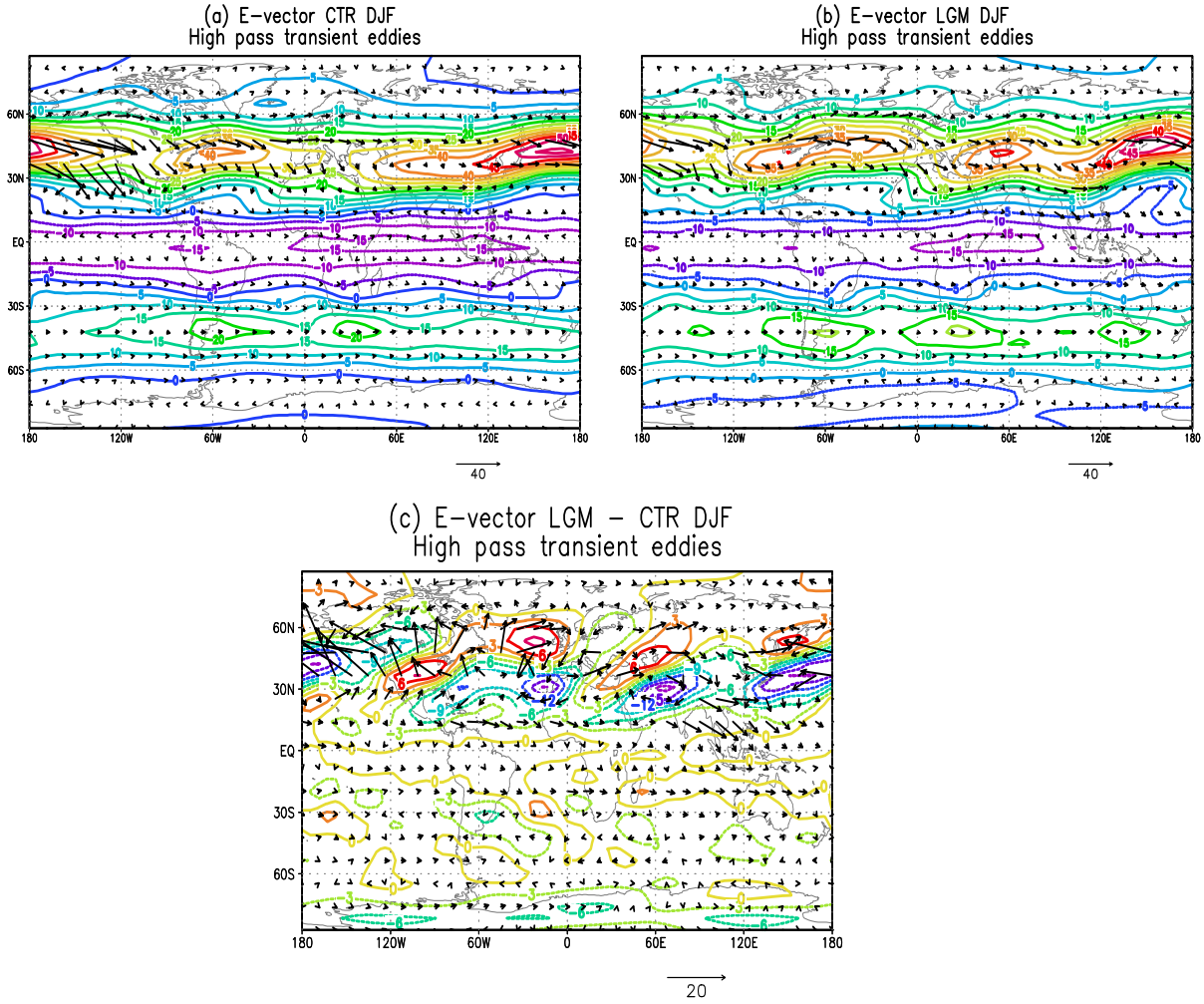

Fig. 3.21: *DJF zonal wind at 200hPa (ms^{-1}) with 200hPa high-pass $\vec{E}$ (m^2s^{-2}) in DJF. For (a) CTR, (b) LGM and (c) anomalies LGM-CTR.*

another break for the upper level westerlies.

One disadvantage of the 2-dimensional $\vec{E}$ vector concept originates from the fact that it captures both changes of the baroclinic and the barotropic eddy mean-flow interactions. Furthermore, its local interpretation may be problematic. In order to disentangle these two contributions more objectively and in detail, the transient barotropic conversion *(Wallace and Lau 1985)* and baroclinic production rates *(see Merkel 2002 for details)* are diagnosed. The barotropic conversion rate can be computed from the scalar product of the 2-dimensional $\vec{E}$ and the gradient of the time-averaged zonal velocity $(\vec{E} \cdot \nabla \overline{u})$. To obtain the baroclinic energy production K_{bc} the relation $K_{bc} = f(u'v'_a - v'u'_a)$ is used, where (u_a, v_a) represents the 2-dimensional ageostrophic velocity and f the Coriolis parameter. Negative values of these conversion rates indicate a mean flow acceleration and a reduction of eddy kinetic energy.

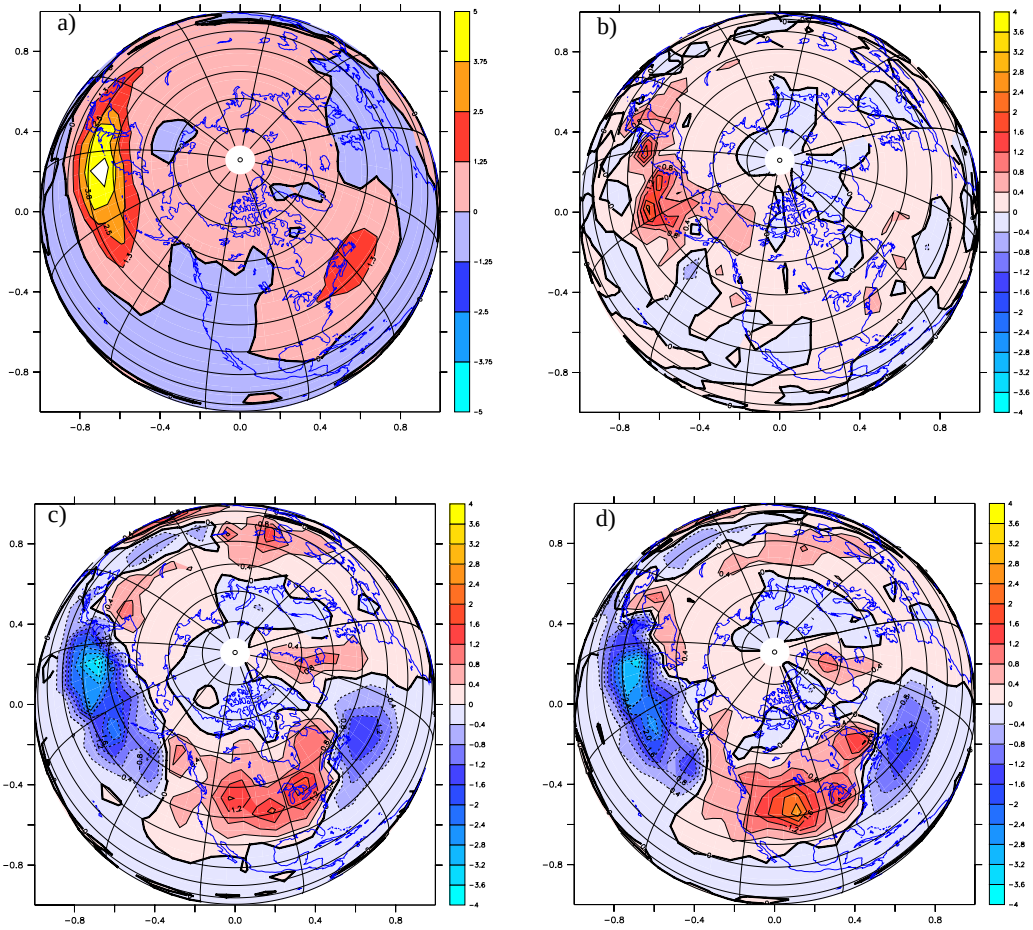

Fig. 3.22: *Time averaged high-pass eddy baroclinic production rates at 500 hPa in DJF [$10^{-4}m^2s^{-3}$] in CTR (a), and the anomalies between ALB-CTR (b), TOPO-CTR (c) LGM-CTR (d).*

Figure 3.22 shows the baroclinic production rate of transient eddy kinetic energy at 500 hPa. One observes a positive production in the regions of highest baroclinicity, resulting in a mean flow deceleration, in particular in the North Pacific jet entrance region (Fig. 3.22a). The North Atlantic baroclinic production of eddy kinetic energy is weaker than in the Pacific. The ALB simulation leads to an intensification of the storm track anomalies in the eastern and central north Pacific. These changes are also partially captured by the Eady growth rate (Fig. 3.12b). The baroclinic production rate in the LGM is mostly governed by the topographic effect. The TOPO simulation shows reduced baroclinic eddy production in the western north Pacific, thereby leading to an acceleration of the mean flow. Furthermore, an enhanced baroclinic eddy production rate can be observed over the ice caps, due to the enhanced baroclinicity in these regions.

As can be seen from Fig. 3.23a, barotropic conversion is positive in the jet entrance regions leading to a mean flow reduction. Further downstream barotropic eddies feed the mean flow, in accordance with the fact that the divergence of the $\vec{E}$ vector induces

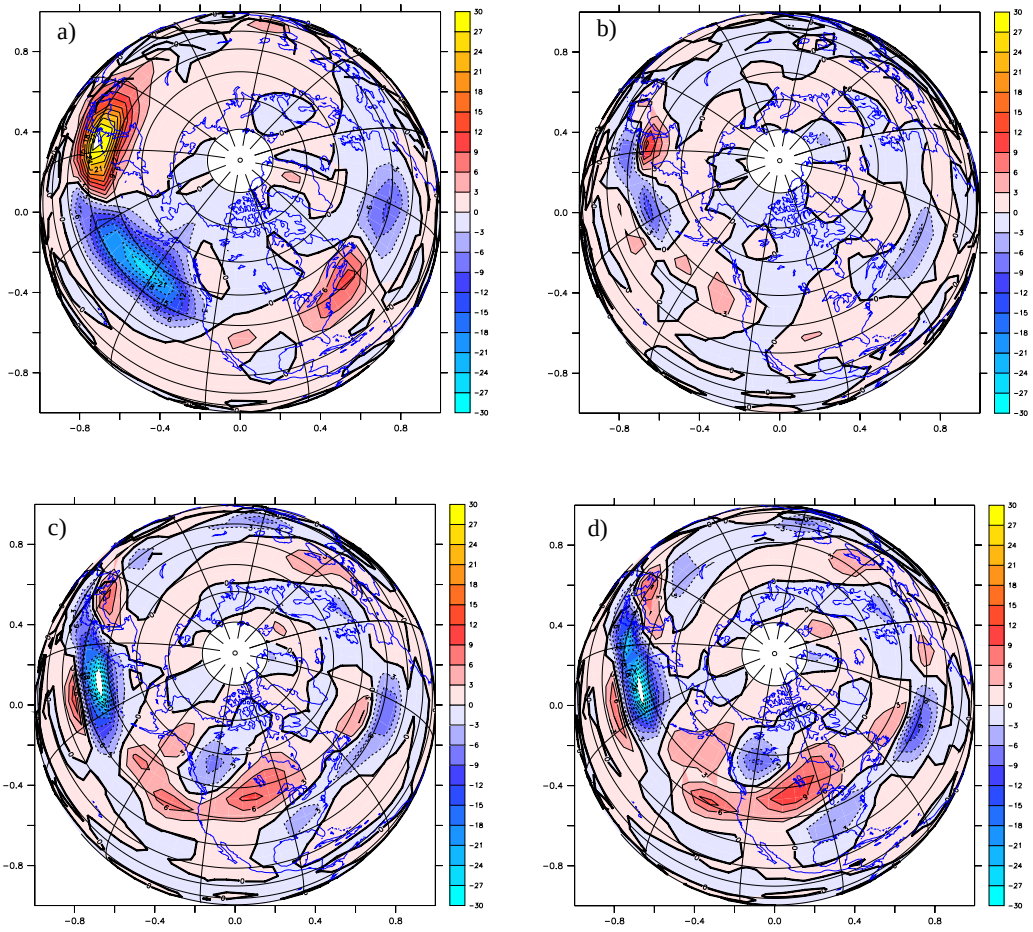

Fig. 3.23: *Time averaged high-pass eddy barotropic conversion rates at 500 hPa in DJF [$10^{-4} m^2 s^{-3}$] in CTR (a), and the anomalies between ALB-CTR (b), TOPO-CTR (c) LGM-CTR (d).*

westerly flow acceleration. The barotropic energy conversion anomalies in ALB, TOPO and LGM (Fig. 3.23), show an increase over northeastern Pacific and over the Laurentide ice sheet, thereby decreasing the mean flow in that area, whereas a mean strong flow acceleration (negative barotropic conversion rates) can be observed in the northwestern Pacific. In the North Atlantic region the barotropic changes have a small-scale structure, with a slight tendency for an intensification of barotropic energy conversion in the northern North Atlantic.

Baroclinic and barotropic processes modulate the storm track activity in the North Pacific, Laurentide and North Atlantic area in a coherent way which is consistent with the simulated eddy-high pass kinetic energy (see Fig. 3.17). Both add to a mean flow weakening over the North Pacific. Due to the changes in baroclinicity and transient eddy activity in the LGM, one should expect significant changes in snowfall and precipitation. Figure 3.24 displays the snowfall anomalies for TOPO, ALB and LGM. It shows that the largest changes occur over places with high eddy activities. Changes in baroclinicity and the storm track characteristics are responsible for an

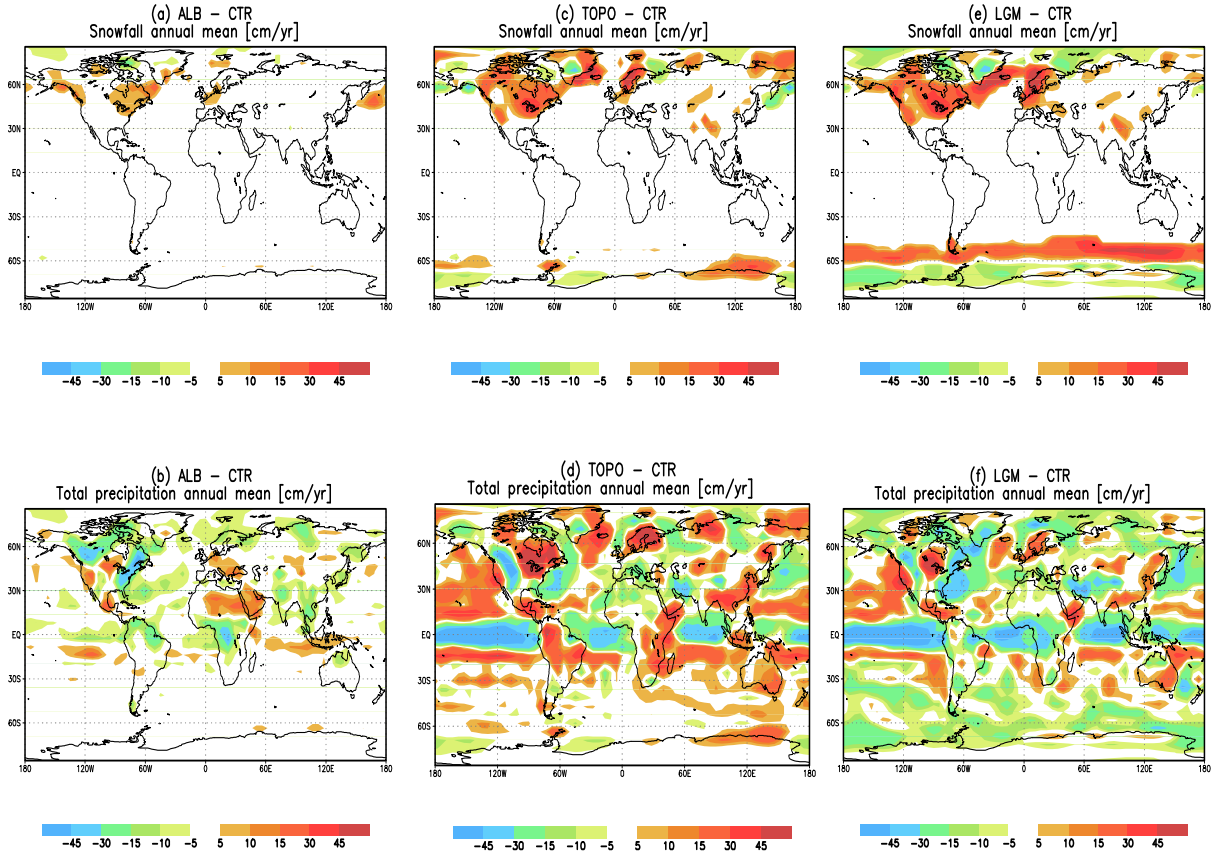

Fig. 3.24: *Snowfall and precipitation anomalies [cm/yr]. (a) and (b) ALB-CTR, (c) and (d) TOPO-CTR, (e) and (f) LGM-CTR.*

increase in snowfall by about 400m/1000years over northeast Canada, the GIN Seas and Scandinavia. During the *LGM* most of the snowfall anomalies in the NH are a result of the presence of the Laurentide and Fennoscandian ice sheets (Fig. 3.24c,e). The other glacial boundary conditions play only a secondary role. In the SH, a belt of increased snowfall is seen around 60°S which is consistent with the enhanced eddy activity and changes of the sea-ice margin in particular in JJA (see Figs. 3.15f, 3.18f). Glacial snowfall are not a direct consequence of the changes of a single boundary condition. Turning to the changes in precipitation (Figs. 3.24b,d,f), the LGM exhibits dryer conditions in most of the tropics and extra-tropics due to the decreased water content in the colder atmosphere associated with the surface cooling, as shown in Figure 3.6. In the eastern equatorial Pacific, the precipitation in the LGM is extremely reduced as a consequence of the permanent La Niña state. However, the precipitation increases over some tropical/subtropical areas which are characterised by positive SST anomalies, as highlighted in the northeast Pacific. The positive precipitation anomalies are also simulated over central North America and Scandinavia. Precipitation in the LGM is reduced along eastern North America and the western North Pacific as a result of the advection of cold and dry air from the eastern flank of the ice caps in the

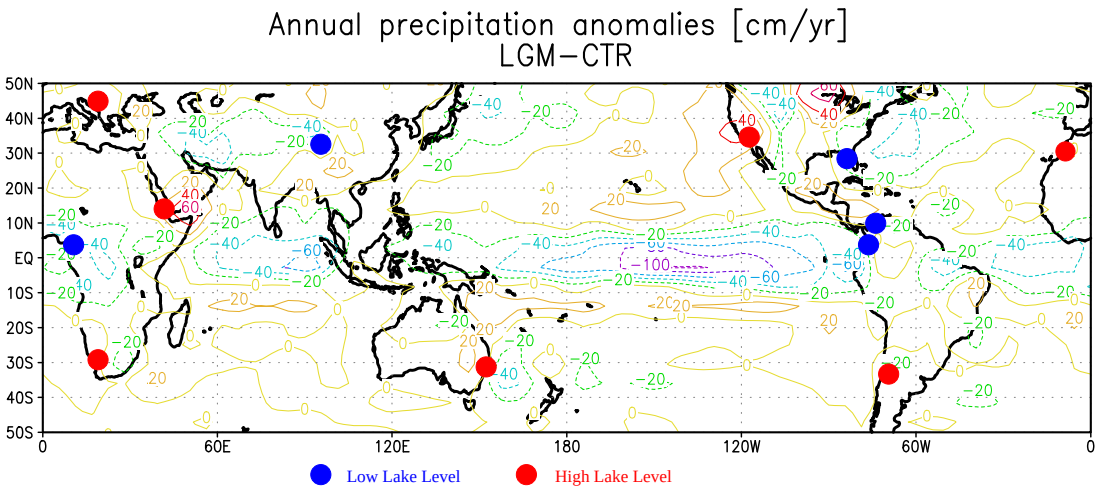

Fig. 3.25: *Simulated precipitation anomalies between the LGM and CTR [cm/yr] and reconstructed areas of enhanced and reduced precipitation from the lake level data of Kohfeld and Harrison (2000).*

LGM. This anomaly advection acts as a positive feedback to suppress the convection (Fig. 3.24). Despite the strong influence of topographic forcing on the precipitation, some differences can be noted between TOPO and LGM. For example, the increase in precipitation over northern South America and eastern Africa in the TOPO is not reproduced in the LGM. This dryer condition in the LGM has also been simulated by ALB as a result of deforestation - increased albedo (Fig. 3.24b).

Compared to paleoclimatic reconstructions from pollen records in Europe and western Siberia *(Peyron et al. 1998; Tarasov et al. 1999)*, the LGM overestimates the annual precipitation in western and central Europe, but it shows much better agreement with the proxies in western Siberia where the paleodata are quite reliable. Such discrepancies between the precipitation simulated by LGM and the paleoreconstructions have also been identified in other *LGM* simulations *(Shin et al. 2003; Wyputta et al. 2001)*. Compared to lake level anomalies *(Kohfeld and Harrison 2000; Street-Perrott and Harrison 1985)*, the simulated precipitation is in good agreement with the proxies, in particular over the north and equatorial Pacific, the eastern coast of North America and the subtropical Atlantic (Fig. 3.25). The simulation and the paleoreconstruction disagree over southern South America and northern Africa where the simulated precipitation is underestimated.

After considering the precipitation and snowfall anomalies separately the evaporation to precipitation ratios will be considered now as it is closely related to hydrology. According to *Peixoto and Oort (1992)* the zonal mean aridity index is defined as E/P (evaporation/precipitation). Table 3.3 shows this index for CTR and the sensitivity experiments. In general, the *LGM* experiments produce an excess of evaporation over precipitation in the tropical region, whereas a deficit of evaporation is found in the extra-tropics. Among the sensitivity experiments, TOPO shows the largest aridity index in the tropics as a result of lower SST and reduced precipitation associated with a weakening of the ITCZ. Furthermore, the convergence of humidity (not shown) in

the tropical belt is extremely reduced in the TOPO and LGM. Compared to CTR, it represents more arid conditions as displayed by the specific humidity anomalies (Fig. 3.6). The other boundary conditions have almost the same impact on the hydrological balance during the *LGM*. In mid and high latitudes the excess of precipitation is likely due to the precipitation anomalies over the North Pacific and North America (Fig. 3.25). Compared to CTR in the SH, the aridity index in the LGM is extremely reduced, probably as a result of decreased evaporation due to lower SST and weaker westerlies.

Sensitivity Exp.	30°S-30°N	30-90°N	30-90°S
CTR	1.17	0.88	0.82
TOPO	1.24	0.90	0.81
ALB	1.19	0.82	0.81
CO2	1.19	0.87	0.81
ORB	1.17	0.88	0.81
LGM	1.23	0.82	0.77

Tab. 3.3: *Aridity Index (E/P) for CTR and the LGM sensitivity experiments.*

3.5 Summary

The results here show that the presence of the LGM ice sheets and changes in land albedo play the most important role for the atmospheric circulation anomalies during the *LGM*. When averaged globally, the changes in albedo generate the largest radiative forcing and the strongest tendency of cooling as compared to the changes resulting from the other boundary conditions. In some areas, TOPO and ALB produce different climate responses. For example, TOPO shows a warming over eastern Asia and the North Pacific, while ALB generates a cooling in these areas. Although the modified orbital parameters and reduced atmospheric CO_2 concentration favour also a reduction of surface air temperature, their influence on the LGM is more clearly manifested in the SH. The positive southern hemisphere t2m anomalies in TOPO (1°C) are replaced by a strong cooling of up to 5°C in the LGM. This cooling results from the changes in the orbital parameters and the CO_2 concentration since the changes triggered by modified land albedo are too weak. In addition, as a result of the lower temperatures the dryer atmosphere also plays an important role to enforce the overall global cooling due to the weaker greenhouse capacity.

The snowfall anomalies between LGM and CTR can be attributed to the enhancement and northward migration of the North Atlantic storm track. They are characterised by increased snowfall in the LGM in North America, the GIN and Labrador Seas. Furthermore, there is a reduction in precipitation on the eastern coast of North America and over western Pacific. An interesting feature is simulated in the SH where the strengthening of the storm track over ACC area of the Indian Ocean sector is accompanied by an increase of snowfall. The simulated LGM temperature and precipitation

are in good agreement with some paleoreconstructions.

Changes of the stationary wave patterns during DJF are an important climate component during the LGM. All boundary conditions seem to contribute to the generation of the stationary low pressure system over Scandinavia and the Hudson Bay in the LGM. The ice sheet topography enhances the trough in these areas as well as over the North Atlantic and the Nordic Seas. The topographic effect of the ice sheets is also manifested in the high pressure anomaly over the North Pacific. Furthermore, it was found that the JJA stationary wave pattern over North America is strongly affected by the land albedo and topography. Changes in the orbital parameters and atmospheric CO_2 concentration produce relatively weak glacial stationary wave anomalies. The series of experiment carried out with different topographic anomalies showed that the amplitude of wave train and the low pressure system over North America are controlled by the height of the ice sheet, although the relationship is not linear. The analyses in σ_{BI} (baroclinic instability) revealed that the glacial topographic changes intensify baroclinic instability over North America. Over Scandinavia, however, the reduction in the vertical wind shear due to the presence of the Fennoscandian ice sheet decreases σ_{BI}. During JJA, the influence of the topography forcing is much weaker competing with the impact of glacial albedo changes. The similarity between the atmospheric changes simulated by TOPO and LGM also confirms that the presence of the ice sheet is the main responsible mechanism for the modified eddy activity in the LGM. Interestingly, the largest storm track changes in the LGM experiment occurs in the Indian Ocean sector of the ACC during austral winter and without having a direct correspondence with any of the sensitivity experiment anomaly. The correspondence between the anomalies in storm track intensity and the anomalies of the Eady growth rate lead to the conclusion that changes in the transient eddy activity are mostly generated by changes in the baroclinic conditions further upstream. Furthermore, calculations of the $\vec{E}$ vector show that the interaction between the eddies and the mean flow is most pronounced over the North Atlantic where the glacial stronger storm track enhances the mean westerlies.

An investigation of the local eddy-mean flow interactions using the barotropic conversion and baroclinic production rates gives a more complex picture: Changes of the baroclinic production rates in LGM are dominated by the topographically induced anomalies. A weakening of baroclinic eddy production is simulated over the northwestern Pacific. Furthermore, an intensification and northward shift of the eddy kinetic energy production region over the North Atlantic was found. These changes correspond to similar anomalies of the diagnosed transient eddy kinetic energy, the eddy heat transport and the Eady growth rate. However, the divergence anomalies of the 2-dimensional $\vec{E}$ vector do not always match the anomalies of the barotropic and baroclinic conversion rates. Changes of the barotropic eddy energy conversion are most pronounced in the western North Pacific. A large negative anomaly is associated with reduced barotropic eddy kinetic energy conversion and an overall acceleration of the westerly mean flow. Positive barotropic conversion and baroclinic production rates over the Laurentide ice sheets and the far eastern North Pacific have the tendency to decelerate the westerly mean flow. Thereby, establishing an interaction between stationary and transient wave activity.

4. OCEANIC CHANGES DURING THE LAST GLACIAL MAXIMUM

The way to succeed is to keep one's courage and patience, and to work on energically.

Vincent van Gogh

4.1 Introduction

CLIMAPs planktonic-foraminifera-based sea surface temperature (SST) reconstructions (*CLIMAP 81)* for the LGM indicate that the glacial subtropical/mid-latitudinal North Pacific was probably warmer than today. This finding is, however, not consistent with SST reconstructions which are based on other marine *(Lee and Slowey 1999)* and terrestrial records from the vicinity of the Hawaiian islands (*Rind and Peteet 1995; Porter 1979).* An ongoing debate (see e.g. *Crowley 2000; Kerr 1995*) has not solved this discrepancy. Some scientists (*Lee and Slowey 1999)* have argued that possibly the low-sedimentation records from the CLIMAP compilation are biased towards warm temperatures due to bioturbation effects. This explanation is plausible but not proven. Recent coupled atmosphere-ocean general circulation model simulations (*Shin et al. 2003; Kim et al. 2003; Bush and Philander 1998; Kitoh et al. 2001)* of the LGM show also a disagreement in simulated North Pacific temperatures. While *Kitoh et al. (2001)* simulate a warming of the subtropical Pacific, very much like in the CLIMAP record, *Shin et al. (2003), Kim et al. (2003)* and *Bush and Philander (1998)* simulate a homogenous North Pacific cooling for the LGM. Neither the modeling nor the reconstruction studies have converged to a consensus yet. It is very surprising that despite this controversial scientific debate, the physical origin of a potential North Pacific warming has not yet been studied in great detail, to our knowledge.

Differences also exists between simulated and reconstructed ocean circulation anomalies. For instance, *Weaver et al. (1998)* argued that the ocean circulation in their model did not contribute to the tropical cooling. However, it has been reconstructed based on planktonic foraminifera a steeper tilt of the thermocline during glacial times in the tropical Pacific, with isotherms shoaling more in the east and deepening more in the west *(Andreasen and Ravelo 1997).* As discussed by *Bush and Philander (1999)* these changes are accompanied by an enhanced easterly trade winds over the Pacific and would be consistent with an enhanced Walker circulation during the *LGM (Molina-Cruz 1997; Sarnthein et al. 1981).* Therefore, in addition to thermodynamical coupling, dynamical coupling between the atmosphere and ocean plays a fundamental role in determining the *LGM* climate, as discussed by *Timmermann et al. (2004).* This conclusion supports the importance of using a global coupled atmosphere-ocean model

to simulate climate feedbacks realistically, in particular under very different boundary conditions like those inferred for the glacial period. In this chapter is investigated the changes of the oceanic circulation (wind-driven and thermohaline parts) for different glacial boundary conditions.

4.2 The Wind-driven Circulation and Sea Surface Temperature

A pre-requisite to understand changes of the wind-driven oceanic circulation is the analyses of the simulated wind stress anomaly field. Here analyses of the wind-driven circulation and SST are divided into 2 parts: First, the changes in the Atlantic basin are discussed; thereafter changes in the Pacific Ocean are analysed.

The simulated wind stress for CTR and the anomalies for the different sensitivity experiments are shown in Figure 4.1. Compared to COADS observations the wind stress strength in CTR is simulated quite realistically, though, the modeled maximum is placed almost 10° northward in the Kuroshio and Gulf Stream areas (Fig. 4.1a). In the CTR climate this misrepresentation is responsible, partially, for higher northwestern Atlantic and northwestern Pacific temperatures as a result of the northward displacement extension of the Gulf Stream and Kuroshio Current.

Compared to CTR, ALB, CO2 and ORB (Fig. 4.1b,c,d) are associated with an enhancement of the westerlies over the North Atlantic around 45-60°N, that results in a southward Ekman transport of cold water in the oceanic surface layer. Moreover, there is also an intensification of the wind stress over the west coast of Europe and northwestern Africa (Fig. 4.1b,c,d). This anomalous wind stress pattern (resembling a positive North Atlantic Oscillation pattern) favours the appearance of lower SST due to its associated offshore water transport and subsequently enhanced upwelling. The TOPO and LGM anomaly (Fig. 4.1e,f) patterns differ to the previous experiments. TOPO, simulates a northward anomaly in the North Atlantic as a result of low surface pressure over Greenland and a high pressure over western Europe (Fig. 3.7e,f).

The changes in LGM (Fig. 4.1f), are very similar to those depicted by the TOPO except for the extra-tropical Atlantic, where the northward wind stress anomaly simulated by TOPO is superposed by a northeastward in the LGM simulation. Furthermore, Figure 4.1f shows an enhancement of the wind stress around 60°N, which can be attributed to the strong meridional thermal gradient linked to a southward displacement of the sea-ice edge. In contrast to the weak wind stress changes in the North Pacific in ALB, CO2 and ORB, TOPO and LGM exhibit a strong reduction of the wind stress as a result of a blocking situation imposed by the Laurentide ice sheet (Fig. 4.1e,f). In the tropical regions stronger trade winds are found in all experiments. In the SH, changes between the CTR run and the *LGM* experiments show an enhanced tropical/subtropical easterlies.

As a result of the simulated shape and magnitude of the wind stress, the model can simulate quite well the magnitude of the Sverdrup transport estimated from observed wind stress data *(Hellerman and Rosenstein 1983)*, though, the front that separates the subtropical and the polar gyre is positioned too far northward due to the coarse

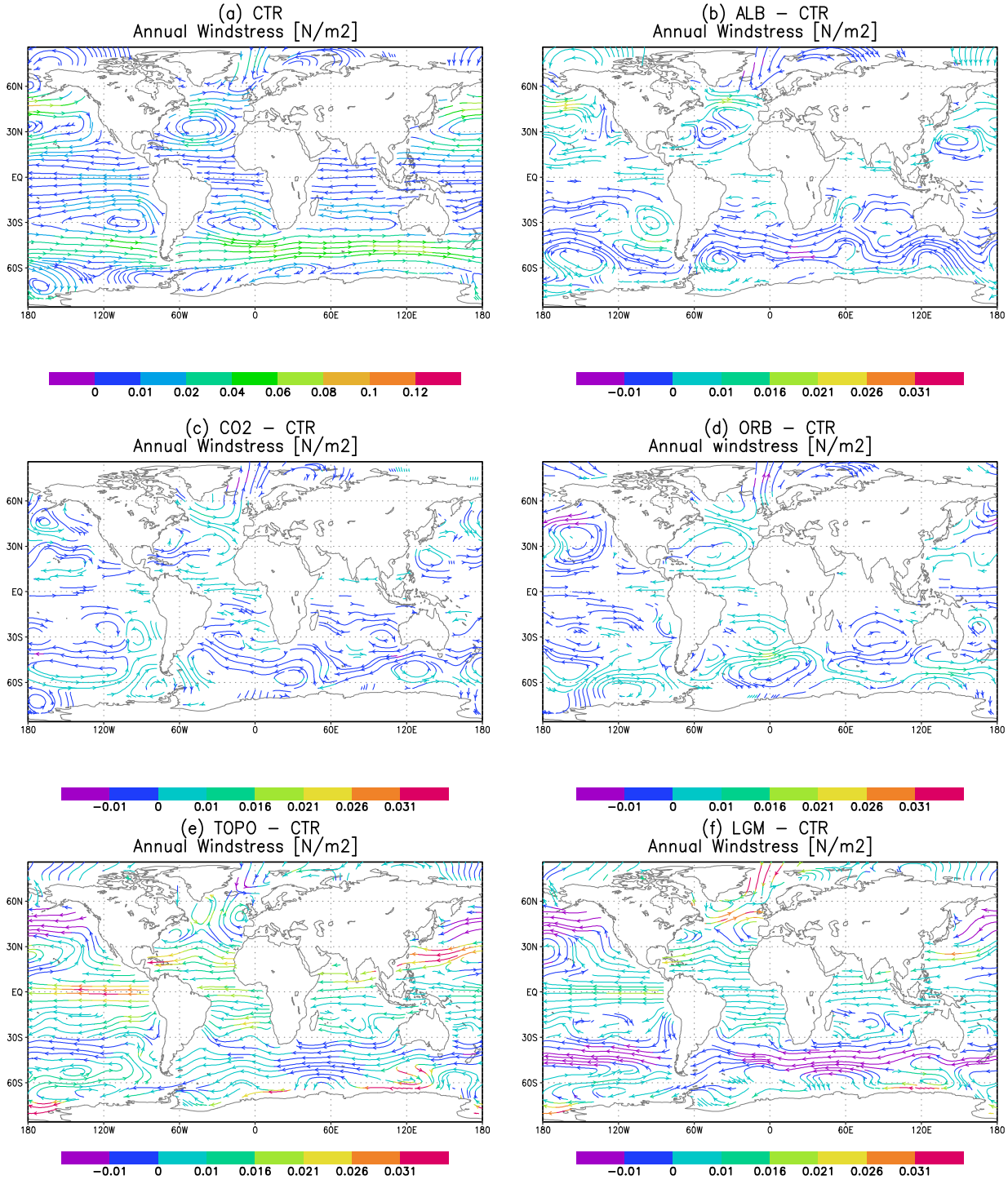

Fig. 4.1: *Time averaged annual mean wind stress for CTR and sensitivity experiments anomalies with respect to CTR* $[Nm^{-2}]$ *. (a) CTR (b) ALB-CTR (c) CO2-CTR (d) ORB-CTR (e) TOPO-CTR (f) LGM-CTR.*

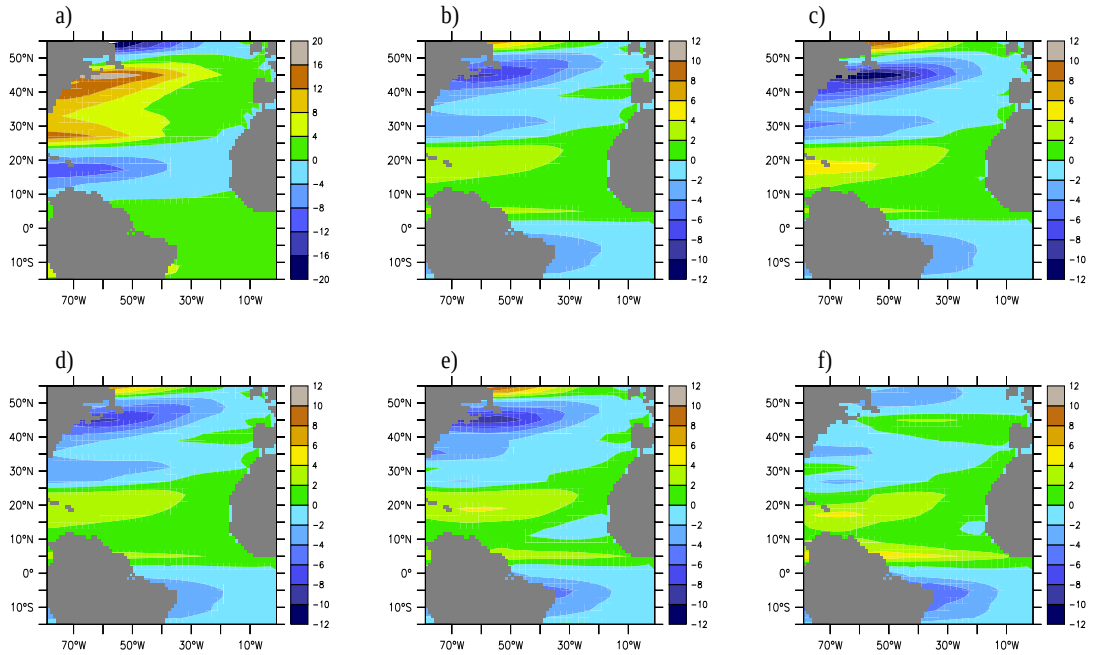

Fig. 4.2: *Time averaged annual mean Sverdrup transport [Sv] in the North Atlantic for CTR (a), and the sensitivity experiment anomalies ALB-CTR (b) CO2-CTR (c) ORB-CTR (d) TOPO-CTR (e) LGM-CTR (f). Positive and negative values denote a clockwise and anti-clockwise circulation, respectively.*

resolution employed here (Fig. 4.2a). The Sverdrup transport is defined as:

$$\psi(x) = \frac{1}{\beta\rho}\int_{x_e}^{x}\frac{\partial\tau_x}{\partial y}dx \tag{4.1}$$

where β is the meridional derivative of the Coriolis parameter, ρ is the mean density of sea water and τ_x is the zonal component of the wind stress. The integral is computed from the eastern to the western boundary in the North Atlantic and North Pacific using modeled atmospheric wind stress data.

The Sverdrup transport anomalies between the sensitivity experiments and CTR (Fig. 4.2) clearly show an overall weakening of the mass transport in the subtropical gyre (30°N-50°N) as a result of reduced wind stress curl. This weaker subtropical gyre, in turn, reduces the amount of warmer water that reaches the North Atlantic and the Nordic Seas in the *LGM* experiments. Changes of the wind stress pattern also generate weaker subtropical/tropical cells leading to reduced poleward surface heat transport. An overall weakening of the circulation by up to 16 Sv ($1Sv = 10^6 m^3 s^{-1}$) can be observed. The wind stress anomalies generate substantial changes of the surface ocean currents. In all experiments an anti-cyclonic circulation anomaly is found in the North Atlantic between 40-60°N (Fig. 4.3). Furthermore, as a result of the strengthening of the trade winds in the equatorial region, the North Equatorial Current (NEC) is stronger than the CTR NEC for all experiments (Fig. 4.3d). Furthermore, a slightly stronger Gulf Stream is found in ALB, CO2 and ORB, however, it is weaker in TOPO and LGM. The weakening of the Gulf Stream during the *LGM* has also been inferred

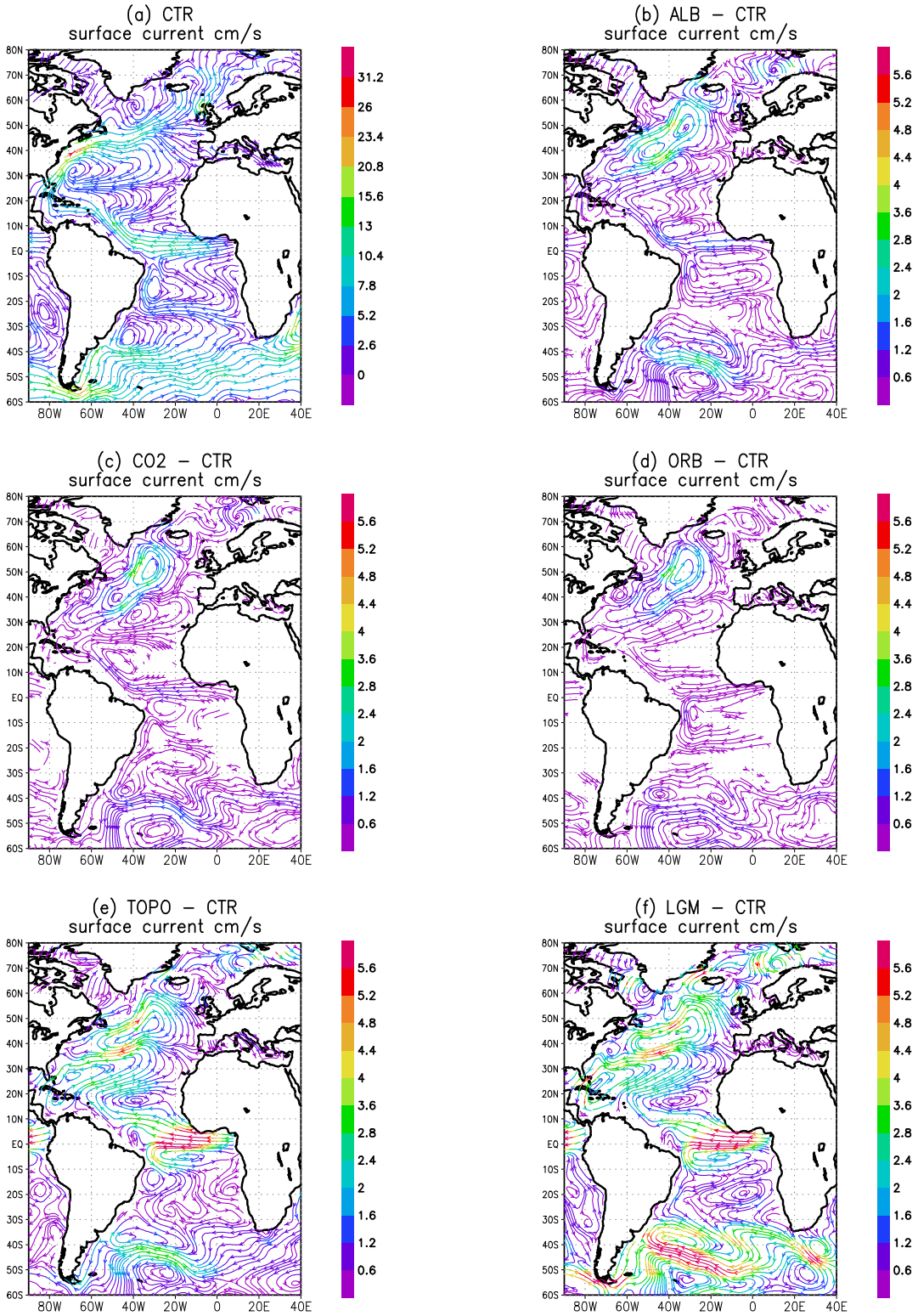

Fig. 4.3: *Time averaged annual mean surface currents [cm/s] for CTR run (a) and sensitivity experiments anomalies (b) ALB-CTR (c) CO2-CTR (d) ORB-CTR (e) TOPO-CTR (f) LGM-CTR.*

from oxygen-isotope ratios of benthic foraminifera through the reduced density contrast across the Florida Strait *(Stieglitz et al. 1999)*.

As compared to observations *(Silveira et al. 1994; Peterson and Stramma 1991; Richardson and Walsh 1988)* the equatorial surface current pattern in the SH is not simulated properly in the CTR run. For instance, the South Equatorial Current (SEC) is positioned too far south and an unrealistic cyclonic circulation between the equator and 20°S takes place (Fig. 4.3a). This cyclonic gyre "resembles" the North Equatorial Counter Current (NECC), although, it shows a northwestern-southeastern tilt. In the sensitivity experiments, a weaker Brazil Current, reduced southern subtropical gyre, and weaker South Atlantic and Circumpolar Currents are simulated. These anomalies are stronger in the TOPO and LGM runs (Fig. 4.3e,f).

Circulation changes are tightly linked also to sea surface temperature changes. Changes of SST are presented in Table 4.1 and Figure 4.4. Global and regional, SST anomalies show a general cooling, except for ALB and TOPO between 30-90°S (Table 4.1), and TOPO in the northeast Pacific (Fig. 4.4d). In the NH mid-latitudes, ALB is mostly responsible for the cooling in the LGM followed by CO2 and ORB. This large extra-tropical cooling in the ALB is primary a result of the North Atlantic cooling, since the associated SST changes in the North Pacific are much weaker (see Fig. 4.4b). In the tropics, between 30°S-90°S, and globally averaged, the reduction of atmospheric CO_2 concentration plays the most important role in cooling the ocean. As found for the globally averaged air temperature anomalies at 2m, the TOPO experiment shows weak SST anomalies due to the North Pacific warming. The anomalies in the LGM show a clearly nonlinear behaviour since the sum of the anomalies in the sensitivity experiments can not reproduce the total LGM cooling. Another interesting feature revealed by Table 4.1 is the uniform SST response to the changes in the orbital forcing, a global and regional cooling by about 0.07°C. The tropical and global cooling simulated in the LGM are very similar the results found by *Weaver et al. (2001)* which are based on an ocean GCM coupled to an energy-moisture balance atmosphere.

Sensitivity Exp.	Global	30°S-30°N	30-90°N	30-90°S
TOPO	-0.03	-0.25	0.12	0.23
ALB	-0.19	-0.24	-0.54	0.11
CO2	-0.24	-0.33	-0.23	-0.09
ORB	-0.07	-0.07	-0.07	-0.08
LGM	-1.35	-1.24	-1.24	-1.62

Tab. 4.1: *Time averaged annual mean SST anomalies between the LGM sensitivity experiments and CTR [°C].*

Figure 4.4 shows the SST anomalies between the sensitive experiments and CTR as well as the annual mean sea-ice margin for each experiment. The SST changes due to albedo changes show a strong North Atlantic cooling (Fig. 4.4b). Both, the southward extension of the sea-ice margin in ALB and enhanced cold air advection from Canada over the Labrador and Nordic Seas play an important role to cool the high latitudes. Furthermore, changes of the wind-driven ocean circulation in ALB have

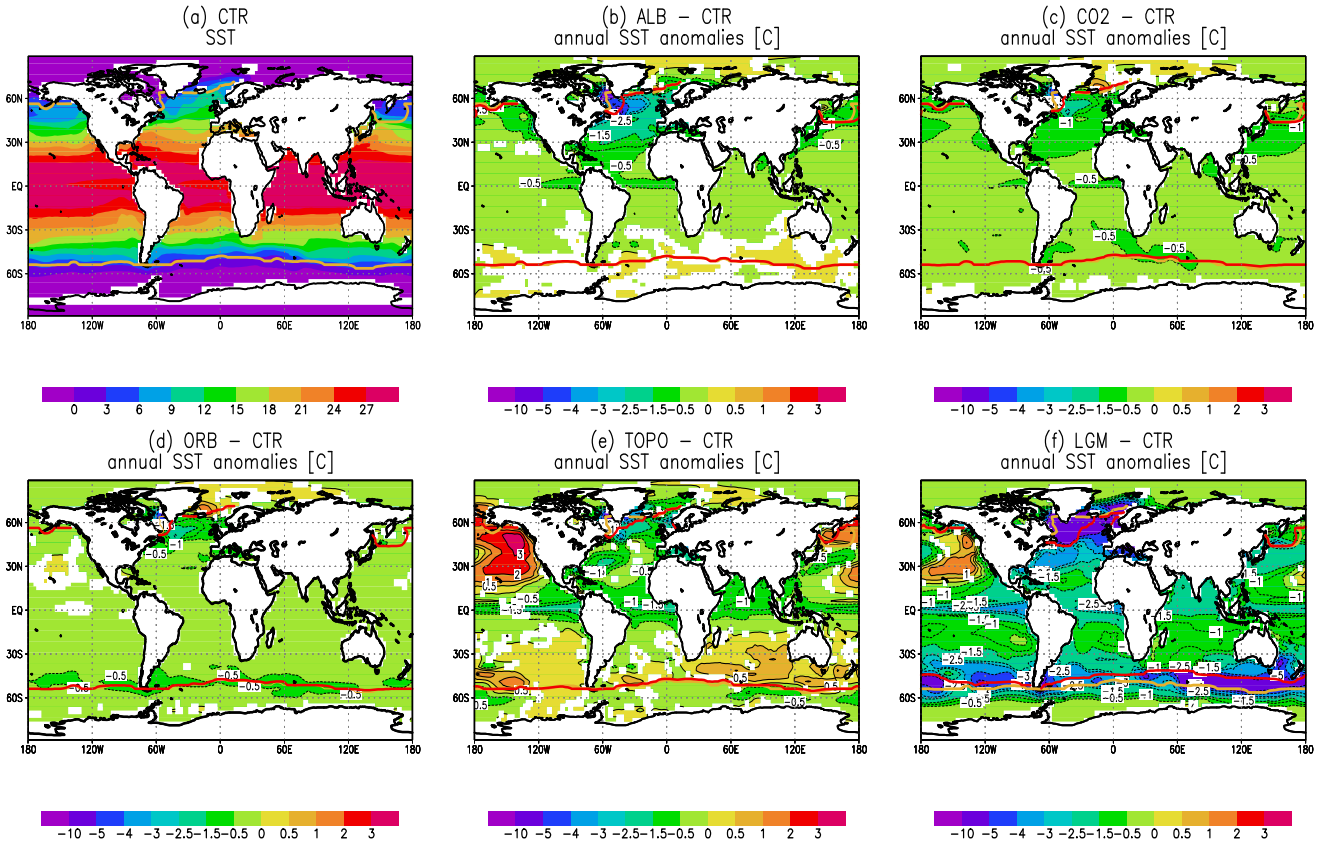

Fig. 4.4: *Time averaged annual mean sea surface temperature for CTR (a) and sensitivity experiments anomalies [°C], (b) ORB-CTR (c) ALB-CTR (d) CO2-CTR (e) TOPO-CTR (f) LGM-CTR. Sea-ice margin in CTR (yellow line) sea-ice margin in the sensitivity experiments (red line). Shaded areas are statistically significant at 95% level based on calculations of student's t-test with 300 degrees of freedom.*

a strong influence on the SST reduction in mid-latitudes. For example, the southward flow anomalies which result from a stronger cyclonic circulation anomaly (Fig. 4.3b) transport cold waters to the western Europe, generating a cooling in these areas. In the equatorial region, on the other hand, the lower SST results from a strengthening of the upwelling and Ekman circulation linked to enhanced equatorial trade winds. Moreover, *Broecker (1995a)* argued that the reduced water vapour and consequently the weaker greenhouse capacity of atmosphere also plays an important role in the glacial oceanic cooling.

Northern Hemisphere SST anomalies in the CO2 experiment have a very similar pattern as the one generated in the ALB experiment (Fig. 4.4b,c). In the SH, however, the weak positive SST anomalies in ALB are not simulated by the CO2 experiment. This is in agreement with the reduced water vapour simulated by the CO2 run (see

Fig. 3.6). Despite substantial SST changes in the North Atlantic, the sea-ice margin in both experiments (ALB and CO2) shows a slightly equatorward extension in the Labrador Sea. The ORB experiment (Fig. 4.4d) displays an overall weak cooling of about 0.5°C, except for the North Atlantic region, where larger anomalies of up to -2°C are found.

In the TOPO experiment, the SST anomalies in the North Atlantic show a general cooling (Fig. 4.4e). In the equatorial Atlantic the SST drops by up to 3°C and anomalies of up to -10°C are found in high latitudes of the NH. These values are very similar those simulated by GFDL's Modular Ocean Model *(Bush and Philander 1999)*. The North Atlantic cooling is mainly a result of 3 effects: (1) Enhanced cold air advection from Laurentide ice sheet, (2) the weaker subtropical gyre, (3) and the weaker greenhouse capacity due an overall reduction of specific humidity. Although the topographic and albedo changes alone largely explain the SST pattern in the LGM, in particular in the North Atlantic, the other boundary conditions also contribute to cooling of the subtropical regions in the northern and southern hemispheres. This can be seen from the larger negative SST anomalies in LGM as compared to those simulated by TOPO (Fig. 4.4e,f).

As discussed in the introduction, the issue of equatorial and North Pacific SSTs changes during the *LGM* remains controversial. Both, model simulations and paleodata disagree in terms of the magnitude and pattern of the SST changes. The most striking SST feature in ECBilt-Clio LGM experiment is the warming of the subtropical and extra-tropical northeastern Pacific. This northeastern Pacific warming is opposed by a cooling in the Kuroshio area, in agreement with GLAMAP reconstruction *(Schäfer-Neth and Paul 2003)* reconstruction (Fig. 4.5). Compared to terrestrial/tropical paleodata, however, the ECBilt-Clio LGM simulation reveals some differences: For instance, the reconstructed cooling of northeastern Brazil of 5°C *(Stute et al. 1995)*, attains values of 2-3°C.

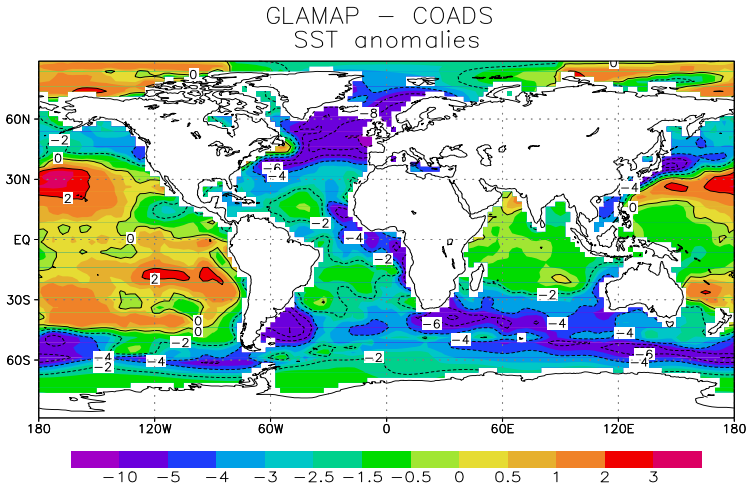

Fig. 4.5: *Reconstructed SST differences between LGM (GLAMAP) and present day (COADS) [°C].*

The simulated tropical Pacific LGM SST anomalies clearly show a kind of La Niña pattern very similar to a present-day La Niña situation. In fact, despite the QG approximation, ECBilt-Clio simulates the atmospheric response to an EL Niño/La Niña SST anomaly similar to primitive equation GCMs in T21 resolution *(Timmermann et al. 2004; Lau and Nath 1996)*. As compared to reality, however, the magnitude of the response is underestimated by a factor of 2-3, which is typical for coarse-resolution atmospheric models. In order to examine the physical mechanisms responsible for the SST anomalies over the equatorial and North Pacific in TOPO and LGM, it is important to investigate the simulated changes of the mean atmospheric circulation and its transient eddy wave activity. As discussed by *Cook and Held (1988)* the presence of Laurentide ice sheet over North America creates a dowstream blocking that imposes an anomalous meridional wind velocity v′, that is proportional to the zonal mean wind $\overline{u}$ and the zonal topographic gradient $\frac{\partial h}{\partial \lambda}$ (Eq. 4.2),

$$v' \approx -\frac{\overline{u}}{cos\phi}\frac{\partial h}{\partial \lambda}\frac{\partial \overline{\Theta}/\partial z}{\partial \overline{\Theta}/\partial \phi} \tag{4.2}$$

The third term in the equation ($\frac{\partial \overline{\Theta}/\partial z}{\partial \overline{\Theta}/\partial \phi}$) is the slope of an isentropic surface and can be computed from the zonally averaged static stability and the meridional zonally averaged temperature gradient. As discussed previously, the relatively weak meridional thermal gradient over the glacial North Pacific leads to a weakening of the thermal wind, which in turn reduces eddy activity and the upper level westerlies. In the LGM experiment

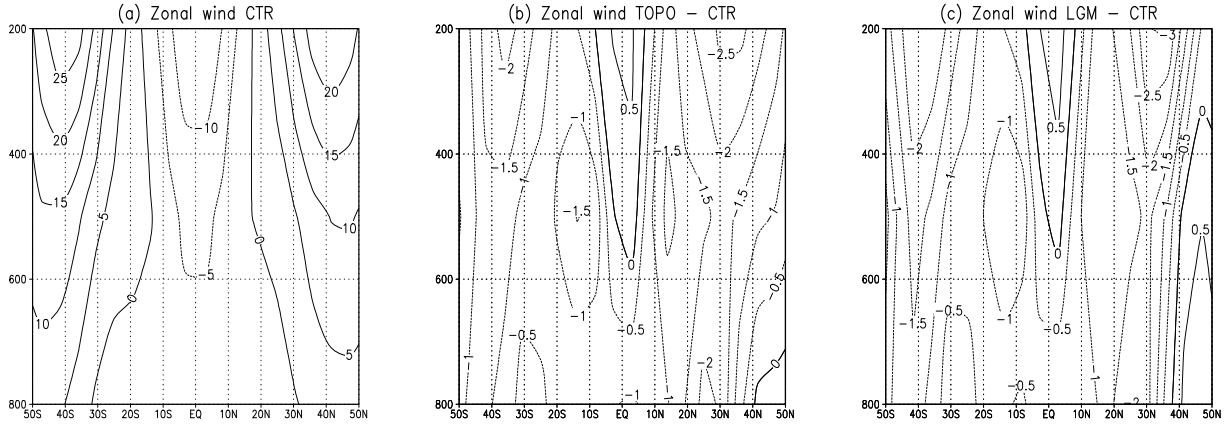

Fig. 4.6: *Time averaged zonal mean of zonal wind component [ms^{-1}] CTR (a), TOPO-CTR (b) LGM-CTR (c).*

the static stability of the atmosphere ($\frac{\partial \overline{\Theta}}{\partial z}$) is enhanced, which leads to an enhancement of the southerly flow anomaly on the western flank ($\frac{\partial h}{\partial \lambda} > 0$) of the ice sheets. The absolute value of the zonally averaged meridional temperature gradient ($\frac{\partial \overline{\Theta}}{\partial \phi}$) increases also during the *LGM*, thereby reducing the topographically induced flow anomaly. Neglecting the changes of ($\frac{\partial \overline{\Theta}}{\partial \phi}$), Eq. 4.2 describes why downstream lows and upstream

highs are generated due to topographic forcing. According *Holopainen et al. (1982)*, and *Kuo (1956)* the changes of the eddy momentum flux convergence have the potential to accelerate or decelerate zonal circulations and to induce secondary meridional circulation anomalies. *Timmermann et al. (2004)* analysing the atmospheric response to the Laurentide ice sheet found a strong upper level total (transient+stationary) eddy momentum flux anomaly at a latitude of about 40°N. Furthermore, it was found that the glacial changes of the magnitude of the meridional gradient of the total eddy

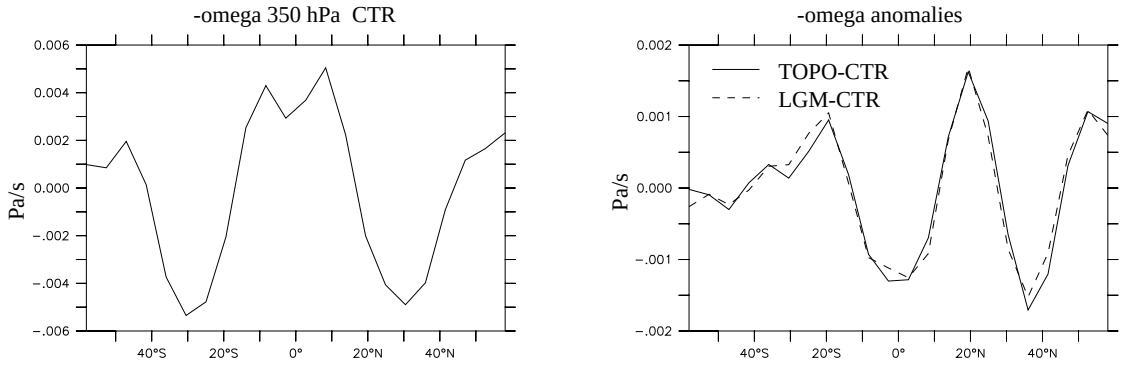

Fig. 4.7: *350hPa zonally averaged negative vertical velocity in the Pacific Ocean (omega) [Pa/s]. (a) CTR and (b) difference between LGM and CTR (dashed line) and TOPO and CTR (solid line). Negative values indicate descending motion, positive values ascending motion.*

momentum flux is highest in the subtropics. The reduced upper-level divergence near 30°N-40°N induces deceleration of the upper level westerlies (Fig. 4.6b,c) as well as a clockwise circulation with ascending motion at about 10-30°N and descending motion around 30-50°N. This secondary circulation can be derived theoretically from the Kuo-Eliassen equation *(Kuo 1956)*. The zonally averaged vertical velocity anomalies trigger a surface high pressure anomaly between 30°-50°N (descending motion) and a low pressure anomaly between 10°N and 30°N (ascending motion) (Fig. 4.7). This positive meridional pressure gradient anomaly at the surface is accompanied by a strengthening of the zonal component of the trade winds in agreement with the near-geostrophic balance (Fig. 4.6b,c).

Due to the atmospheric circulation anomalies, one may expect changes in the wind-driven oceanic circulation. In order to diagnose such changes of the wind-driven circulation the Sverdrup transport in the North Pacific is calculated (Fig. 4.8). The reduction of the mean wind stress curl over the west Pacific leads to a spin-down of the subtropical and the subpolar gyres. This favors a surface cooling in Kuroshio area and a warming of the eastern North Pacific trough changes of the meridional heat transport by the subtropical gyre. Furthermore, the supply of cold waters from the subpolar area to the eastern North Pacific is diminished, thereby favouring a slight warming in this area (Fig. 4.8, 4.9). A similar feature, cooling in the west and warming in the east Pacific, is also found in the GLAMAP reconstruction (Fig. 4.5). Comparing the Sverdrup transport anomalies among the sensitivity experiments (Fig. 4.8), it is clearly

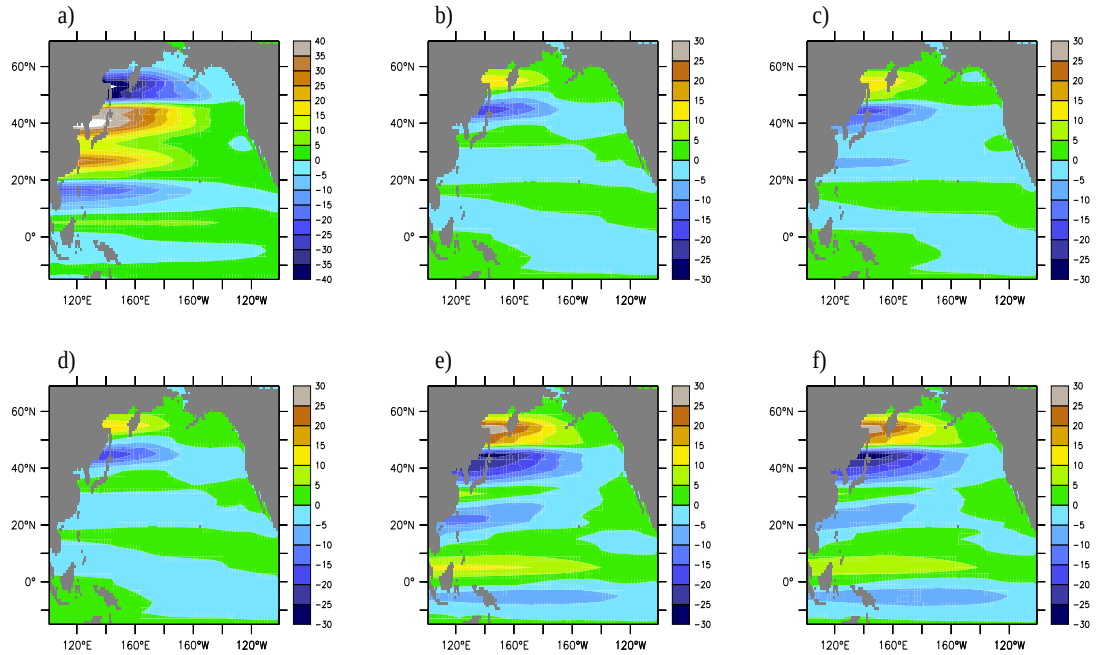

Fig. 4.8: *Time averaged annual mean Sverdrup transport [Sv] in the North Pacific for CTR (a) and sensitivity experiments anomalies, ALB-CTR (b) CO2-CTR (c) ORB-CTR (d) TOPO-CTR (e) LGM-CTR (f).*

seen that the wind-driven circulation in the North Pacific is mostly generated by the wind stress changes imposed by the Laurentide ice sheet.

McCreary and Lu (1994) and Liu and Philander (1995) argued that the strength of the subtropical cells as well as the magnitude of equatorial upwelling are tightly dependent on the wind stress near 10°N-20°N. Thus, one should expect that the stronger trade winds described above will intensify the subtropical cells through changes of the Ekman transport. For instance, an intensification of the trade winds by 30-50% leads to an enhancement of the meridional transport of about 2 Sv and an equatorial cooling of approximately 2°C *(Klinger et al. 2002; Liu and Philander 1995)*. These values are in good agreement with the simulated LGM anomalies triggered by the overall strengthening of the trade winds (see Figs. 4.4f, Figs. 4.8f). The changes of the Sverdrup transport are well captured also by the surface current anomalies. Figure 4.9 shows a substantial weakening of the Kuroshio Current as well as an intensification of the equatorial current system in TOPO and LGM. A strengthening of the SEC enhances the poleward heat transport, thereby warming up the subtropical Pacific and cooling the equatorial Pacific. The associated horizontal temperature advection leads to a warming of the central Pacific by about 0.2K/month *(Timmermann et al. 2004)*.

The changes due to the albedo, reduced atmospheric CO_2 concentration and orbital forcing are much weaker, but they contribute to the cooling of the Kuroshio region and to the warming in northeastern Pacific (Fig. 4.8). Another mechanism that contributes to the North Pacific warming is associated with the subtropical atmospheric teleconnection of the permanent La Niña state. These teleconnection are characterised by a reduction of the subtropical wind-strength, and hence of latent cooling of the ocean

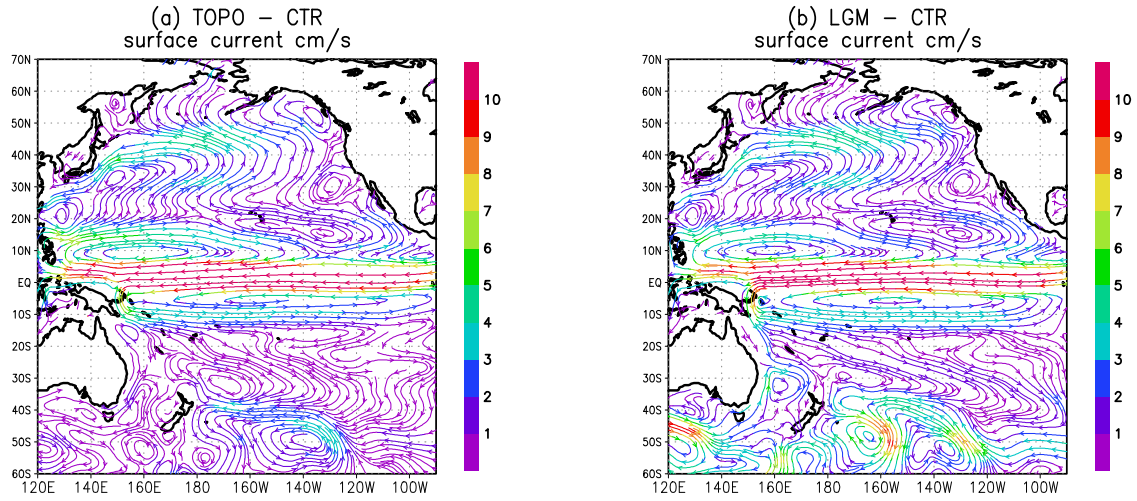

Fig. 4.9: *Time averaged annual mean surface currents anomalies with respect to CTR [cm/s]. (a) TOPO-CTR (b) LGM-CTR.*

and changes of the sensible heat flux. These changes are also typical for a present day La Niña situation (for further details, see *Timmermann et al. 2004).*

In order to investigate the influence of wind stress changes to the generation of SST anomalies in the equatorial Pacific, several wind stress sensitivity experiments are performed. The forcing function in the meridional direction is multiplied with the simulated zonal wind stress component. The function is defined as $[1 + a \times e^{[\frac{2(\gamma_r - \gamma)^2}{\alpha}]}]$, a is the amplitude factor (0.5, 1 and 1.5), γ_r is the latitude of anomaly maximum (10°N, 15°N, 20°N and 25°N), and α is the width of the anomalous wind stress forcing. An example of the wind stress forcing is shown in Figure 4.10a at 15°N. Figure 4.10b shows the SST anomalies with respect to the LGM experiment averaged between 5°S-5°N simulated by the wind stress sensitivity experiments.

Figure 4.10b highlights the strong influence of the wind stress on the equatorial SST pattern. In the first experiment the forcing is applied at 10°N with $a = 0.5$, i.e., the zonal wind stress is increased there by 50%. The associated SST cooling attains values of about 2°C. This is significant given the fact that the SST changes associated to the present day La Niña are of the same magnitude. The forcing applied further north (15°, 20°N and 25°N) generates a much weaker equatorial SST response. Moreover, it becomes evident that the SST response also depends on the magnitude of the wind stress changes. For example, an increase of the zonal wind stress by about 150% at 25°N generates an equatorial cooling of 8°C, but if an anomalous forcing of a similar strength is applied at 10°N the SST drops by 15°C (Fig. 4.10b). The experiments above highlights the importance of off-equatorial wind stress changes in driving the subtropical/tropical cells as well as equatorial SST anomalies.

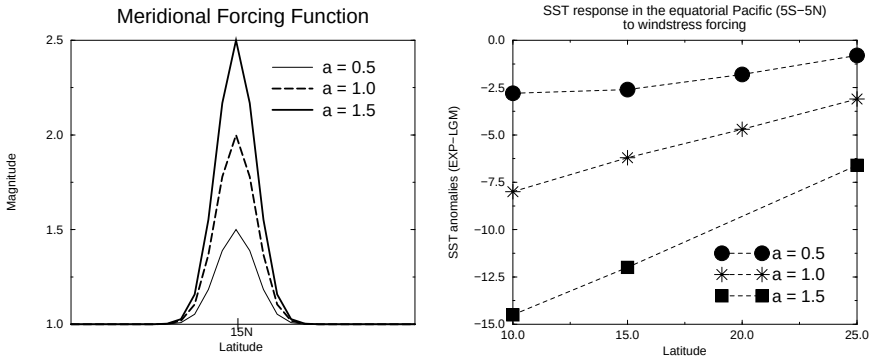

Fig. 4.10: *Windstress forcing at 15°N (left panel) and SST response averaged between 5°N-5°S in Pacific Ocean (right panel). The latitudes in the right panel indicate where the forcing was applied i.e. 10°N, 15°N, 20°N and 25°N.*

4.3 Sea-ice

The changes of the atmospheric and oceanic circulations in the LGM result in substantial changes in both, sea-ice area and sea-ice volume. Moreover, modifications of ice extent can feed back on to the atmospheric and oceanic circulations thereby serving as an important climate feedback component *(Mysak and Venegas 1998)*. For example, changes in the buoyance forcing resulting from sea-ice melting and brine rejection during the sea-ice formation can trigger different states of the thermohaline circulation *(Ganopolski and Rahmstorf 2001; Manabe and Stouffer 1997; Fanning and Weaver 1997; Rahmstorf 1995)*.

Figure 4.11 displays time series of the simulated hemispherically averaged sea-ice area and sea-ice volume for CTR and the sensitivity experiments during the last 300 years of the simulations. As mentioned briefly in Chapter 2, the model can well simulate the observed present day sea-ice area. Nevertheless, there is no precise estimates of the sea-ice volume based on observation because of the sparseness of ice-thickness measurements. Comparing the simulated present-day sea-ice volume in the NH ($55.8 \times 10^3 km^3$) to the results obtained by *Hilmer and Lemke (2000)* using a dynamic-thermodynamic-sea-ice model driven by NCEP-NCAR Reanalysis forcing data, one finds that ECBilt-Clio (version 2) overestimates the sea-ice volume by a factor of 2 due to the larger sea-ice thickness. Figure 4.11a shows that the changes of the NH sea-ice area in TOPO, ORB and CO2, are relatively weak as compared to LGM. The reduction of the the sea-ice area in the North Pacific due to the topographically induced positive SST anomalies is partially compensated by an increase in the North Atlantic. The ALB simulation, however, exhibits an increased sea-ice area (Fig. 4.11a) due to an overall oceanic cooling of the ocean (see Fig. 4.4b). Despite the relatively small changes in ALB, TOPO, CO2 and ORB the changes of sea-ice area and volume in LGM are large and correspond to about 25% of the CTR value. (see Figs. 4.11a and 4.12c).

In the SH the sea-ice response to the individual glacial boundary conditions is weaker than simulated in the NH. Nevertheless, it is important to note that the joint

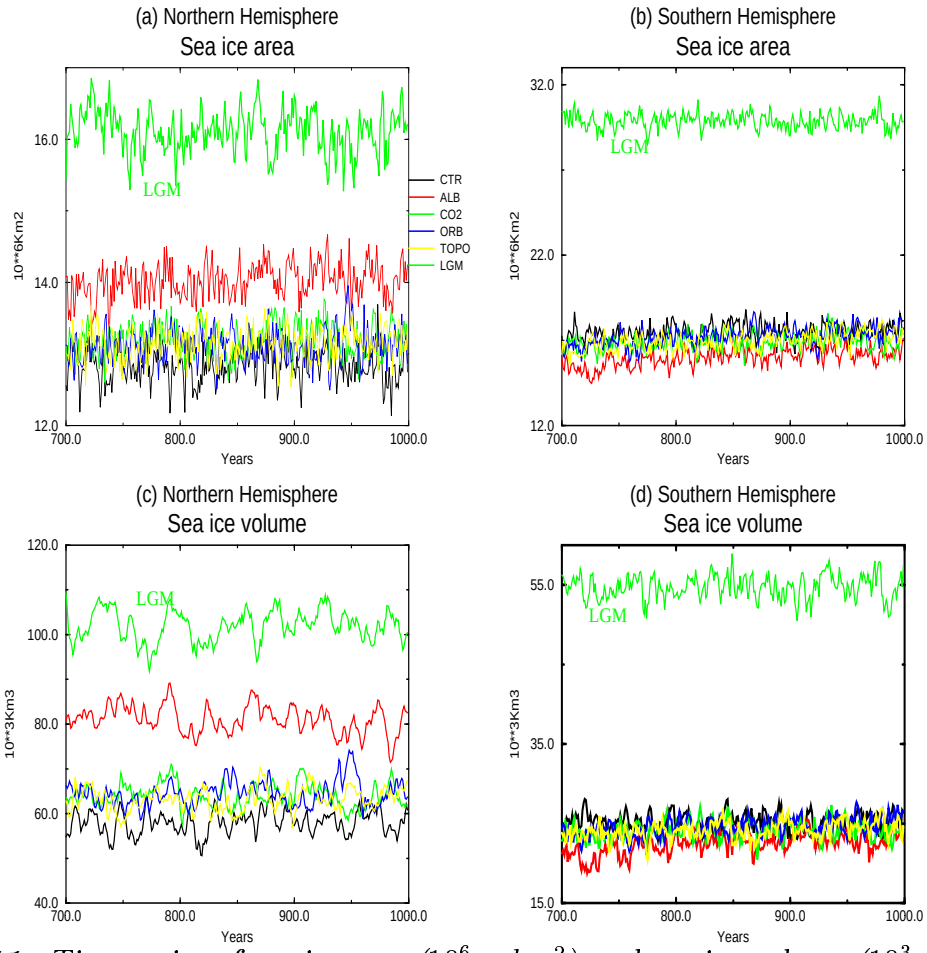

Fig. 4.11: *Time series of sea-ice area ($10^6 \times km^2$) and sea-ice volume ($10^3 \times km^3$) in the sensitivity experiments. (a) NH and (b) SH. (c) and (d) the same as (a) and (b) but for the sea-ice volume.*

effect of the boundary condition changes captured in LGM increases the sea-ice by more than 100% (Fig. 4.11b). The comparison between the LGM and the other sensitivity experiments in the SH indicates that the mechanism leading to sea-ice changes in the LGM is highly nonlinear, since the sum of the sensitivity experiments anomalies is smaller than the differences between the LGM and CTR. Sea-ice volume shows a very similar behaviour in the NH (Fig. 4.11c,d), the glacial sea-ice volume is almost 80% larger than in CTR, whereas in the SH, it is about three times larger than for the present-day climate. One should keep in mind that the sea-ice thickness simulated by ECBilt-Clio is overestimated in the CTR climate. Hence, such a bias may also influence the glacial sea-ice anomalies.

Figure 4.12 displays the simulated sea-ice thickness distribution for CTR and LGM. The differences between these simulations are remarkable. In the LGM, the sea-ice thickness increases in the Arctic Ocean, the North Atlantic and around Antarctica. In the central Arctic the sea-ice thickness increases by more than 5m. In the North Atlantic the most important feature is the southward shift of the sea-ice margin that

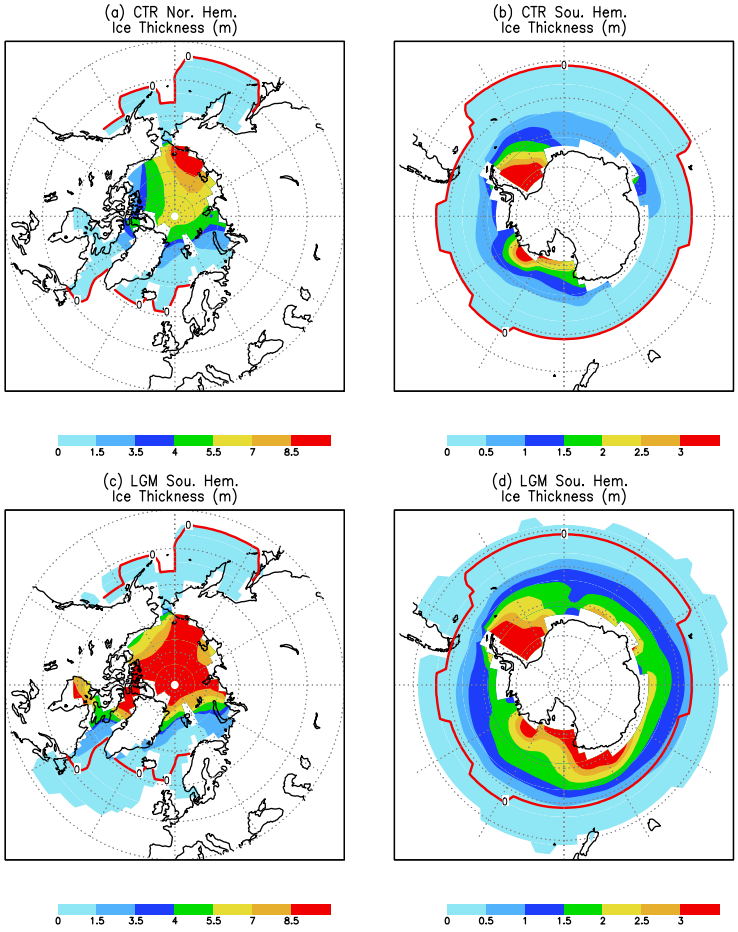

Fig. 4.12: *Time averaged annual mean sea-ice thickness [m] in the CTR (a) and (b), and LGM simulation (c) and (d). The red line is the sea-ice margin in the CTR run.*

moves equatorward by almost 15° (Fig. 4.12c). These changes can be attributed to the SST anomalies in the North Atlantic which drop by about 10°C-15°C. The changes in Antarctica are even more spectacular. The sea-ice margin moves equatorward reaching the southern part of New Zealand and Argentina.

4.4 Sea Surface Salinity

Changes of the atmospheric circulation, the SST, and the sea-ice volume lead to important changes in Sea Surface Salinity (SSS). The simulated SSS anomalies between the *LGM* sensitivity experiments and CTR are shown in Figure 4.13a. It should be noted that the glacial sea level drop of 120 m and the associated increase of global salinity by about 1 psu (practical salinity unit) are not captured by the ECBilt-Clio LGM experiments. Furthermore, changes of the runoff mask, and - most important -

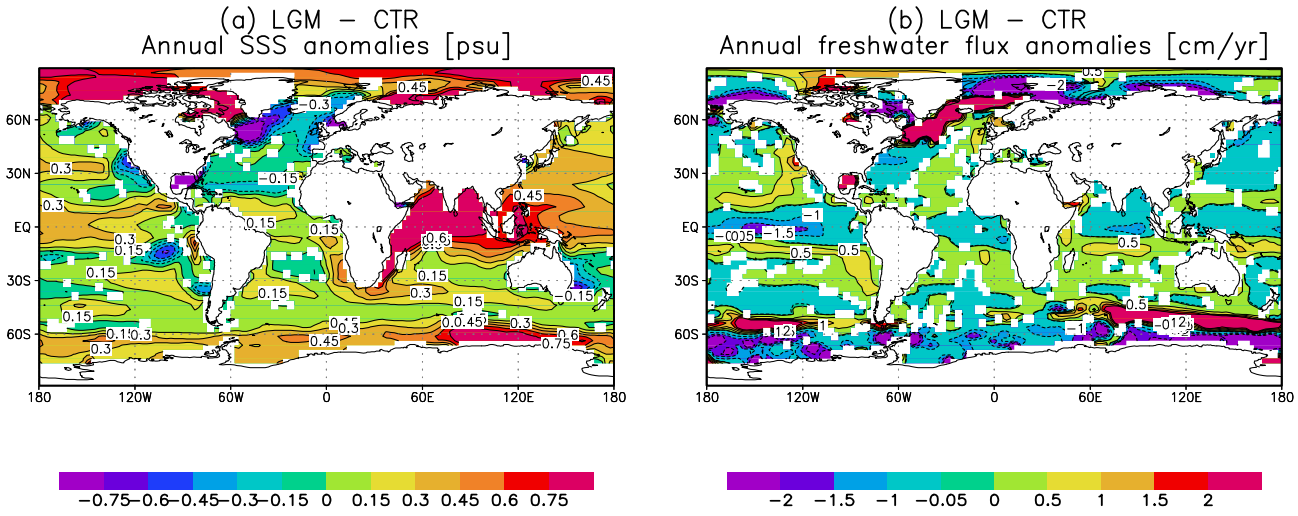

Fig. 4.13: *Time averaged annual mean anomalies between the LGM experiment and CTR for SSS [psu] (a) and freshwater [cm/yr] (b). Shaded areas are statistically significant at 95% level based on calculations of student's t-test with 300 degrees of freedom. Negative values in (b) mean excess of evaporation over precipitation*

the uncertainties of ice sheet ablation during the *LGM* are not taken account here. A freshening of the North Atlantic is evident in all experiments, whereas, positive SSS anomalies are observed in the tropics due to reduced precipitation and lower temperatures. This is also in agreement with the aridity index (Table 3.4), that indicates an excess of precipitation over evaporation in the mid and high latitudes and a deficit in the tropics. Positive SSS anomalies in the equatorial zone are in part due to negative freshwater flux anomalies at the ocean surface (Fig. 4.13b). In addition to the simulated changes in the North Atlantic, there is also a large positive SSS anomaly in the Indian Ocean. This anomaly originates from a substantial reduction of the Asian summer monsoon and the corresponding negative fresh water flux anomalies (Fig. 4.13b).

In polar latitudes, the salinity increases mainly due to the brine rejection during the process of sea-ice formation. Despite the enhanced sea-ice area in the LGM no positive SSS anomalies are simulated. The brine released anomaly is over compensated by a increased freshwater flux which accompanies the enhancement of the LGM storm track over the North Atlantic (Fig.4.13b).

4.5 Comparison with Paleodata

In order to test the validity of the modeling results it is necessary to compare the simulated oceanic anomalies in the LGM to available paleoreconstructions. However, it should also be noted that many of these reconstructions have large uncertainties. The simulated LGM SST, SSS and sea-ice margin are compared to the GLAMAP

paleoreconstruction data set. The GLAMAP reconstruction *(Schäfer-Neth and Paul 2003)* presents a new reconstruction of SST, SSS and sea-ice margin for the North and South Atlantic during the *LGM*. This reconstruction is based on the analyses of 275 sediments cores between the North Pole and 60°S. Stratigraphies have been carefully derived from cores chronostratigraphies *(see Sarnthein et al. 2003 for an overview)*. GLAMAP provides a new LGM SST reconstruction for the Atlantic, and includes the *CLIMAP (1981)* reconstruction for Indian and Pacific Oceans. Most significant differences between CLIMAP and GLAMAP occur in the tropical region and the North Atlantic/Nordic Seas sector. According to the CLIMAP reconstruction, the *LGM* anomalies with respect to today's climate do not exceed -2°C in the tropics. CLIMAP's tropical temperature reconstruction are in disagreement with the various land-based paleotemperature that suggest a glacial cooling of -5°C *(Anderson and Webb 1994; Guilderson et al. 1994)*. Another controversial point concerning the CLIMAP reconstruction are the extremely cold Nordic Seas and the annually persistent sea-ice cover. This glacial scenario is opposed by reconstructions that indicate at least seasonally ice-free conditions during the *LGM (Sarnthein et al. 1995)*. Furthermore, compared to CLIMAP, GLAMAP exhibits much colder tropical and subtropical regions, and warmer high latitudes in particular during summer *(Schäfer-Neth and Paul 2003)*. GLAMAP's low SST in the tropical and subtropical areas are also consistent with estimates based on other proxy data *(Crowley 2000, Guilderson et al 1994)*.

The differences between the simulated SST and SSS in the LGM and reconstructed GLAMAP SST and SSS fields are depicted in Figure 4.14. It is important to note that the GLAMAP uses fixed SST of -1.8°C in areas which are covered by sea-ice. Thus, the differences northward of 70°N and southward of 60°S are not considered here. Furthermore, GLAMAP SSTs are provided for February and August only. Hence a direct comparison of simulated annual mean data with the average of February and August data might have a bias as well. Striking differences between simulated ECBilt-Clio and reconstructed GLAMAP SSTs are observed mainly in the extra-tropics. The simulated eastern North Atlantic temperatures are around 4-5°C higher than simulated by GLAMAP. This feature can be attributed to an underestimation of sea-ice cover in the NH winter. GLAMAP suggests that during the *LGM* the sea-ice margin started off the west coast of Great Britain, whereas in the ECBilt-Clio LGM simulation it starts farther north, near Scandinavia (Fig. 4.15a). In addition, the ECBilt-Clio displays a broader Gulf Stream, which leads to a warm bias in the North Atlantic area. In the equatorial Atlantic, GLAMAP and ECBilt-Clio are characterised by a similar glacial cooling, except for a model warm bias in the northern and southern upwelling regions off the coast of west Africa. ECBilt-Clio does not capture coastal upwelling properly. In contrast, in the South Atlantic the simulated SSTs are colder than in GLAMAP. It is important to stress that according to *Malmgren et al. (2001)*, SST as reconstructed using modern analog techniques has a typical uncertainty of about 1°C whereas reconstructions using the transfer function method have a slightly larger error of about 1.2°C.

A similar hemispheric contrast between simulation and reconstruction can be observed for the Pacific. The simulated cooling of the SH oceans can be partially attributed to the much larger sea-ice extent and an associated cooling of the adjacent

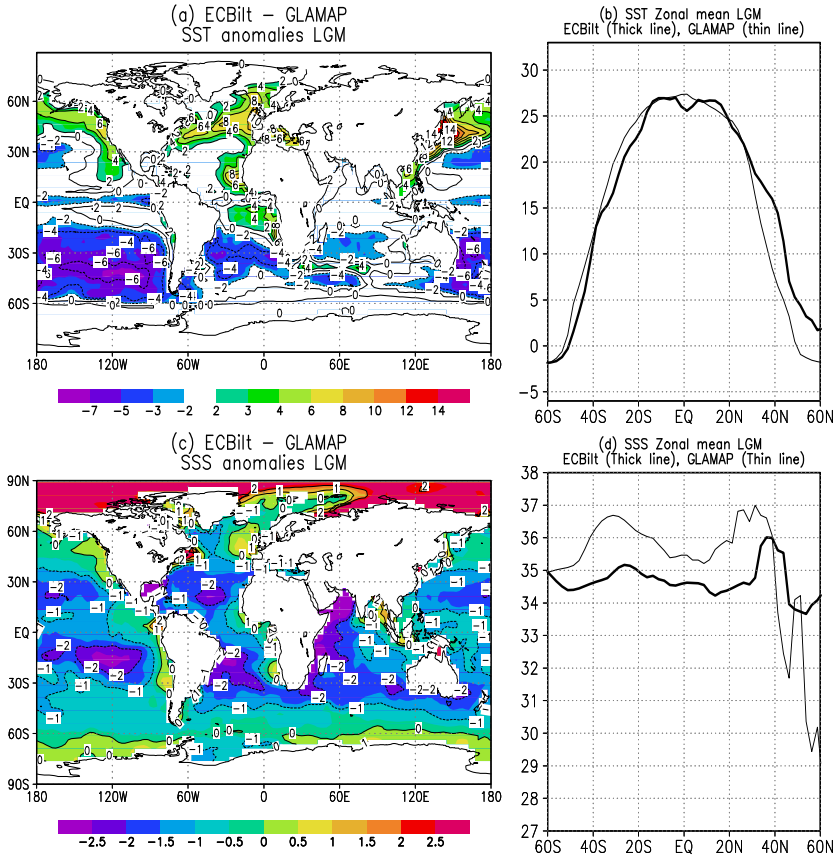

Fig. 4.14: *Differences between time averaged annual mean LGM ECBilt-Clio and the GLAMAP average between February and August. (a), (b) SST. (c) and (d) SSS.*

ocean. It is important to note that the SH warming in the GLAMAP (see Fig. 4.14) has neither been reproduced by other *LGM* simulations using the state-of-the art climate models, nor supported by paleoreconstructions *(Lee and Slowey 1999; Rind and Peteet 1985)*. In the equatorial Pacific the model shows much stronger cooling the GLAMAP/CLIMAP reconstruction. Similar cooling has also been found by the AOGCM experiments for the *LGM (Shin et al. 2003; Bush and Philander 1999)* and other proxy data *(Beck et al. 1997)*. Although the ECBilt-Clio LGM simulation and the GLAMAP reconstruction exhibit many differences, absolute temperatures appear quite similar (Fig. 4.14b).

The differences between the simulated glacial SSS are shown in Figure 4.14c. The simulated freshening in comparison with the reconstruction over most parts of the ocean is a result of neglecting the glacial sea level drop of 120 m, resulting in a homogeneous 1 psu reduction of global salinity. However, the simulated higher salinity around Antarctica is mainly a result of an increase in sea-ice volume and brine re-

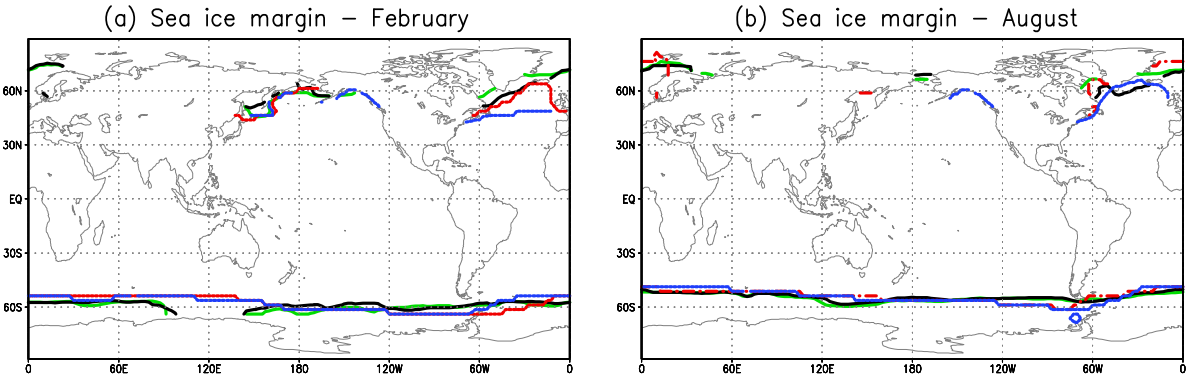

Fig. 4.15: *Maximum sea-ice margin in February (a) and August (b). Black line (ECBilt-Clio LGM), Blue line (CLIMAP), Red line (GLAMAP) and Green line (ECBilt-Clio CTR).*

leased. In terms of zonal changes (Fig. 4.14d), the model exhibits a saltier ocean north of 60°N. Whereas the GLAMAP reconstruction suggests the existence of a strong polar halocline during the *LGM*. Elsewhere, ECBilt-Clio and GLAMAP show differences of the order of 1 psu.

The simulated and reconstructed sea-ice area are plotted in Figure 4.15a,b. GLAMAP and ECBilt-Clio are in good agreement during summer and winter, however, both data are characterised by a smaller sea-ice area than in the, CLIMAP reconstruction in particular in the NH. In the SH near South America, the simulated sea-ice area is overestimated throughout the year as compared to GLAMAP. In general, the ECBilt-Clio LGM simulation reproduces quite well the seasonal variability in both hemispheres (Fig 4.15a,b).

4.6 Convective Layer Depth and Surface Density

Deep convective mixing in the North Atlantic is an essential component in driving meridional overturning flow, associated with the thermohaline circulation (THC). Today, the major sites open ocean convection are the center of the Greenland, Iceland Norwegian (GIN) Sea *(Wood et al. 1999; Visbeck et al. 1995; Schott et al. 1993)*, Labrador Sea and a small region in the northwestern Mediterranean Sea *(Schott et al. 1996)*. However, only in the Labrador and GIN Seas North Atlantic Deep Water (NADW) is formed by convection, thereby replenishing the deep water of the Atlantic, Pacific and Indian Oceans. Figure 4.16 shows the time-averaged convective-layer depth (CLD) and surface density for CTR and the anomalies between the sensitivity experiments and CTR. The shaded areas represent the CLD anomalies and the contour lines are the surface density changes.

In comparison with observations the simulated convection in Labrador Sea is too weak and GIN Seas convection is located too far north (Fig. 4.16a). A new version of

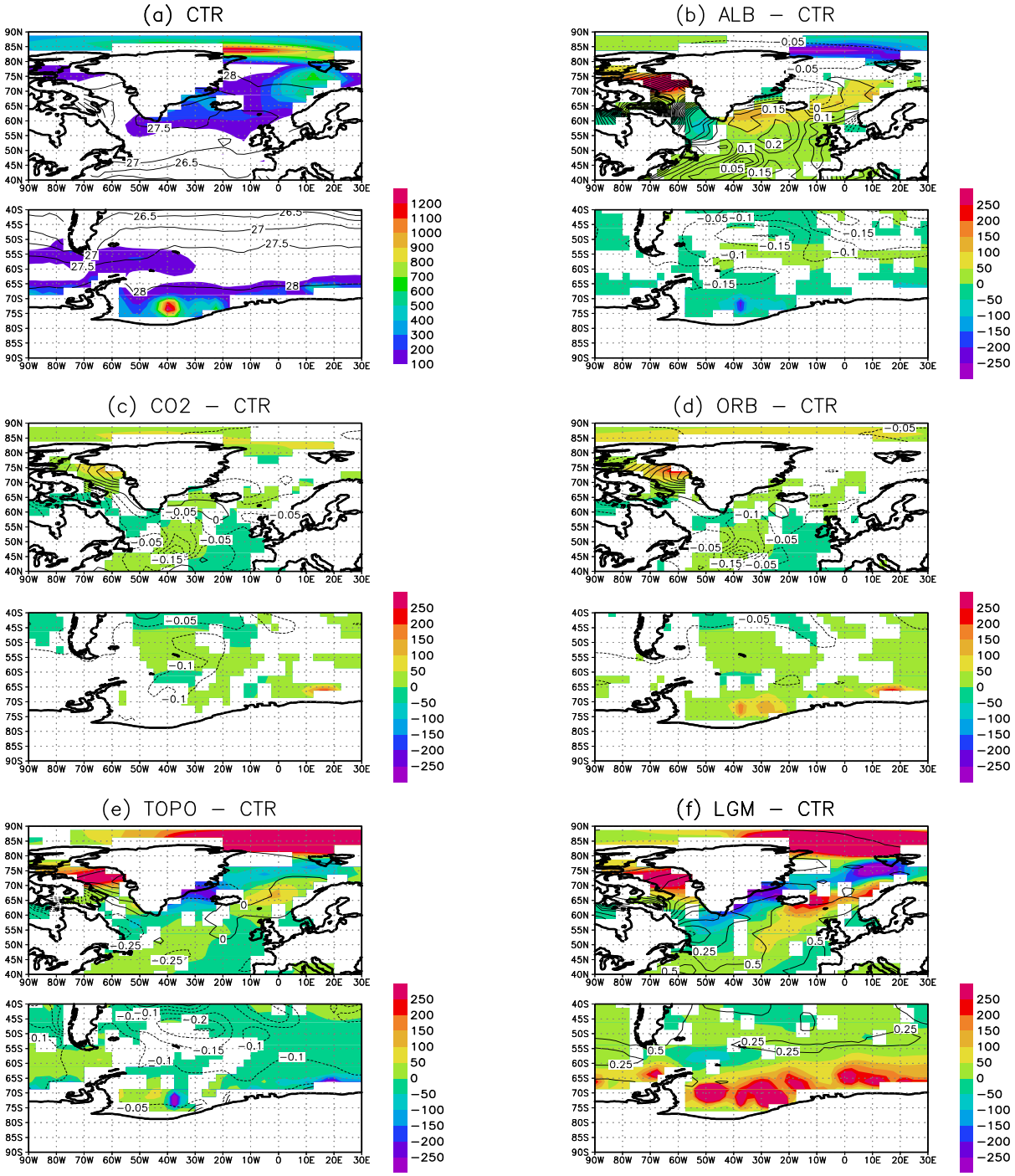

Fig. 4.16: *Simulated time mean convective layer depth (shaded) [m] and surface density - 1000 (contour) [kg/m^3]. Northern Hemisphere (upper) and Southern Hemisphere (lower), (a) CTR (b) differences between ALB-CTR (c) CO2-CTR (d) ORB-CTR (e) TOPO-CTR (f) LGM-CTR. Shaded areas are statistically significant at 95 % level based on calculations of student's t-test with 300 degrees of freedom.*

the coupled model (ECBilt-Clio) has an improved representation of convection sites. The simulated sites of deep water formation in the ECBilt-Clio version 2 used here are east of Greenland, and south of Iceland. In the SH, in agreement with other modeling studies, the Weddell Sea is an important convective region, supporting the formation of Antarctica Bottom Water (AABW). The changes of the CLD in ALB show a substantial deepening of the convective layer in the Labrador and GIN Seas and a shoaling in the Arctic Ocean (Fig. 4.16b). The increase in convection in the North Atlantic seems to result from the drop in SST which over compensates the reduced salinity contribution to the surface density. Deepening of CLD in the Nordic Seas is due to an increase of surface density. North of 80°N substantial changes of CLD are clearly seen which are due to glacial topographic forcing (Fig. 4.16e). The CLD and surface density changes in CO2 and ORB are marginal and shall be neglected here.

The LGM is characterised by a substantial increase in the CLD and density in the major sites of model deep water formation (Fig. 4.16f). Moreover, LGM also reveals a southward migration of the maximum of CLD in the NH. This southward displacement of the sites of convection has consequences for the structure of the North Atlantic THC. It is consistent with other *LGM* modeling studies and paleoceanographic data *(Hewitt et al. 2001; Sarnthein et al. 1995)*. Glacial albedo and ice sheet topography changes are largely responsible for the simulated LGM CLD and density anomalies, in particular in the NH. In the SH, however, the pronounced deepening of the CLD is not found in the individual sensitivity runs. This feature is a result of an increase of brine rejection linked to sea-ice changes and triggered by the lower SST.

4.7 Thermohaline Circulation

Changes of atmospheric and oceanic circulation, SST, SSS and sea-ice have a large impact on the processes driving deep water formation. The THC is a key element of the climate system, in particular in the NH, because it carries a substantial amount of heat and saline waters poleward. Climate changes associated with perturbations in the THC have been inferred from paleoclimatic records as well as from model simulations forced by increasing greenhouse gas concentrations.

Of particular scientific interest is the possibility of a THC weakening caused by warming and/or freshening of high latitude surface water due to greenhouse warming *(Stocker and Schmittner 1997; Manabe and Stoufer 1993)*. Both, the high latitude warming and an enhanced poleward transport of moisture in the atmosphere may contribute to the generation of a halocline in the formation regions of NADW. Thus, the climate during the *LGM*, which experienced large changes in the SST and SSS *(Schäfer-Neth and Paul 2003)*, is an interesting test case to study the stability properties of the THC.

The THC is driven primarily by horizontal density gradients, initiated by vertical density gradients resulting from deep convection at a few sites in the North Atlantic *(Marotzke 1997)* and the southern ocean. Interior vertical mixing plays also a crucial role in *pulling* the THC. Recent process studies (as part of WOCE - World Circulation Ocean Experiment) have confirmed that such mixing is highly localised in the deep ocean *(Munk and Wunsch 1998, Polzin et al. 1997)*. Furthermore, modeling studies

(Timmermann et al. 2004b; Oka et al. 2001; Schiller et al. 1997) revealed the importance of wind forcing for the establishment of large scale density gradients and hence, the THC.

Surface conditions in the North Pacific and Indian ocean do not favour deep convection. In the North Pacific surface waters are cold, like in the North Atlantic, but the waters are not salty enough to sink to the deep ocean. In the Indian Ocean, the waters are too warm at the surface to allow deep convection.

Figure 4.17 shows the simulated maximum of the meridional streamfunction, measuring the strength of the NADW and AABW. AABW formation is quantified in terms of the northward meridional mass transport at 20°S. Compared to reality, the ECBilt-Clio overestimates the strength of the NADW. The simulated transport associated with the NADW formation (35 Sv) is twice as strong as inferred from observations (18 Sv) *(Talley et al. 2003; Hall and Bryden 1982)*. The overestimation of NADW formation is a result of higher out polar/polar surface salinity, originating from unrealistically large values for brine rejection due to an overestimation of the sea-ice volume. It must be noted, however, that discrepancies associated with the strength of the NADW have been found in coupled global models of different complexity, as discussed by *IPCC (2001)* and presented here in Table 4.2. The Table clearly shows a large uncertainties in the simulated NADW strength between the models. In the SH, ECBilt-Clio simulates the amount of deep water formation more realistically (Table 4.3). The maximum meridional overturning in the SH as simulated by the CTR run attains values of about 37 Sv (Fig. 4.3), which is comparable to the *MacDonald (1998)* estimate of 36 Sv, but it is larger than the 22 Sv estimated by *Ganachaud and Wunsch (2000)* and *Talley et al. (2003)*.

Model Name	NADW (Sv)
ECBilt-Clio	34.3
CSM1	26.1
ECHAM3/LSG	28.1
ECHAM1/LSG	30.0
NCAR1	35.8
GFDL-R15	15.0
HadCM3	18.1
MRI2	17.0

Tab. 4.2: *Simulated NADW in different models [Sv].*

In the CTR simulation, the maximum meridional overturning in both hemispheres formed at regions with surface density higher than 1027.5 kgm^{-3} and CLD deeper than 700 m (Fig. 4.16a). Comparing the simulated NADW and the AABW in the sensitivity runs to the CTR, there is a clear increase (decrease) of the NADW (AABW). However, simulated changes of these quantities in ORB and CO2 are much smaller than in TOPO and ALB (Fig. 4.17a,b). TOPO shows stronger (weaker) NADW (AABW) than the ALB, despite smaller CLD anomalies. This feature is likely a result of a large amount of deep water formed north of 80°N in TOPO, due to the salinity changes under seasonal

LCDW (Sv)	Source
37.1	ECBilt-Clio
36.0	MacDonald (1998)
22.0	Ganachaud and Wunsch (2000)
48.0	Schmitz (1995)
50.0	Sloyan and Rintoul (2001)
22.0	Talley et al. (2003)

Tab. 4.3: *Simulated (ECBilt-Clio) and estimated Lower Circumpolar Deep water (LCDW) [Sv].*

sea-ice (see Fig 4.16e). Meanwhile, recent studies suggest that the SH climate changes may lead those of the NH *(Shin et al. 2003b; Blunier and Brook 2001). Broecker (1998, 2000)* proposed the bipolar seesaw, as a possible mechanism for SH control a NADW formation. The weaker AABW in TOPO favors an enhancement of the NADW due to a reduction of oceanic vertical stability linked to a reduced intrusion of deep dense water into the North Atlantic. A similar mechanism has been suggested by *Shin et al. (2003b).*

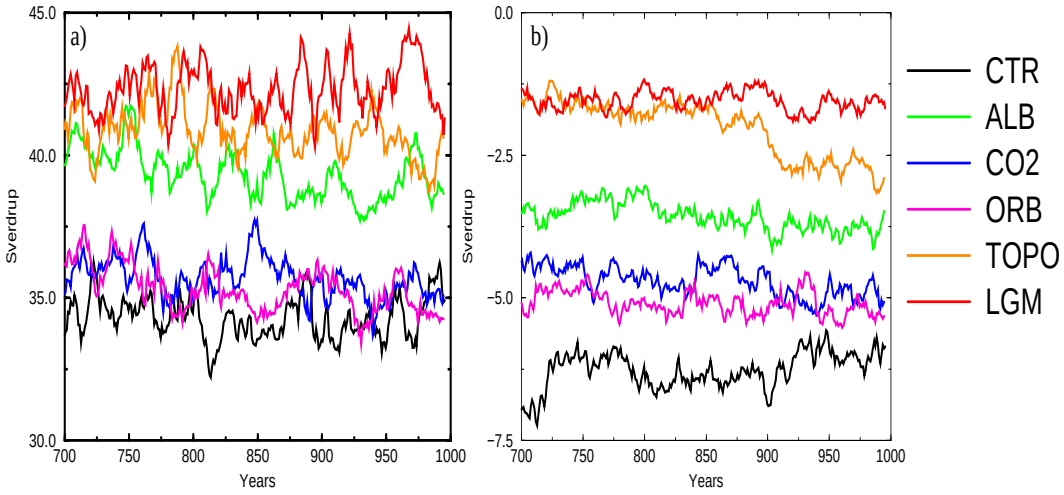

Fig. 4.17: *Time averaged annual mean maximum meridional overturning [Sv] for the LGM experiments. (a) NADW (b) AABW exported northward in Atlantic at 20° S.*

As proposed by *Schmitt et al. (1989)* and *Speer and Tziperman (1992)*, surface density anomalies (a combination of the thermal and the haline density anomalies) can generate thermohaline circulation changes. In order to diagnose the thermal and haline contributions to the density changes in LGM, the thermal and haline density flux ($kgm^{-2}s^{-1}$) is computed. The surface density flux is defined as *Schmitt et al. (1989)*,

$$F_\rho = \alpha F_t + \beta F_S = -\alpha \frac{Q}{C_P} + \beta\rho \frac{(E-P-R-I)S}{1-S}, \tag{4.3}$$

with the thermal expansion ($\alpha = -\frac{1}{\rho}\frac{\partial \rho}{\partial T}\mid_{p,S}$) and the haline contraction coefficient ($\beta = \frac{1}{\rho}\frac{\partial \rho}{\partial S}\mid_{p,T}$). In these expressions, $C_P, \rho_{(S,T)}, p, T$ and S are specific heat, density, pressure and sea surface temperature and salinity, respectively. Q, E, P, R and I represent net heat flux, evaporation, precipitation, runoff and water flux by sea-ice melting and growth, respectively. Figure 4.18 shows the surface density flux for CTR and the anomalies between the LGM and CTR. The two regions of strongest density gain are in the western North Atlantic, where cold and dry continental air masses blow onto relatively warm waters of the Gulf Stream and North Atlantic Current. The second region of density gain is in the Nordic Seas, where the model experiences a negative net heat flux associated to strong cooling of surface waters. ECBilt-Clio simulates positive thermal density flux in the tropical region off the east coast of the North America, while *Schmitt et al. (1989)* found a negative thermal density flux in this area. The contribution of the haline density flux to the total density is much smaller. The areas of density loss around the equator correspond to expected areas of heat gain and precipitation excess linked to the ITCZ.

On a basin-scale, similar findings were reported by previous studies *(Shin et al 2003; Schmitt et al. 1989)*. As argued by *Schmitt et al. (1989)* the salinity may dominate the density flux at the ice/water interface, but it does not dominate high latitude open-ocean fluxes.

As for present-day climate, the simulated NADW formation in the LGM is also controlled by the thermal density flux. Due to the stronger glacial cold advection over the North Atlantic, the thermal density flux anomalies (Fig. 4.18d) generate substantial changes in the surface density and subsequently in the CLD. Cold glacial winds increase the vertical air-sea temperature contrast and thus the loss of heat from the ocean to the atmosphere, which leads to strong convective mixing and an enhancement of the NADW cell in the LGM. The topographic and albedo forcing are crucial for this enhancement, through the related changes in the thermal density flux (not shown). Paleoceanographic data *(McCave et al. 1995; Veum et al. 1992)* and other *LGM* model simulations *(Hewitt et al. 2001; Kitoh et al. 2001)*, support the possibility of a stronger NADW, as simulated here. The changes in the haline density flux (Fig. 4.18e), however, tend to reduce the convection strength in the Nordic Seas and along the east coast of Greenland. This feature results partially from an increase in snowfall and precipitation associated with an enhancement and northward shift of the glacial North Atlantic storm track (see Fig. 4.13b). The total (thermal+haline) density flux anomalies are dominated by the changes in the thermal flux. Haline flux anomalies are most important to the east of Greenland and the Nordic Seas.

The findings discussed here are very similar to those obtained by *Shin et al. (2003)*. However, using the CCSM LGM model simulation *Shin et al. (2003)* found a reduction in the NADW formation, which they attributed to the increase in the vertical oceanic stability due to an enhanced intrusion of AABW into the North Atlantic. In the LGM experiment, the total maximum northward overturning in the SH is enhanced, but it is reduced in the southern Atlantic at 20°S (Fig. 4.17b). This is quite an unexpected

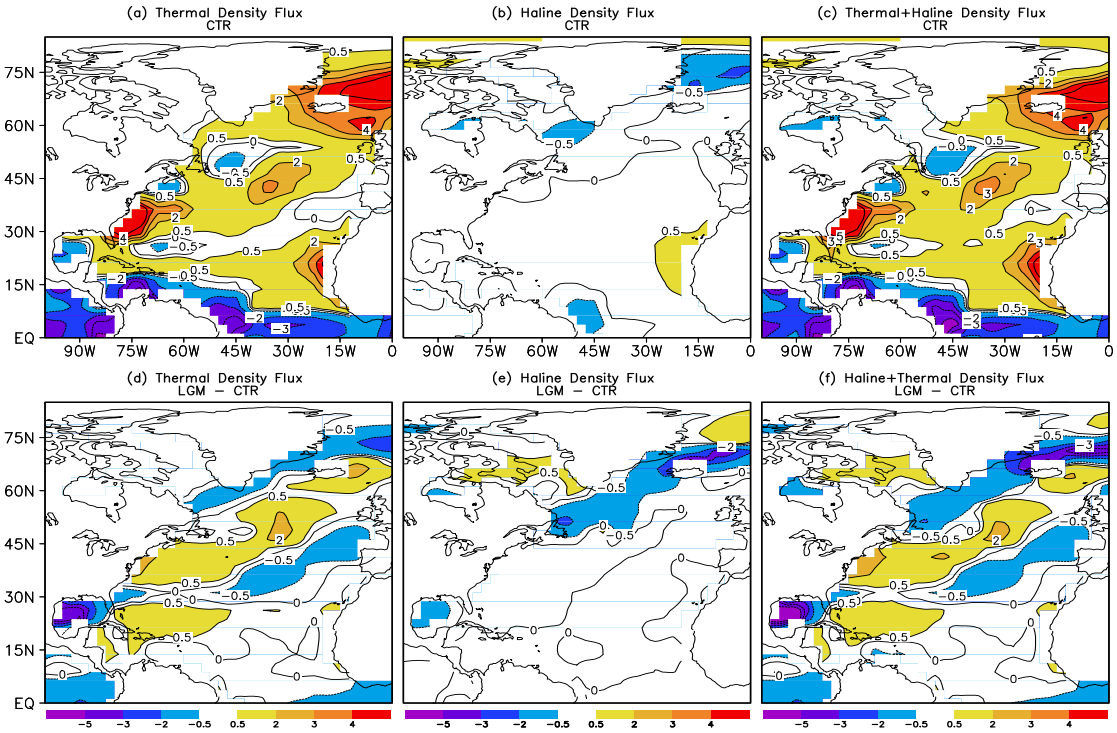

Fig. 4.18: *Time averaged annual density flux in CTR* $[10^{-6} \times kgm^{-2}s^{-1}]$*. (a) thermal contribution, (b) haline contribution and (c) thermal+haline. (d), (e) and (f) the same as a,b,c but for the differences LGM-CTR.*

results, since the CLD and density increase in the southern Atlantic in the LGM. More studies are necessary to better understand the interaction between the AABW and NADW, as well as the dynamical and thermodynamical mechanisms leading to the changes in both circulation systems.

4.8 Atmospheric and Oceanic Heat Transport

Radiative process continually act to cool the extra-tropics and warm the low latitudes of Earth, and it is only the poleward energy transport by the atmosphere and the oceans that establishes an equilibrium and prevents the tropics from warming up indefinitely *(Trenberth and Caron 2001; Miller and Russell 1989)*. As a result of the modified atmospheric and oceanic circulations during the *LGM*, substantial changes are expected to occur in the total heat transport. The total poleward heat transport of the atmosphere-ocean system in each latitudinal band is computed from the difference between the net shortwave radiation and the outgoing longwave radiative flux at the top of the atmosphere. It can be expressed as,

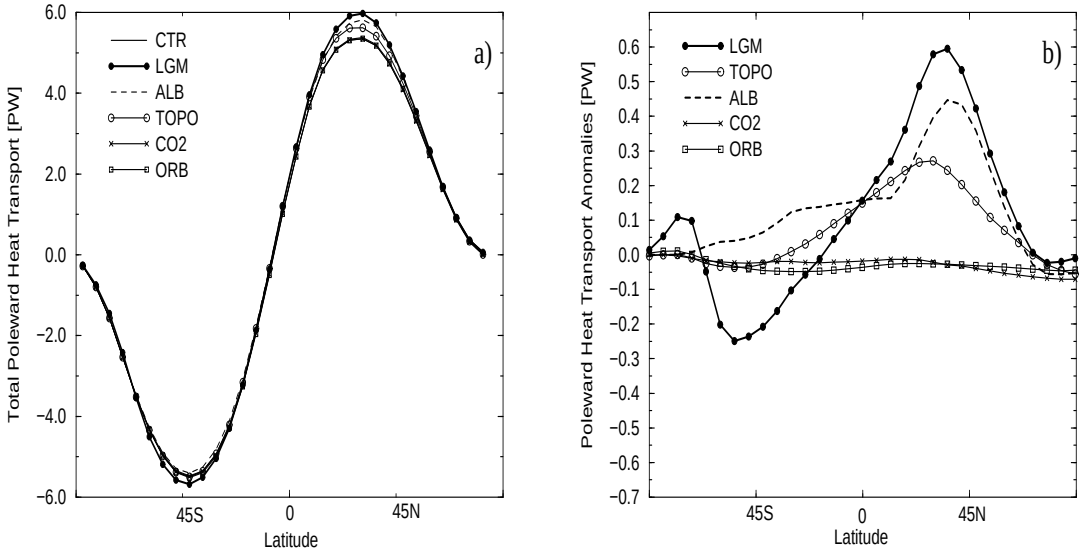

Fig. 4.19: *Time averaged annual heat transport [PW]. (a) Sensitivity experiments (b) Anomalies between the sensitivity experiments and CTR.*

$$H(\phi)_{total} = H_{ATM} + H_{OCE} = 2a^2\pi \int_{-\pi/2}^{\phi} (S_{TOA}(\phi)' - L_{TOA}(\phi)') \, .cos\phi' . d\phi' \qquad (4.4)$$

where, H_{total}, H_{ATM} and H_{OCE} are the total, atmospheric, and oceanic heat transport, respectively. a is the radius of the Earth, ϕ is the latitude, S_{TOA} is the zonally integrated net shortwave radiation, and L_{TOA} is the zonally integrated outgoing longwave radiative flux. Both fluxes are computed at the top of the atmosphere.

The simulated H_{total} in the CTR simulation is comparable to calculations which are based on data *(Trenberth and Caron 2001; Peixoto and Oort 1992)*. The maximum poleward heat transport appears in both hemisphere around 40°N and 40°S and attains maximum values of 5.2 PW ($PW = 10^{15}W$). In the sensitivity runs there is no change in the latitude at which the maximum northward and southward transport occurs (Fig. 4.19a). Figure 4.19b shows the H_{total} anomalies between the sensitivity experiments and CTR. It can be clearly seen that changes in atmospheric CO_2 concentration and in the orbital forcing change the heat transport only marginally. These boundary conditions generate a weak increase (decrease) in the heat transport in the SH (NH). Modified topography and albedo, however, are associated with significant changes in H_{total} (Fig. 4.19b). The topographic effect is evident north of 30°S with the maximum around 30°N. Although in TOPO the northward oceanic heat transport at 30°S increases in the Atlantic by about 0.1 PW (Table 4.3) this is not reproduced by the H_{total} anomalies. Thus, at this latitude belt the atmospheric and oceanic heat transport cancel each other out or the heat transport in the Indian/Pacific sector opposes the Atlantic counterpart.

In ALB experiment the contribution of the oceanic heat transport anomalies at 30°S in Atlantic to the H_{total} anomalies is very small (Table 4.3). The reduced southward H_{total} in ALB is mainly due to the weaker atmospheric heat transport. On the

EXP-CTR	$\Delta_{H_{OCE}}$
CTR = 0.32PW	-
Δ_{TOPO}	0.10
Δ_{ALB}	0.01
Δ_{CO2}	0.01
Δ_{ORB}	0.0
Δ_{LGM}	0.14

Tab. 4.4: *Northward oceanic heat Transport anomalies at 30°S in the Atlantic [PW]. Δ denotes anomalies between the sensitivity experiments and CTR.*

other hand, the northward transport in the NH as simulated by ALB increases due to the enhanced meridional overturning in the ocean and the steeper radiation gradient between 20°N-50°N (Fig. 4.20b). In the NH the H_{total} anomalies in TOPO are similar to the anomalies in the ALB, but they have smaller magnitudes (Fig. 4.19b).

The poleward H_{total} as simulated by LGM increases in both hemisphere in comparison to CTR experiment (Fig. 4.19b). Compared to the ALB and TOPO, the LGM needs more heat at high latitudes because it experiences much stronger extra-tropical cooling (Fig. 4.4f). The increased H_{total} in the LGM can be in part attributed to the steeper thermal contrast between tropical and extra-tropical regions. As shown in the Table 4.3, the northward heat transport in the South Atlantic increases by 0.14 PW which subsequently reduces the southward H_{total} and H_{OCE}, which in turn, enforces the SH cooling in the LGM. However, the increased transient eddy activity in the SH, more than compensate the reduced poleward oceanic heat transport (see Fig. 3.14f, Fig. 4.19b).

The LGM changes of H_{total} in the NH are also associated with changes in the meridional overturning circulation (see Fig. 4.17). The oceanic poleward heat transport in the Atlantic is mainly driven by the meridional overturning circulation cell, with northward flowing warm surface waters in the western boundary current and a southward flowing cold deep waters in the deep western boundary. The current contribution from the direct horizontal circulation is negligible (0.06 PW southward) *(Bryden 1993)*. In the Pacific the situation is different: There, the meridional heat transport is driven by the horizontal wind-driven circulation. It is important to note that in the LGM experiment the mass transport in the Kuroshio area is reduced and thereby its associated heat transport. For the Atlantic, *Böning et al. (1996)* derived a near linear relationship between the overturning rate and the total heat transport at 25°N from a set of experiments using a modified version of the Modular Ocean Model (MOM). It is suggested that for every 2 Sv gain in the overturning rate, the heat transport across 25°N increases by approximately 0.1 PW. Since in the LGM simulation the overturning increases by 8 Sv (see Fig. 4.17b) and the H_{total} by 0.6 PW (Fig. 4.19b), one would expect an increase in the oceanic heat transport in the North Atlantic by about 0.4 PW. Thus, around 0.2 PW of H_{total} must result from changes in the Indian-Pacific sector or/and from the atmospheric circulation. Further investigations have shown that the contribution from the horizontal gyre circulation in some models is not negligible. *He-*

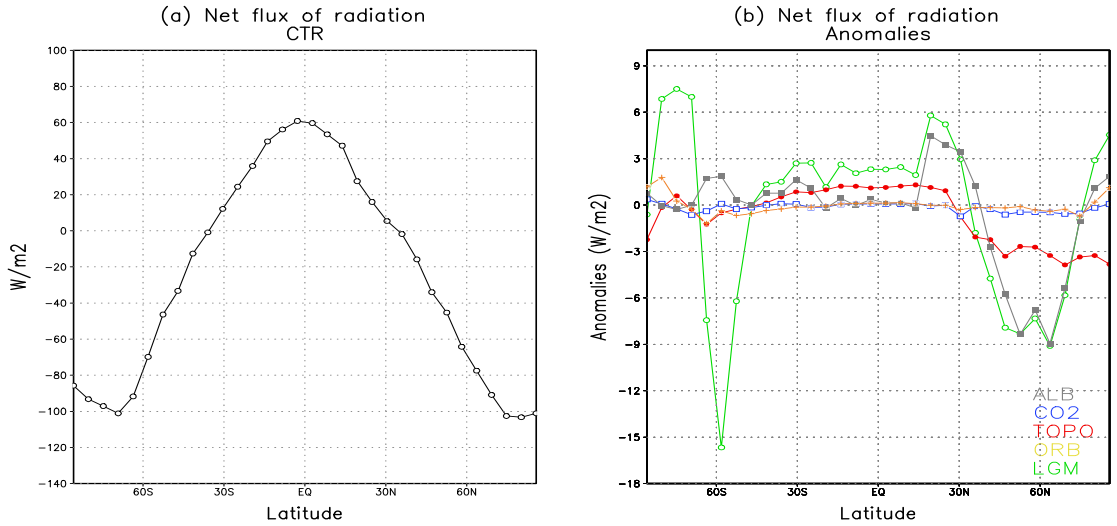

Fig. 4.20: *Time averaged annual mean net flux of zonally averaged radiation at the top of the atmosphere [Wm^{-2}]. CTR (a) anomalies between the sensitivity experiments and CTR (b).*

witt et al. (2001) studying a simulated relatively warm North Atlantic during the *LGM* argued that the increased heat transport in mid-latitudes was in part a consequence of a stronger simulated subpolar gyre.

4.9 Summary

In this chapter the simulated oceanic changes for the glacial sensitivity experiments have been investigated. As previously found for the *atmospheric* circulation, the changes of topography and land albedo play also the most important role in driving glacial *oceanic* changes. The simulated SST anomalies in LGM are quite similar to the CLIMAP reconstruction in the Pacific area and similar the GLAMAP *(Schäfer-Neth and Paul 2003)* reconstruction in the North Atlantic. Compared to pre-industrial conditions LGM exhibits a warming in the northeastern Pacific and an overall cooling in the Kuroshio area and the Atlantic. Both, the southward extension of the sea-ice margin and enhanced cold air advection from the Laurentide ice sheet play an important role in cooling the North Atlantic, whereas the reduced wind stress curl is responsible for the cooling in the Kuroshio area. In the equatorial Pacific, on the other hand, the lower SST results from a strengthening of the tropical/subtropical cell triggered by enhanced tropical-subtropical trade winds. Moreover, *Broecker (1995a)* argued that the reduced water vapour and CO_2 and consequently the weaker greenhouse capacity of atmosphere also plays an important role in triggering glacial oceanic cooling. This has been confirmed by *Timmermann et al. (2004)*.

The SST changes in the North Pacific are primarily driven by topographically in-

duced modifications of the large-scale atmospheric circulation. The anomalous stationary wave patterns in turn lead to a reduction of latent and sensible ocean cooling in the subtropical North Pacific. Furthermore, a reduced wind stress curl over the Kuroshio area slows down the subtropical and subpolar gyres, as diagnosed from the Sverdrup transport relationship (Fig. 4.8). As a consequence, the western North Pacific cools down whereas the northeastern Pacific warms up. Another mechanism that contributes to the North Pacific warming is based on remote tropical forcing associated with a permanent glacial La-Niña-type pattern *(Timmermann et al. 2004)*. It is well known that under present-day conditions, a La Niña event induces northeastern Pacific warming due to changes of latent and sensible heat fluxes *(Lau and Nath 1996)*. Hence, in addition to the effect of the upstream blocking situation on SSTs, there is a tropical teleconnection triggered by the La Niña state, which reinforces the warming in the North Pacific. Due to the low climate sensitivity of our coupled model to the reduced atmospheric CO_2, its associated radiative forcing can not compensate for this warming, as in other *LGM* simulations *(Shin et al. 2003; Bush and Philander 2001)*.

In the equatorial Pacific, ECBilt-Clio simulates SST anomalies of about 2-3 degrees which is 1-1.5°C lower than in the CLIMAP reconstruction. This cooling can be traced back to topographically induced changes in the upper level momentum flux convergence which generates a secondary circulation cell with ascending motion to the south of the convergence and descending motion to the north of it (Fig. 4.7b) *(Kuo 1956)*. This anomalous vertical circulation enhances the meridional pressure gradient and subsequently leads to stronger trade winds according to the geostrophic relation. Thereby, stronger trade winds near 10°-20°N enhance the strength of the subtropical cell due to Ekman transport which in turn intensifies the equatorial upwelling leading to the equatorial cooling. Based on the sensitivity experiments anomalies, one can argue that two other processes are important in controlling oceanic surface temperature i.e. the weaker greenhouse capacity of the dryer atmosphere and the local radiative forcing due to reduced atmospheric CO_2 concentration. Nevertheless, compared to the ocean dynamical changes these forcing mechanisms seem to play a secondary role.

As discussed by *Timmermann et al. (2004)*, a climatic comparison between simulated northeastern/equatorial Pacific SST anomalies and paleodata can be problematic since there are very few data which can be regarded as reliable SST proxies *(see Crowley 2000)*. For example, sediments cores from Hawaiian Islands may be contaminated by the Island wake effect *(Xie et al. 2001)* due to changes of the trade winds, which pushes warm western Pacific water into the area of the wake where the sediment cores were sampled. Thus, it remains unclear whether Hawai´ian SST proxies really represent temperatures of the open central Pacific. In the North Atlantic, however, the comparison between modeling results and paleodata is less problematic in particular after completing the GLAMAP reconstruction. A comparison between the simulated LGM SSTs anomaly and the GLAMAP reconstruction reveals that the LGM experiment has a warm bias in the North Atlantic. This may be due to the fact that the ECBilt-Clio simulation neglects background ablation from the ice sheets *(Marshall and Clark 1999)*, which can have an influence on the strength of the thermohaline circulation, and hence on the SST.

In addition to a 1 psu offset, the simulated salinity changes in the sensitivity ex-

periments show an overall freshening in the North Atlantic. Comparison among the sensitivity experiments shows that the salinity anomalies which result due to the reduced atmospheric CO_2 concentration are marginal. This agrees with the modeling results of *Shin et al. (2003)*. The southward glacial extension of the seasonal sea-ice margin in the North Atlantic does not result in positive SSS anomalies because a strong LGM storm track leads to increased freshwater fluxes which level off the brine effect. Except for the northeastern Atlantic, the simulated sea-ice extension in the LGM compares well with the GLAMAP reconstruction, as shown in Figure 4.15.

Changes of the atmospheric circulation, SST, SSS anomalies and changes of the characteristics of sea-ice have a large impact on surface density and CLD. Due to stronger cold air advection from the Laurentide ice sheet, the simulated changes in thermal density flux in the North Atlantic generate substantial changes in surface density and CLD. In the LGM experiment, the increase in CLD and density at the major sites of the deep water formation leads to an augment of the NADW formation rate, which is associated with a strengthening of the northward total heat transport by about 0.6 PW. The changes in ALB and TOPO are crucial for this enhancement through the changes in thermal density flux. Although the advection of warm surface waters associated with the anomalous cyclonic circulation in mid-latitudes (Fig. 4.3) may reduce the surface density in the sites of deep water formation, this effect is damped by the presence of a cold atmosphere which absorbs a large part of the heat. Paleoceanographic data *(McCave et al. 1995; Veum et al. 1992)* and other *LGM* model simulations *(Hewitt et al. 2001; Kitoh et al. 2001)* support the possibility of a stronger thermohaline circulation as simulated here. Although, other evidence based on radiocarbon analyses and other paleodata sources suggests that during the *LGM* the THC was considerably weaker than today *(Lea and Boyle 1990; Broecker and Denton 1989; Duplessy et al. 1988)*. It is important to note that it is not clear whether the thermohaline circulation was completely resumed at the time of the *LGM*, since the *LGM* occurred about 2000-3000 years after the major meltwater pulse Heinrich II.

5. CONCLUSION AND OUTLOOK

"Whether or not nature behaves according to law depends entirely upon whether we succeed in writing laws that describe its behaviour"

Goodman

The aim of this thesis was to explore and understand some major climate mechanisms responsible for atmospheric and oceanic changes during the *LGM* (21,000 years ago). The study is based on a series of *multi-millennial* coupled model simulations employing for the first time the coupled global-atmosphere-sea ice model of intermediate complexity, ECBilt-Clio. In order to study the *LGM* climate mechanisms, 17 experiments were performed (Table 2.4) which in total corresponds to 21,600 model years. In the introduction of the thesis, I raised several questions that shall be discussed in the light of the ECBilt-Clio results.

(1) What is the impact of the glacial boundary conditions on changes of the atmospheric and oceanic circulations?

The findings here confirm previous results obtained by *LGM* simulations: The topographic forcing excerts a strong influence on the glacial wintertime atmospheric circulation in the northern hemisphere *(e.g., Cook and Held 1988; Rind 1987)*. As discussed in Chapter 3, large-scale atmospheric flow is reorganized due to changes of the zonal mean circulation and the transient eddy activity associated to the modified boundary conditions. Different aspects of this reorganisation can be traced back to the effect of the individual boundary condition changes during the *LGM*. Analyses of the sensitivity experiments show that the presence of the *LGM* ice sheets and changes in land albedo play a crucial role in forcing *LGM* climate anomalies. When averaged globally, the prescribed changes of albedo are associated with the largest radiative forcing and the strongest tendency of cooling as compared to the changes resulting from the other boundary conditions. The modified orbital parameters and the reduced atmospheric CO_2 concentration favour a small reduction of global surface temperature during the *LGM*. However, their influence is most clearly manifested in the SH. The positive temperature anomalies as simulated in the SH by TOPO (1°C) are replaced by a strong cooling of up to 5°C in the LGM (Fig. 3.2). This cooling must result from a nonlinear interaction to the joint effect of the other boundary conditions. In some areas, TOPO and ALB generate opposite warming tendencies. For example, TOPO shows a warming over eastern Asia and the North Pacific, while ALB generates a cooling in these areas. In addition, as a result of the lower temperatures the dryer

atmosphere also plays an important role to enhance the overall global cooling due to the weaker greenhouse capacity. The topographic and albedo forcing are also crucial to modify the large-scale stationary wave pattern in the atmosphere during the *LGM*.

Changes of the stationary wave pattern during DJF and the associated surface temperature anomalies play an important role in changing the baroclinic structure of the glacial atmosphere. The analyses of σ_{BI} (baroclinic instability) revealed that glacial topographic changes intensify baroclinic instability over North America. Over Scandinavia, however, the reduction of the vertical wind shear due to the presence of the Fennoscandian ice sheet decreases σ_{BI}. In addition, the weaker meridional thermal gradient over the North Pacific associated with the topographic changes reduces the synoptic transient wave activity and the meridional temperature flux in the atmosphere. In this area, the reduced heat transport carried by the transient synoptic eddies enhances baroclinicity and operates as a negative feedback for the Pacific storm track activity. Furthermore, the reduction of the zonally averaged meridional momentum flux divergence of the synoptic disturbances leads to an intensification of the zonal mean upper level westerlies and an associated increase of the storm track activity due to barotropic and baroclinic instabilities. Eddy-mean flow interactions serve as a negative feedback for the zonally averaged mean flow and its transient eddy activity. The analyses of the eddy-mean-flow interactions showed that positive barotropic conversion and baroclinic production rates over the Laurentide ice sheets and the far eastern North Pacific have the tendency to decelerate the westerlies, thereby amplifying the stationary wave changes triggered by topographic forcing. In the North Atlantic area, the situation is more complex, as the downstream topographic low of the Laurentide ice sheet interacts with the upstream high of the Scandinavian ice sheet, leading to a particular flow situation over the North Atlantic. It is characterised by an intensification of transient eddy kinetic energy over Labrador Sea/Nordic Seas and a weaker transient eddy kinetic energy over the North Atlantic. These changes are consistent with the diagnosed eddy heat transport and the Eady growth rate (baroclinic instability). Furthermore, near the sea-ice margins the albedo and radiative forcing effects are very strong, creating substantial cooling due to the sea-ice albedo feedback. This cooling is further enhanced by the topographically-induced heat flux and ocean dynamics *(Timmermann et al. 2004)*.

(2) Which mechanisms are responsible for glacial SST changes in the Pacific Ocean?

Atmospheric changes associated with the *LGM* boundary conditions have a large impact on the SSTs anomalies, as addressed in Chapter 4. The simulated SST anomalies in the LGM have quite some similarities with the CLIMAP reconstruction in the Pacific area and with the GLAMAP SST and sea-ice reconstruction in the North Atlantic (Fig. 4.4). Compared to pre-industrial conditions, the LGM simulates a warming in the northeastern Pacific and an overall cooling in the Kuroshio area and Atlantic. The LGM simulated equatorial Pacific SST anomalies during the *LGM* are about 1-1.5 degrees lower than in the CLIMAP reconstruction and more consistent with the results of *Lea and Slowey (1990)*. The SST changes in the North Pacific are primarily

driven by topographically induced modification of the large-scale atmospheric circulation. The anomalous stationary wave patterns lead to a reduction of latent and sensible ocean cooling in the subtropical Pacific. Furthermore, reduced wind stress curl over the Kuroshio area slows down the subtropical and subpolar gyres, as diagnosed from the Sverdrup transport relationship (Fig. 4.8). As a consequence, the western Pacific cools down whereas the northeastern Pacific warms up. The mechanism responsible for the SST anomalies in the equatorial and the North Pacific is shown in Figure 5.1. Another mechanism that contributes to the North Pacific warming is based on remote tropical forcing associated with a permanent La-Niña-type pattern. It is well known that under present-day conditions a La Niña event induces warming of the North Pacific area due to changes of the latent and sensible heat fluxes *(Lau and Nath 1996)*. Hence, in addition to the effect of the topographic upstream blocking situation, there is a tropical teleconnection (which is even simulated in our quasi-geostrophic model) triggered by the La Niña state, which reinforces the positive extra-tropical SST anomaly. Due to the relatively low climate sensitivity of our coupled model the reduced radiative forcing due to the CO_2 lowering can not compensate for this warming.

These changes in the SST have a direct impact on the precipitation patterns in the LGM. As a result of the permanent La Niña state the LGM exhibits negative precipitation anomalies in the equatorial Pacific, whereas positive anomalies are found in the northeastern Pacific which are associated with positive SST anomalies. The dryer equatorial Pacific/wetter northeastern Pacific pattern is consistent with a precipitation reconstruction inferred from lake level data *(Kohfeld and Harrison 2000)* (see Fig. 3.25). Most of the glacial snowfall anomalies in the NH are a result of the presence of the Laurentide and Fennoscandian ice sheets (Fig. 3.24c,e). The other glacial boundary conditions play a secondary role. In the LGM, a belt of increased snowfall can be seen around 60°S. The increase of snowfall over the ACC area is a nonlinear response to the joint effect of the *LGM* boundary conditions. The LGM exhibits dryer conditions in most of the tropics and extra-tropics (Figs. 3.24b,d,f) due to the decreased water content in the colder atmosphere (Fig. 3.6), as well as due to changes in the atmospheric circulation.

The strong air-sea interaction and the importance of the diabatic forcing for the atmospheric circulation during the *LGM*, makes an assessment and a model-data comparison particularly difficult. The reason is that different coupled atmosphere-ocean models generate different climate response for the *LGM*. The disagreement among the models is expected, given the uncertainty of future climate projections using state-of-the-art coupled general circulation models. Surprising, however, is that all of these *LGM* model simulations are considered to be consistent with reconstructed data. Obviously, this suggests that the uncertainty in the reconstructions is so large that it prevents to constrain which of the model simulations is most realistic. Or in other words, paleo modeling studies (including this) tend to show a comparison with those paleo-data which fit. Future research will hopefully narrow down the uncertainties of paleo data and those of climate model simulations for the *LGM* considerably. For the time being, we have to cope with the uncertainties still present.

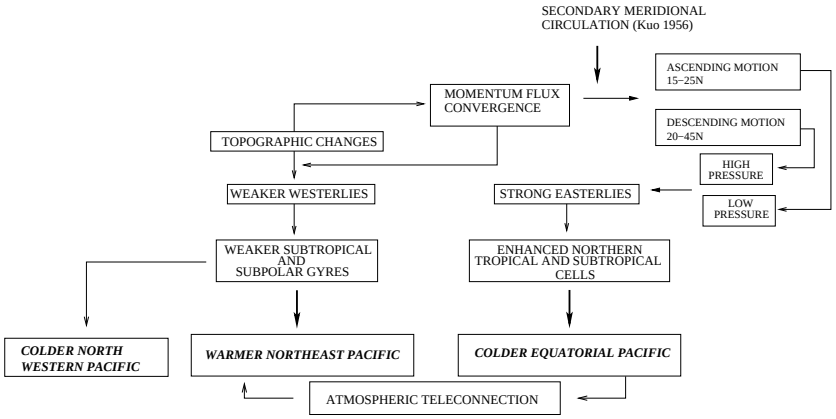

Fig. 5.1: *Control mechanism of the northern and equatorial Pacific surface temperature. After Timmermann et al. (2004).*

(2) How does the thermohaline circulation respond to glacial boundary conditions?

As a result of the changes in the oceanic convective layer depth and the surface density in the LGM experiment the rate of the NADW formation increases. The enhanced glacial NADW is accompanied by a substantial strengthening of the poleward oceanic heat transport in the North Atlantic which in turn reduces the SST in the SH, since less heat is transported southward. Comparing the simulated NADW and the AABW formation rate in the sensitivity runs to the CTR, it becomes evident that the deep water anomalies triggered by orbital forcing and reduced atmospheric CO_2 concentration are much smaller than in TOPO and ALB (Fig. 4.17a,b)

It is not clear from paleodata as to whether the THC was in an equilibrium state during the real *LGM* period, because it occurred 3,000 years after the transient meltwater pulse Heinrich II. In order to examine the atmospheric and oceanic response to a weakening of the THC under the LGM background forcing, sensitivity experiments were carried out (not shown here) by adding freshwater into the North Atlantic thereby mimicking an idealized Heinrich Event II. The freshwater experiments show that the NADW decreases almost linearly with the volume of freshwater added and it is accompanied by an increase in the AABW nearly simultaneously with the NADW reduction. This weaker North Atlantic meridional cell leads to reduced northward heat transport which in turn cools the Northern Hemisphere. Since heat is no longer exported northward the Southern Hemisphere warms up in particular in high-latitudes. This contributes to the so-called bipolar seesaw effect. The suppression of the NADW also drastically changes the atmospheric circulation (not shown). At 800 hPa a strong anomaly high pressure establishes over the North Atlantic/Europe while a low pressure anomaly can be found over the North America.

Some limitations of EMIC modeling approach pursued here, originate from the set-up of the atmospheric model, which is based on the quasi-geostrophic (QG) approximation and uses just three atmospheric layers. Strinctly speaking, the QG as-

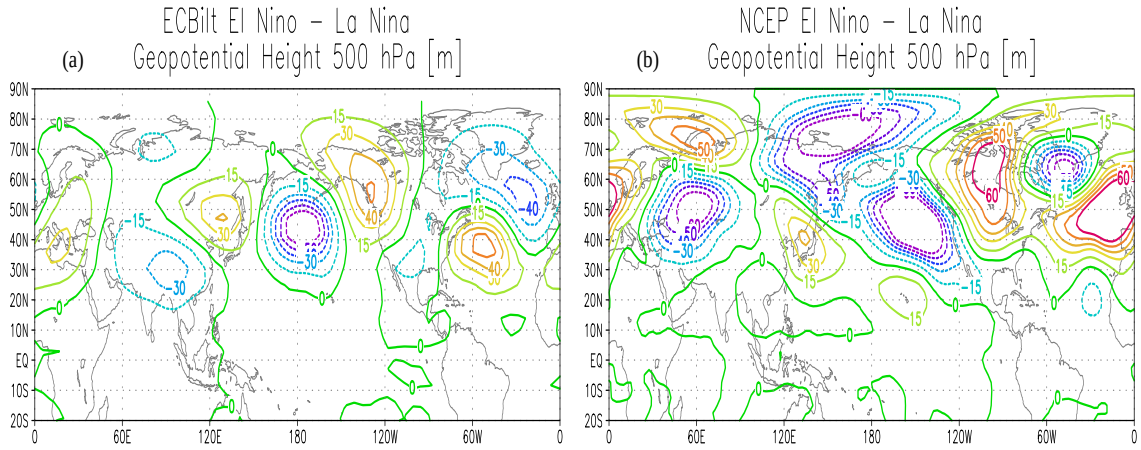

Fig. 5.2: *Eddy geopotential response [m] at 500hPa to an El Niño pattern with a Niño 3 amplitude 3-4°C. (a) ECBilt and (b) NCEP composite between El Niño and La Niño events.*

sumption holds only for small Rossby numbers ($Ro \ll 1$) and for small topographic gradients. Despite this theoretical limitation the atmospheric response e.g. to tropical SST anomalies is qualitatively well captured (Fig. 5.2). However, the amplitude of the response is diminished in comparison with high-resolution primitive equation models, which is mostly due to the low resolution of the atmospheric model, rather than due to the QG assumption. Furthermore, it was found that the presence of topography leads to an improved atmospheric circulation and stationary and transient wave activity with respect to a simulation which neglects orographic forcing (Fig. 5.3). Figure 5.3c shows that the presence of topography plays a crucial role in generating the low over northeastern Asia and the ridge over western North America. Hence, practically the model can reproduce much better both the tropical and topographic responses than the strict theoretical considerations suggest. It is important to note that compared to the NCEP Reanalysis (Fig. 5.3d), the amplitude of the simulated stationary waves is reduced by a factor of 2. The inclusion of the ice sheet topography (see Fig. 2.8b) in a three layer atmosphere (200, 500, 800 hPa) may be problematic. Compared with other coupled *LGM* simulations, however, the LGM experiment analysed here reveals large similarities with the results obtained from primitive equation multi-layer models. To be more specific: The simulated stationary wave anomalies induced by *LGM* forcing are qualitatively and quantitatively very similar to those obtained by *Kitoh et al. (2001)* using the MRI CGCM. The same holds for the simulated SST structure. The upstream high and downstream low features associated to the ice sheets also show good agreement with e.g., *Rind (1988, figure 22)* and *Broccoli and Manabe (1987, figure 11)*.

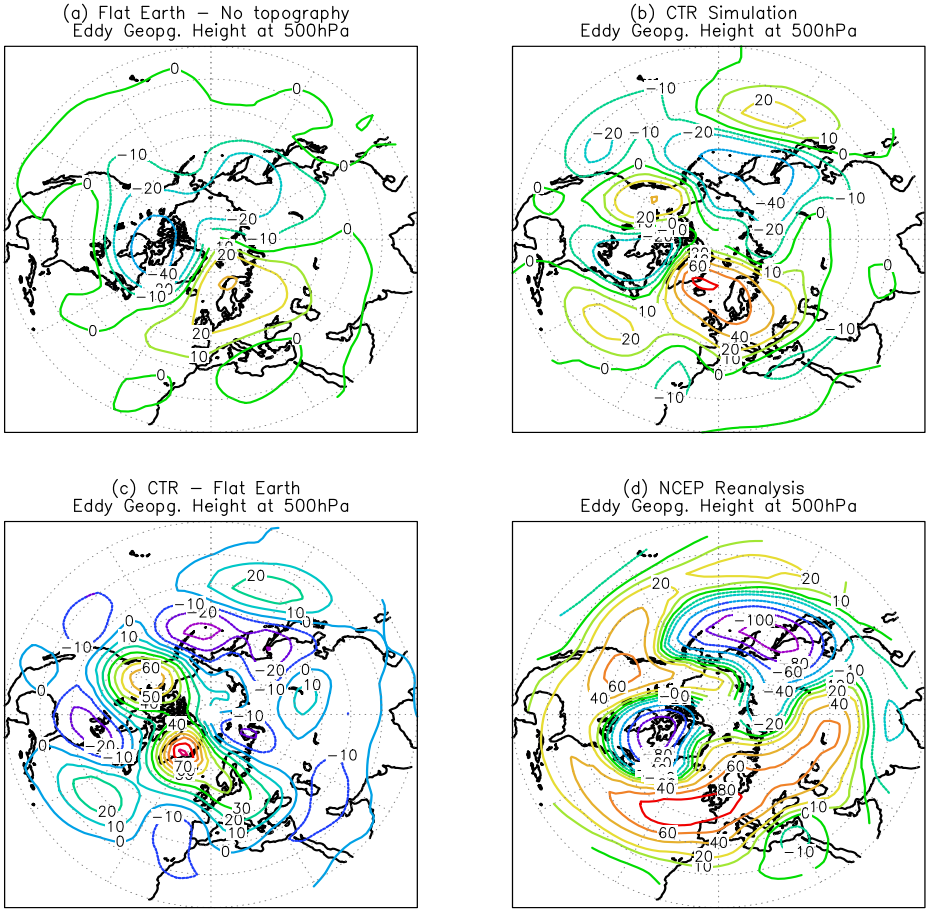

Fig. 5.3: *Time averaged annual mean eddy geopotential height at 500hPa [m]. Flat Earth (a), CTR (b), eddy geopotential anomalies between Flat Earth and CTR (c) and the eddy geopotential height in NCEP Reanalysis (d).*

Outlook

Several issues of glacial climates could not be addressed by this study. An in-depth analysis of the interaction between stationary and transient waves under glacial conditions would be very interesting. Furthermore, atmospheric circulation changes can be projected onto the leading atmospheric circulation regimes. According to *Palmer (1999)* and *Corti et al (1999)*, climate change manifests itself in significant changes of the probability of natural weather patterns. This hypothesis can be tested for LGM climate anomalies. In addition, a more in-depth analysis of the changes of the thermohaline circulation, the role of overflows, convection and wind-forcing under glacial conditions, would be another challenging exercise for future research.

In a recent EU project (MOTIF) similar experiments as the LGM experiment conducted here will be performed using state-of-the art CGCMs. Using these simulations it will be very interesting to assess how robust atmospheric and oceanic changes patterns are represented by different global coupled climate models. This will also reveal as to whether the simplifications made in our atmospheric model are justified or not.

The LGM experiments discussed in this thesis do not take into account the background ablation from the ice-sheets *(Marshall and Clarke 1999)* which is in the range of 0.1-0.3 Sv. This significant perturbation of the hydrological cycle may have severe consequences for the strength of the THC. In a series of sensitivity studies with ECBilt-Clio, this effect has been analysed. The results will be submitted to the Journal of Geophysical Research soon. In fact, the main conclusion is that without an active ice sheet model the strength of the glacial THC cannot be assessed properly using CGCMs.

The LGM experiments conducted here are also the basis for the simulation of Heinrich events by Uta Krebs. In her PhD thesis she will study the processes that lead to the recovery of the THC after a meltwater-induced collapse, as well as the role of air-sea interactions in setting up the bipolar seesaw. A new version of ECBilt-Clio is used in this study, which has more realistics meridional overturning in the North Atlantic.

Remote forcing of the glacial THC from the Southern Hemisphere, as suggested by *Weaver et al. (2003)* and *Knorr and Lohmann (2003)* is another hypothesis that shall be tested in near future using the ECBilt-Clio LGM model.

In essence, science is a perpetual search for an intelligent and integrated comprehension of the world we live in.

Cornelius Bernardus Van Neil

6. LIST OF REFERENCE

Adam, J., H. Faure, H. (1997) *Palaeovegetation maps of the Earth during the Last Glacial Maximum, and the early and mid Holocene: an aid to archaeological research. J. Arch. Sci, 24, 623-647.*

Alley, R.B. (2000) *Ice-core evidence of abrupt climate changes. Proceedings of the National Academy of Sciences USA 97: 1331-1334.*

An, S-I., Timmermann, A., Lin, F.F., Bejerano, L., Justino, F., Liu, Z., Tudlope, A.W. (2003) *Modeling evidence for enhanced ENSO variability during the Last Glacial Maximum. Submitted to Paleocenography.*

Anderson, D. M., Webb, R.S. (1994) *Ice-age tropics revisited, Nature, 367, 23-24.*

Andreasen, D., Ravelo, A.C. (1997) *Tropical Pacific Ocean thermocline depth reconstruction for the Last Glacial. Paleocenography, 12, 395-414.*

Barb, E., Rostek, F. Sonzogni, C. (1997) *Interhemispheric synchrony of the last deglaciation inferred from alkenone palaeothermometry. Nature, 385, 707-710.*

Barb, E., Arnold, M., Maurice, P., Duprat, J., Moyes, J., Duplessy, J.-C. (1987) *Retreat velocity of the North Atlantic polar front during the last deglaciation determined by ^{14}C accelerator mass spectrometry. Nature, 328, 791-794.*

Beck, J. W., Recy, J., Taylor, F., Edwards, R.L., Cabioch G. (1997) *Abrupt changes in early Holocene tropical sea surface temperature derived from coral records, Nature, 385, 705-707.*

Behl, R.J., Kennet, J.P. (1996) *Brief interstadial events in the Santa Barbara basin, NE Pacific, during the past 60 kyr. Nature, 379, 243-246.*

Berger, A. (1988) *Milankovitch theory and climate, Reviews of Geophysics, 26, 624-657.*

Bjornsson, H., Mysak, L.A. (2001) *Present-Day and Last Glacial Maximum Ocean Thermohaline Circulation in a zonally Averaged Coupled Ocean-Sea-Ice-Atmosphere Model. J. Climate, 14, 1422-1439.*

Blackmon, M.L. (1976) *A climatological spectral study of the 500hPa geopotential height for the northern Hemisphere. J. Atmos. Sci. 33:1607-1623.*

Blunier, T., Brook, E.J. (2001) *Timing of millennial-scale climate change in Antarctica and Greenland during the last glacial period. Science, 291, 109-112.*

Bond, G., Showers, W. Chezebiet, M., Lotti, M., Almasi, R., deMenocal, P., Priore, P., P. Cullen, Hajdas H.I., Bonani, G. (1997) *A pervasive Millennial-scale cycle in North Atlantic Holocene and glacial climates. Science, 278, 1257-1266.*

Bond, G.C., Lotti, R. (1995) *Iceberg discharges into the North Atlantic on millennial time-scales during the last glaciation, Science, v. 267, p. 1005-1010.*

Böning, C.W., Bryan, F.O., Holland, W.R. Döscher, R. (1996) *Deep-water formation and meridional overturning in a high-resolution model of the North Atlantic. J. Phys. Oceanogr., 26, 1142-1164.*

Bradley, R.S. (1999) *Paleoclimatology: Reconstructing Climates of the Quaternary. Academic Press, San Diego, 610pp.*

Broccoli, A. J. (2000) *Tropical cooling at the Last Glacial Maximum: An atmosphere-mixed layer ocean model simulation. J. Climate, 13(5), 951-976.*

Broccoli, A.J., Manabe, S. (1987) *The influence of continental ice, atmospheric CO_2, and land albedo on the climate of the last glacial maximum. Clim. Dyn., 1, 87-99.*

Broecker, W.S. (2000) *Was a change in thermohaline circulation responsible for the Little Ice Age? Proc. Nat. Acad. Sci., 97(4): 1339-1342.*

Broecker, W.S. (1998) *Paleocean circulation during the last deglaciation. A bipolar seesaw? Paleoceanography, 13, 119-121.*

Broecker, W.S. (1997) *Thermohaline circulation, the Achilles heel of our climate system: Will man-made CO2 upset the current balance? Science, 278, 1582-1588.*
Broecker, W.S. (1995a) *The glacial world according to Wally. Eldigio Press, New York, USA, pp 318.*
Broecker, W.S. (1995b) *Chaotic Climate. Scientific American, 273, Sci. Amer. 273:62-68.*
Broecker, W. S. (1994) *Massive iceberg discharges as triggers for global climate change, Nature, 372, 421.*
Broecker, W.S., Denton, G.H. (1989) *The role of ocean-atmosphere reorganizations in glacial cycles. Geochimica et Cosmochimica Acta 53:2465-2501*
Broecker, W.S., Peteet, D.M., Rind, D. (1985) *Does the ocean-atmosphere system have more than one mode of operation? Nature, 315, 21-26.*
Bromwich, D.H., Robask, F.M., Keen, R.A., Bolzan, J.F. (1993) *Modeled variations of precipitation over the Greenland ice sheet. J. Climate 6:1253-1268.*
Bryden, H.L. (1993) *Ocean heat transport across 24°N latitude. In: Interaction Between Global Climate Subsystems, The legacy of Hann (G.A. McBean, and M. Hantel, eds.). Geophysical Monographs, No.3/4, 5-6.*
Budyko, M.I., (1969) *The Effect of Solar Radiation Variations on the Climate of the Earth. Tellus, 21, 611-619.*
Bush, A. B. G., Philander, S. G. H. (1999) *The climate of the Last Glacial Maximum: Results from a coupled atmosphere-ocean general circulation model. J. Geophys. Res. D20, 24,509-24,525.*
Campin, J., Goosse, H. (1999) *A parametrisation of dense overflow in large-scale ocean models in z coordinate. Tellus, 51A, 412-430.*
Chang, K. M. E., Lee, S., Swanson, K. L. (2002) *Storm Track Dynamics. J. Atmos. Sci. 15:2163-2183.*
Claussen, M., Ganopolski A., Brovkin V., Gerstengarbe F.-W., Werner P. (2003) *Simulated Global-Scale Response of the Climate System to Dansgaard-Oeschger and Heinrich events. Climate Dynamics, 21: 361-370.*
Clement, A.C., Cane, M.A., Seager, R. (2001) *An orbitally driven tropical source for abrupt climate change. J. Climate, 14, 2369-2375.*
CLIMAP Project Members (1981) *Seasonal reconstruction of the Earth's surface of the last glacial maximum. Geol. Soc. Am. Map. Chart Ser. MC-36 1-18.*
Cook, K.H., Held, I. (1992) *The stationary Response to Large-Scale Orography in a General Circulation Model and Linear Model. J. Atm. Sci., 49, 6, 525-539.*
Cook, K.H., Held, I. (1988) *Stationary waves of the ice age climate. J. Climate, 1:807-819.*
Corti, S., Molteni, F., Palmer, T.N. (1999) *Signature of recent climate change in frequencies of natural atmospheric circulation regimes, Nature, 398, 799-802.*
Crowley, T. (2000) *CLIMAP SSTs re-revisited. Clim. Dyn, 16, 241-245.*
Crowley, T. (1995) *Ice age terrestrial carbon changes revisited. Global Biogeochemical Cycles, 9:377-389.*
Dansgaard, W., Johnsen, S.J., Clausen, H.B., Dahl-Jensen, D., Gundestrup, N.S., Hammer, C.U., Hvidberg, C.S., Steffensen, J.P., Sveinbjörnsdottir, J.E., Jouzel, J., Bond, G. (1993) *Evidence for general instability of past climate from a 250 kyr ice core. Nature, 364, 218-219.*
Dansgaard, W., White, J.W., Johnsen, S.J. (1989) *The abrupt termination of the Younger Dryas climate event. Nature, 339, 532-534.*
Dansgaard, W., Johnsen, S.J., Clausen, B., Dahl-Jensen, D., Gundestrup, N., Hammer, C.U., Oeschger, H. (1984) *North Atlantic climatic oscillations revealed by deep Greenland ice. In: Climate Processes and Climate Sensitivity. Hansen, J.E., Takahashi, T. (eds.) Geophys. Mono., 29, Amer. Geophys. Union, Washington D.C., pp. 288-298.*
daSilva, A., Young, A. C., Levitus, S. (1994) *"Atlas of surface marine data 1994, volume 1.: Algorithms and procedures.," Tech. Rep. 6, U.S. Department of Commerce, NOAA,NESDIS.*
Denton, G.H., Hughes, T. (1981) *The Last Great Ice Sheets (Wiley, New York).*
Dickson, R.R., Meincke, J., Malmberg, S.-A., Lee, A.J. (1998) *The ?Great Salinity Anomaly? in the northern North Atlantic 1968-1982. Prog. Oceanogr., 20, 103-151.*
Dong, B., Valdes, P. (2000) *Climates at the Last Glacial Maximum: Influence of Model Horizontal*

Resolution. J. Climate 13:1554-1573.

Dong, B., Valdes, P. (1998) *Simulation of the last glacial maximum climates using a general circulation model: Prescribed versus computed sea surface temperature. Clim. Dyn., 14:571-591.*

Duplessy, J.C., Shackleton, N.J., Fairbanks, R.J., Labeyrie, L., Oppo, D., Kallel, N., (1988) *Deepwater source variations during the last climatic cycle and their impact on the global deepwater circulation. Paleoceanography, 3, 343-360.*

Farrera, I., Harrison, S.P., Prentice, I.C., Ramstein, G., Guiot, J., Bartlein, P.J., Bonnefille, R., Bush, M., Cramer, W., von Grafenstein, U., Holmgren, K., Hooghiemstra, H., Hope, G., Jolly, D., Lauritzen, S.-E., Ono, Y., Pinot, S., Stute, M., Yu, G., (1999) *Tropical climates at the last glacial maximum: a new synthesis of terrestrial palaeoclimate data. I. Vegetation, lake-levels and geochemistry. Clim. Dyn., 15, 823-856.*

Fanning, A.F., Weaver, A.J. (1997) *Temporal-geographical meltwater influences on the North Atlantic conveyor: Implications for the Younger Dryas. Paleoceanogr., 12, 307-320.*

Ganachaud, A., Wunsch, C. (2000) *Improved estimates of global circulation, heat transport and mixing from hydrographic data. Nature, 408, 453-457.*

Ganopolski, A., Rahmstorf, S. (2001) *Simulation of rapid glacial climate changes in a coupled climate model. Nature, 409, 153-158.*

Gent, P., McWilliams, J. (1990) *Isopycnal mixing in ocean general circulation models. J. Phys. Oceanogr. 150-155.*

GrADS (Grid Analysis and Display System) Version 0.9. Copyright (c) 1988, 1989, 1990 *by Brian Doty (Center for Ocean-Land-Atmosphere Interactions , Department of Meteorology, University of Maryland, College Park, MD 20742).*

Grootes, P.M., Stuiver, M. (1997) *Oxygen 18/16 variability in Greenland snow and ice with 10-3 and 10-5 year time resolution. J. Geophys. Res. C102, 26455-26470.*

Guilderson, T.P., Fairbanks, R.G. and J.L. Rubenstone (1994) *Tropical temperature variations since 20,000 years ago: modulating interhemispheric climate change, Science, 263, 663-665.*

Hagelberg, T., Bond, G., deMenocal, P. (1994) *Milankovitch band forcing of sub-Milankovitch climate variability during the Pleistocene, Paleoceanography, 9, 545-558,*

Hall, N. M. J., Hoskins, B. J., Valdes, P., Senior, C. (1994) *Storm tracks in a high-resolution GCM with doubled carbon dioxide. Q.J.Meteorol. Soc., 128:1209-1230.*

Hall, M.M., Bryden, H.L. (1982) *Direct estimates of ocean heat transport. Deep Sea Res. 29, 339-359.*

Hansen, J.E., Sato, M., Ruedy, R. (1993) *How sensitivite is the world's climate? Nat Geogr Res Explor 9: 143-158.*

Haug, G.H., Hughen, K.A., Peterson, L.C., Sigman, D.M., Röhl, U. (2001) *Southward migration of the Intertropical Convergence Zone through the Holocene. Science 293, 1304-1308.*

Haug, G.H., Pedersen, T.F., Sigman, D.M., Calvert, S.E., Nielsen, B., Peterson, L. (1998) *Glacial/interglacial variations in production and nitrogen fixation in the Cariaco Basin during the last 580 ka. Paleoceanography 13, 5, 427-432.*

Heinrich, H. (1988) *Origin and consequences of cyclic ice rafting in the Northeast Atlantic Ocean during the past 130,000 years , Quaternary Research 29, p.143-152.*

Hellerman, S., Rosenstein, M. (1983) *Normal monthly wind stress over the world ocean with error estimates. J. Phys. Oceanogr., 13, 1093-1104.*

Herbert, T.D., Schuffert,J. D., Andreasen, D., Heusser, L., Lyle, M., Mix, A. Ravelo, A.C., Stott, L.D., Herguera, J.C. (2001) *Collapse of the California Current During Glacial Maxima Linked to Climate Change on Land. Science, 61-76.*

Hewitt, C., Broccoli, J.A., Mitchell, J.F.B., Stouffer, R.J. (2001) *A coupled model study of the last glacial maximum: Was part of the North Atlantic relatively warm? Geo. Res. Lett., 28, 1571-1574.*

Hewitt, C., Mitchell, J.F.B. (1997) *Radiative forcing and response of a GCM to ice age boundary conditions: cloud feedback and climate sensitivity. Clim. Dyn., 13,821-834.*

Hilmer, M., Lemke, P (2000) *On the decrease of Arctic sea ice volume. Geophy. Res. Let., 27, 3751-3754.*

Hodell, D.A., Curtis, J.H., Brenner, M. (1995) *Possible role of climate in the collapse of classic*

Maya civilisation. Nature, 375, 391-394.
Hoffert, M.I., Covey, C. (1992) *Deriving global climate sensitivity from palaeoclimate reconstructions. Nature, 360, 573-576.*
Holopainen, E. O., Rontu, L. and Lau, N.C. (1982) *The effect of large-scale transient eddies on the time-mean flow in the atmosphere. J. Atmos. Sci., 39, 1972-1984.*
Holton, J. (1972) *An introduction to dynamic meteorology. Academic Press, Inc. pps. 319.*
Hoskins, B.J., Valdes P., (1990) *On the existence of storm-tracks. J. Atmos. Sci., 47, 1854-1864.*
Hoskins, B.J., James I. N., White, G. H. (1983) *The shape, propagation and mean flow interaction of large scale weather system. J. Atmos. Sci., 40,1595-1612.*
Imbrie, J., Boyle, E.A., Clemens, S.C., Duffy, A., Howard, W.R., Kukla, G., Kutzbach, J., Martinson, D.G., McIntyre, A., Mix, A.C., Molfino, B., Morley, J.J., Peterson, L.C., Pisias, N.G., Prell, W.L., Raymo, M.E., Shackleton, N.J., Toggweiler, J.R. (1992) *On the structure and origin of major glaciation cycles, 1, Linear responses to Milankovitch forcing, Paleoceanography, 7, 701-738.*
Imbrie, J., Hays, J.D., Martinson, D.G., McIntyre, A., Mix, A.C., Morley, J.J., Pisias, N.G., Prell, W.L., Shackleton N.J.(1984) *The orbital theory of Pleistocene climate: Support from a revised chronology of the marine O record, in Milankovitch and Climate, Part 1, edited by Berger, A.L. et al., D. Reidel, Norwell, Mass, pp. 269-305.*
IPCC: Climate Change 2001 (2001) *. The scientific basis. Eds. J. T. Houghton, Y. Ding, D. Griggs, M. Noguer, P. Van der Linden, X. Dai, K. Maskell, C. A. Jonhson. Cambridge Univ. Press., Cambridge,U.K., pp. 881.*
Jackson, C. (1999) *Sensitivity of Stationary Wave Amplitude to regional Changes in Laurentide Ice Sheet Topography. Mechanisms of Global Climate Change at Millennial Time Scales. Geophysical Monography 112. American Geophysical Union.*
Jeffreys, H. (1926) *On the dynamics of geostrophic winds. Quat. J. Roy. Met. Soc. 52, 85-104.*
Joussane, S., Taylor, K. E. (1995) *Status of the Paleoclimate Modelling Intercomparison Project. In: Proceedings of the first international AMIP scientific conference WCRP-95 425-430 Monterey, USA.*
Justino, F., Timmermann, A., Merkel, U., Souza, E. (2004) *Synoptic reorganization of atmospheric flow during the Last Glacial Maximum. Submitted to J. Climate.*
Kapsner,W. R., Alley, R., Shuman, B., Anandakrishnan, C.A., Grootes, P. M. (1995) *Dominant influence of atmospheric circulation on snow accumulation in Greenland over the past 18000 years. Nature, 373,52-54.*
Kerr, R. (1995) *Chilly ice-age tropics could signal climate sensitivity. Science, 267, 961.*
Kim, S.J., Flato, G.M., Boer, G.J. (2003) *A coupled climate model simulation of the Last Glacial Maximum , Part 2: approach to equilibrium. Clim. Dyn. 20, 635-661.*
Kitoh, A., Murakami S., and Koide, H. (2001)*: A simulation of the Last Glacial Maximum with a coupled atmosphere-ocean GCM. Geophys. Res. Lett., 28, 2221-2224.*
Kitoh, A. Mountain uplift and surface temperature changes (1997). *Geoph. Res. Lett., 24, 2, 185-188.*
Klinger, B., McCreary, J., Kleeman, R. (2002) *The relationship between oscillating subtropical wind stress and equatorial temperature. J. Phys. Oceanogr., 32, 1507-1521.*
Knorr, G., Lohmann, G. (2003) *Southern Ocean Origin for Resumption of Atlantic Thermohaline Circulation during Deglaciation. Nature, 424, 532-536.*
Knutti R., Stocker, T. (2002) *Limited Predictability of the Future Thermohaline Circulation Close to an Instability Threshold. J. Climate, 15, 197-186.*
Kohfeld, K., Harrison, S. (2000) *How well can we simulate past climates? Evaluating the models using palaeoenvironmental datasets. Quat. Sci. Rev. 19, 321-346.*
Kotilainen, A.T., Shackleton, N.J. (1995) *Rapid climate variability in the North Pacific Ocean during the past 95,000 years. Nature, 377, 323-326.*
Kuo, H.L. (1956) *Forced and free meridional circulations in the atmosphere. J. Meteor. 13: 561-568.*
Labeyrie, L., Maslin, M., Pflaumann, U., and Schulz, H. (1995) *Variations in Atlantic surface ocean paleoceanography, 50°-80°N: A time-slice record of the last 30,000 years. Paleoceanography,*

10: 1063-1094.

Lang, C., Leuenberger,M., Schwander, J., Johnsen, J. (1999) *16° C rapid temperature variation in central Greenland 70000 years ago. Science, 286, 934-937.*

Lau N. C., Nath, M. J., (1996) *The role of the "Atmospheric Bridge" in linking tropical Pacific ENSO events to extratropical SST anomalies, J. Climate, 9, 2036-2057.*

Lea, D.W., Boyle, E.A. (1990) *Foraminiferal reconstruction of barium distribution in water masses of the glacial ocean. Paleoceanography, 5, 719-742.*

Lee, K.E., Slowey, N.C. (1999) *Cool surface waters of the subtropical North Pacific during the last glacial. Nature 397:512-514.*

Levis, S., Foley, J.A., Pollard, D. (1999) *CO_2 climate, and vegetation feedbacks at the Last Glacial Maximum. J. Geophys. Res. 104, D24, 31,191-31,198.*

Lindzen, R.S., Farrell, B. (1980) *A simple approximate result for maximum growth rate of baroclinic instabilities. J. Atmos. Sci., 37:1648-1654.*

Liu, Z., Philander, S. (1995) *How different wind stress pattern affect the tropical-subtropical circulations of the upper ocean. J. Phys. Oceanogr., 25, 449-462.*

Lorenz, E.N. (1967) *The Nature and Theory of the General Circulation of the Atmosphere. World Meteorological Organization, Geneva.*

Lorenz, E.N. (1960) *Energy and numerical weather prediction. Tellus, 12, 364-373.*

Lowell, T. V., Heusser, C. J., Andersen, B. G., Moreno, P. I., Hauser, A., Denton, G. H., Heusser, L. E., Schluchter, C.,. Marchant, D. R. (1995) *Interhemispheric symmetry of paleoclimatic events during the last glaciation, Science.*

Lyle, M., Prahl, F.G., and Sparrow, M.A. (1992) *Upwelling and productivity changes inferred from a temperature record in the central equatorial Pacific. Nature, 355:812-815.*

MacAyeal, D.R. (1993a) *Binge/Purge oscillations of the Laurentide Ice Sheet as a cause of the North Atlantic's Heinrich events. Paleoceanography, 8, 775-784.*

MacAyeal, D.R. (1993b) *A tutorial on the use of Control methods in ice-sheet modelling. Journal of Glaciology, 39, 91-98.*

MacDonald, A.M. (1998) *The global ocean circulation: A hydrographic estimate and regional analysis. Progress in Oceanogr., Vol. 41, Pergamom, 281-382.*

Malmgren, B.A., Kucera, M., Waelbroek, C., Nyberg J. (2001) *Comparison of statistical and artificial neural network techniques for estimating past sea-surface temperatures from planktonic foraminifer census data. Paleoceanography, 16, 520-530.*

Manabe, S., Stouffer, R.J. (1997) *Coupled ocean-atmosphere model response to freshwater input: comparison to Younger Dryas event, Paleocenography, 12, 321-336.*

Manabe, S., Stouffer, R.J. (1995) *Simulation of abrupt climate change induced by freshwater input to the North Atlantic Ocean. Nature, 378, 165-167*

Manabe, S., Stouffer, R.J. (1993) *Century-scale effects of increased atmospheric CO_2 on the ocean-atmosphere system. Nature, 364, 215-218.*

Manabe, S., Broccoli, A.J. (1985) *The influence of continental ice sheets on the climate of an ice age. J. Geophys. Res., 90(D1), 2167-2190.*

Marotzke, J. (1997) *Boundary mixing and the dynamics of three-dimensional thermohaline circulations. Journal of Physical Oceanography, 27, 1713-1728.*

Marshall, S.J., Clarke, K.C. (1999) *Modeling North American Freshwater Runoff through the Last Glacial Cycle. Quaternary Research, 52, 300-315.*

Marshall, S.J., Molteni, F. (1993) *Toward a dynamic understanding of planetary-scale flow regimes. J. Atmos. Sci., 50, 1792-1818.*

Maslin, M.A. , Seidov, D., Lowe, J. (2001) *Synthesis of the nature and causes of sudden climate transitions during the Quaternary In: The Oceans and Rapid Climate Change: Past, Present and Future (eds. Seidov, Haupt, and Maslin) AGU Geophysical Monograph Vol., 126, 9-52.*

McCave, I.N., Manighetti, B. and Beveridge, N.A.S. (1995) *Changes in circulation of the North Atlantic during the last 25,000 years inferred from grain-size measurements. Nature, 374:149-152.*

McFarlane, N.A., Boer, G.J.; Blanchet, J.-P.; Lazare, M., J. (1992) *The Canadian Climate Centre Second General Circulation Model and Its Equilibrium Climate. J. Clim., 5(10): 101324.*

McCreary, J., Lu, P. (1984) *Interaction between the subtropical and the equatorial ocean circulations: The subtropical cell. J. Phys. Oceanogr., 24, 466-497.*
McManus, J., Oppo D.W., Cullen, J.L. (1999) *A 0.5 Million-Year Record of Millennial scale climate variability in the North Atlantic. Science, 283, 971-975.*
Merkel, U. (2003) *ENSO Teleconnections in High Resolution AGCM Experiments. Ph.D. Thesis, Max-Planck-Institut Für Meteorology. Examensarbeit Nr. 93.*
Mikolajewicz, U., T.J. Crowley, A. Schiller and R. Voss, (1997) *Modelling teleconnection between the North Atlantic and North Pacific during the Dryas event, Nature, 387, 384-387.*
Miller, J.R., Russell, G.L. (1989) *Ocean Heat Transport during the Last Glacial Maximum. Paleoceanography, 4, 2, 141-155.*
Molina-Cruz, A. (1977) *The relation of the southern trade winds to upwelling process during the last 75,000 years. Quater. Res. 8 324-338.*
Munk, W., Wunsch, C. (1998) *Abyssal Recipes II. Deep Sea Res., 45, 1976-2009.*
Murray, J. (1887) *On the distribution of pelagic foraminifer at the surface and on the floor of the ocean. Nat. Sci. (Ecology) 11, 17-27.*
Mysak, L.A., Venegas, S.A. (1998) *Decadal climate oscillations in the Arctic: a new feedback loop for atmosphere-ice-ocean interactions. Geop. Res. Lett. 25, 3607-3610.*
NCEP Reanalysis data provided by the NOAA-CIRES Climate Diagnostics Center, Boulder, Colorado, USA, from the http://www.cdc.noaa.gov/
Neftel, A., Oeschger, H., Schwander, J., Stauffer, B., Zumbrunn R. (1982) Ice core measurements give atmospheric CO_2 content during the past 40,000 yr. Nature 295:220-23.
Oeschger, H., Beer, J., Siegenthaler, U., and Stauffer, B. (1984) Late glacial climate history from ice cores. In Hansen, J. E., and Takahashi, T. (Eds.) *Climate Processes and Climate Sensitivity (Maurice Ewing Series, No. 5): 299306. American Geophysical Union, Washington, D.C.*
Oka, A., Hasumi, H., Suginohara, N. (2001) *Stabilisation of thermohaline circulation by wind-driven and vertical diffusive salt transport. Clim. Dyn. 18:71-83.*
Opsteegh, J.D., Haarsma, R.J., Selten, F.M. Kattenberg, A. Kattenberg. (1998) *ECBilt, a dynamic alternative to mixed boundary conditions in ocean models. Tellus, 50A,348-367.*
Paciorek, C., Risbey, J. S., Ventura, V. Roses, R. D. (2002) *Multiple Indices of Northern Cyclone Activity, Winter 1949-1999. J. Climate, 15:1573-1589.*
Palmer , T. N. (1999) *A nonlinear dynamical perspective on climate prediction. J. Climate, 12, 575-591.*
Peixoto, J.P., Oort, A.H. (1992) *Physics of Climate, Spring-Verlag New York, Inc. 520 pgs.*
Paillard, D., Labeyrie, L., (1994) *Role of the thermohaline circulation in the abrupt climate warming after Heinrich events: Nature, v. 372, p. 162-164.*
Peltier, W.R. (2004) *Global glacial isostasy and the surface of the ice-age Earth: the ICE-5G (VM2) model and GRACE. Annual Review of Earth and Planetary Sciences, Vol 32, 111-149.*
Peltier, W.R., Shennan, I., Drummond, R., Horton, B. (2002) *On the postglacial isostatic adjustment of the British Isles and the shallow viscoelastic structure of the Earth. Geophys. J. Int. 148,443-475.*
Peltier, W.R. (1994) *Time Dependent Topography Through the Glacial Cycle: IGBP PAGES/World Data Center-A for Paleoclimatology Data Contribution Series 93-015, NOAA/NGDC Paleoclimatology Program, Boulder CO, USA.*
Peltier, W.R., Hyde, W. (1984) *A model of the ice age cycle. Milankovitch and Climate, Understanding the Response to Orbital Forcing, A. Berger, J. Imbrie, J. Hays, G. Kukla, and B. Saltzman, Eds. NATO ASI Series C, Vol. 126, Reidel, 895 pp.*
Peterson, L.C., Haug G.H., Hughen, K.A., Röhl, U. (2000) *Rapid changes in marine and terrestrial climate in the tropical Atlantic during the last glacial. Science 290, 1947-1951.*
Peterson, R.G and Stramma, L (1991) *Upper-level circulation in the South Atlantic Ocean. Progress in Oceanogr., 26, 1-73.*
Peyron, O., Guiot, J., Cheddadi, R., Tarasov, P., Reille, M., de Beaulieu, J-L., Bottema, S., Andrieu, V., (1998) *Climatic reconstruction in Europe for 18,000 yr BP from pollen data. Quat. Res. 49:183-196.*

Philander, S. G. H. (1985) *Tropical oceanography. Advances in Geophysics, 28A, 461-477.*
Pinot, O., Ramstein, G., Harrison, S.P., Prentice, I.C., Guiot, J., Stute, M., Joussaume ,S. (1999) *Tropical paleoclimate at the last glacial maximum: comparison of paleoclimate modeling Intercomparison project (PMIP) simulations and paleodata. Clim. Dyn. 15: 857-874.*
Polzin, K.L., Toole, J.M., Ledwell, J.R., Schmitt, R.W. (1997) *Spacial variability of turbulent mixing in the ocean. Science, 276, 93-96.*
Porter, S.C. (1979) *Hawaiian glacial climates. Quat. Res. 12:161-187.*
Prentice, I.C., Cramer, W., Harrison, S.P., Leemans, R., Monserud, R.A. and A.M. Solomon (1992). *A global biome model based on plant physiology and dominance, soil properties, and climate. J. Biogeogr., 19, 117-134.*
Rahmstorf, S. (1994) *Rapid climate transitions in a coupled ocean-atmosphere model. Nature, 372, 82-85.*
Richardson, P.L. e Walsh, D., (1986) *Mapping Climatological Variations of Surface Currents in the tropical Atlantic using Drifts. J. Geophys. Res., vol. 91, C9, 10437-10450.*
Rind, D. (1987) *Components of the ice age circulation. J. Geophys. Res. , 92(D4):4241-4281.*
Rind, D., Peteet, D. (1985) *Terrestrial conditions at the last glacial maximum and CLIMAP sea-surface temperature estimates, Are they consistent? Quat. Res. 24:1-22.*
Rostek, F., G. Ruhland, G., F. Bassinot, F., P.J. Müller, P.J., Labeyrie, L., Lancelot, Y., Bard, E. (1993) *Reconstructing sea surface temperature and salinity using d18O and alkenone records. Nature, 364, 319-321.*
Sakai, K., Peltier, W.R. (1999) *A Dynamical Model of the Dansgaard-Oeschger Oscillation and the Origin of the Bond Cycles. J. Climate, 12, 2238-2255.*
Saltzman, B. (1983) *Climate system Analysis. Adv. Geophys. 25, 173-233.*
Sarnthein, M., Gersonde, R., Nieder, S., Pflaumann, U., Spielhagen, R., Thiede, J., Wefer, G., Weinelt, M. (2003) *Overview of Glacial Atlantic Ocean Mapping (GLAMAP 2000), Paleoceanography, 18(2), 1030.*
Sarnthein, M., Stattegger, K., Dreger, D., Erlenkeuser, H., Grootes, P., Haupt, B. J., Jung, S., Kiefer, T., Kuhnt, W., Pflaumann, U., Schäfer-Neth, C., Schulz, H., Schulz, M., Seidov, D., Simstich, J., van Kreveld, S., Vogelsang, E., Völker, A. and Weinelt, M. (2001) *Fundamental modes and abrupt changes in North Atlantic circulation and climate over the last 60 ky - Concepts, reconstructions and numerical modeling. In: Schäfer, P., Ritzrau, W., Schlüter, M. and Thiede, J. (eds.), The Northern North Atlantic: A changing environment. Springer Verlag, Berlin, 365-410.*
Sarnthein, M. Jansen, E., Weinelt, M., et al. (1995) *Variations in Atlantic surface ocean paleoceanography, 50-85°N: a time-slice record of the last 55000 years. Paleoceanography, 10: 1063-1094.*
Sarnthein, M., Tetzlaff, G., Koopman, B., Wolter, K., Pflaumann, U. (1981) *Glacial and interglacial wind regimes over the eastern subtropical Atlantic and North-west Africa. Nature, 293, 193-196.*
Schäfer-Neth, C. and A. Paul (2003) *Gridded Global LGM SST and Salinity Reconstruction, IGBP PAGES/World Data Center for Paleoclimatology, Boulder Data Contribution Series 2003-046. NOAA/NGDC Paleoclimatology Program, Boulder CO, USA.*
Schiller, A., Mikolajewicz, U., Voss, R. (1997) *The stability of the North Atlantic thermohaline circulation in a coupled ocean-atmosphere general circulation model. Clim. Dyn. 13:325-347.*
Schmitt, R.W., Bogden, P.S., Dorman, C.E. (1989) *Evaporation minus precipitation and density flux for the North Atlantic. J. Phys. Oceanogr., 19,1208-1221.*
Schneider, R.R., Müller, P.J., Ruhland, G., Meinecke, G., Schmidt, H., Wefer, G. (1996) *Late Quaternary surface temperatures and productivity in east-equatorial South Atlantic: Response to changes in trade/monsoon wind forcing and surface water advection, 1996. In: The South Atlantic: Present and Past Circulation, G. Wefer, W.H. Berger, G. Siedler and D. Webb (eds.), Springer-Verlag, Berlin , pp. 527-551.*
Schott, F., Visbeck, M., Send, U., Stramma, L., Desaubies, Y. (1996) *Observations of deep convection in the Gulf of Lions, northern Mediterranean, during the winter of 1991/1992. J. Phys. Oceanogr. 26, 505-524.*
Schott, F., Visbeck, M., Fischer, J. (1993) *Observations of vertical currents and convection in*

the central Greenland Sea during winter 1988/1989. J. Geophy. Res. 98, 14401-14421.
Schulz, H. von Rad, U., Erlenkeuser, H. (1998) *Correlation between Arabian Sea and Greenland climate oscillations of the past 111,000 years. Nature, 393, 54-57.*
Schulz, M., Timmermann, A., Paul, A. (2002) *On the 1470-year pacing of Dansgaard-Oeschger warm events. Paleoceanogr., 17 (3), 10.1029/2000PA000571.*
Seidov, D., Barron, E., Haupt, B.J. (2001) *Meltwater and the global conveyor: northern versus southern connections, Global Planetary Change, 30, 257-270.*
Seidov, D, Maslin, M.A. (2001) *"Atlantic Ocean heat piracy and the bipolar climate seesaw during Heinrich and Dansgaard-Oeschger events" J. Quatern. Sci., 16, 321-328.*
Shin,S.I., Liu, Z. Otto-Bliesner B., Brady, E.C., Kutzbach, J.E., Harrison, S.P. (2003) *Simulation of the Last Glacial Maximum climate using the NCAR-CCSM. Cli. Dyn., 20:127-151.*
Shin, S.-I., Liu, Z., Otto-Bliesner, B.L., Kutzbach, J.E. Vavrus, S.J., (2003b) *Southern Ocean sea -ice control of the glacial North Atlantic thermohaline circulation. Geo. Res. Lett. 30(2), 1096, doi:10.1029/2002GL015513.*
Sikes, E.L. Keigwin, L.D. (1994) *Equatorial Atlantic sea surface temperature for the last 30 kyr: A comparison of Uk_{36}, δO^{18} and foraminiferal assemblage temperature estimates, Paleoceanography, 9, 31-45.*
Silveira, I.C.A., Miranda, L. B., Brown, W. S. (1994) *On the origins of the North Brazil Current. J. Geophys. Res., 98, 14,353-14,368.*
Speer, K., Tziperman, E. (1992) *Rates of water mass formation in the North Atlantic Ocean. J. of Physical Oceanography, 22, 94-104.*
Steinglitz, J.L., Curry, W.B., Slowey, N. (1999) *Weaker Gulf Stream in the Florida Straits during the Last Glacial Maximum. Nature, 402, 644-648.*
Stendel, M., Roeckner, E. (1998) *Impacts of horizontal model resolution on simulated climate statistics in echam. Report 253, Max-Planck Institue of Meteorology.*
Stocker, T.F. (1998) *The seesaw effect. Science, 282, 61-62.*
Stocker, T.F., Schmittner, A. (1997) *Influence of CO_2 emission rates on the stability of the thermohaline circulation. Nature, 388, 962-865.*
Stommel, H. (1961) *Thermohaline convection with two stable regimes of flow. Tellus, 13, 224-230.*
Street-Perrott, F.A. , Harrison, S.P. (1985), *Lake levels and climate reconstruction, p 291-340. A. D. Hecht, ed., Paleoclimatic Analysis and Modeling. John Wiley, Chichester, 445 p.*
Stute, M., Forster, M., Frischkorn, H., Serejo, A. Clark, F.j., Schlosser, P. Broecker, W. S., G. Bonani (1995) *Cooling of tropical Brazil (5° C) during the last glacial maximum. Science 269, 379-383.*
Suarez, M. J., Held, I. M.(1979) *The sensitivity of an energy balance climate model to variations in the orbital parameters. J. Geophys. Res., 84(C8), 4825-4836.*
Talley, D.L., Reid, L.J., Robbins, E.P. (2003) *Data-Based Meridional Overturning Streamfunctions for the Global Ocean. J. Climate, 16, 3213-3226.*
Tarasov, L., Peltier, W.R. (2002) *Greenland glacial history and local geodynamic consequences. Geophys. J. Int. 150, 198-229.*
Tarasov P.E., Peyron, O., Guiot, J., Brewer, S., Volkova, V.S., Bezusko, L.G., Dorofeyuk, N.I., Kvavadze, E.V., Osipova, I.M., Panova, N.K. (1999) *Last Glacial Maximum climate of the former Soviet Union and Mongolia reconstruction from pollen and plant macrofossil data. Clim. Dyn. 15:227-240.*
Thompson, L.G., Mosley-Thompson, E., Mulvaney, R., Davis, M.E., Lin, P.-N., Henderson, K.A., Cole-Dai, J.,Bolzan, J.F., Liu,K.-b. (1995) *Late Glacial Stage and Holocene tropical ice core records from Huascaran, Peru, Science, 269, 46-50.*
Timmermann, A., Justino, F., Jin, F. F., Krebs, U., Goosse, H. (2004, in press) *Surface temperature control in the North and tropical Pacific during the last glacial maximum. Clim. Dyn.*
Timmermann, A., Goosse, H. (2004b) *Is the wind stress forcing essential for the meridional overturning circulation. Geophys. Res. Lett.,31, L04303, doi: 10.1029/2003GL01877.*
Timmermann, A., Schulz, M., Gildor, H., Tziperman, E. (2003) *Coherent Resonant millenial-scale climate transitions triggered by massive meltwater pulses. J. Climate, 16, 2569-2585.*
Trenberth, K., Caron, J.M. (2001) *Estimates of Meridional Atmosphere and Ocean Heat Trans-*

ports J. Climate 14: 3433-3443.

Trenberth, K. (1991) *Storm Tracks in the Southern Hemisphere. J. Atmos. Sci., vol.48, n.19, 2151-2178.*

Veum, T., Jansen, E., Arnold, M., Beyer, I., Duplessy, J. C. (1992) *Water mass exchange between the North Atlantic and the Norwegian Sea during the past 28,000 years. Nature. 356, 783-785 1992.*

Van Kreveld, S., Sarnthein, M., Erlenkeuser, H., Grootes, P., Jung, S., Nadeau, M.J., Pflaumann, U. , Voelker, A. (2000) *Potential links between surging ice sheets, circulation changes, and the Dansgaard-Oeschger cycles in the Irminger Sea, 60-18 kyr. Paleoceanography 15: 425-442.*

Visbeck, M., Fischer, J., Schott, F. (1995) *Preconditioning the Greenland Sea for deep convection: Ice formation and ice drift. J. Geophys. Res., 100, 18489-18502.*

Xie, S., Liu, T.W., Liu, Q., Nonaka, M. (2001) *Far-Reaching Effects of the Hawaiian Islands on the Pacific Ocean-Atmosphere System. Science, 292, 2057-2060.*

Waelbroeck, C., Labeyrie, L., Duplessy, J.-C., Guiot, J., Labracherie, M., Leclaire, H., Duprat, J. (1998) *Improving past sea surface temperature estimates based on planktonic fossil fauna. Paleoceanography, 13, 272-283.*

Wallace, L., Lau, N.,-C (1985) *On the role of barotropic energy conversion in the general circulation. Advances in Geophysics, A28, 33-74.*

Wang, P. (1999) *Response of Western Pacific marginal seas to glacial cycles: paleoceanographic and sedimentological features. Mar. Geol., 156:5-39.*

Weaver, A.J., Saenko, A., Clark, P.U., Mitrovica, J.X. (2003) *Meltwater pulse 1A from Antarctica as a trigger of the Bølling-Allerød warm interval. Science, 299, 1709-1713.*

Weaver, A.J., Eby, M., Wiebe, E. C., Bitz, C. M. , Duffy, P.B. , Ewen, T. L., Fanning, A. F., Holland, M.M., MacFadyen, A., Matthews, H.D., Meissner, K.J., Saenko, O., Schmittner, A., Wang, H. Yoshimori, M. (2001) *The UVic Earth System Climate Model: Model Description, Climatology and Applications to Past, Present and Future Climates. Atmosphere-Ocean, 39(4), 361-428.*

Weaver, A.J., Eby, M., Fanning, A. F.,Wiebe, E. C. (1998) *Simulated influence of carbon dioxide, orbital forcing and ice sheets on the climate of the Last Glacial maximum. Nature, 394: 84 7-853.*

Webb, R.S., Rind, D.H., Lehman, S.J., Healy, R.J., Sigman, D. (1997) *Influence of ocean heat transports on climate of the Last Glacial Maximum. Nature 385, 695-699.*

Winton, M., Sarachik, E.S. (1993) *Thermohaline Oscillations Induced by Strong Steady Salinity Forcing of Ocean General Circulation Model. J. Phys. Oceanogr., 23, 1389-1410.*

Wood, R.A., Keen, A.B., Mitchell, J.F.B., Gregory, J.M. (1999) *Changing spatial structure of the thermohaline circulation in response to atmospheric CO_2 forcing in climate model. Nature, 399, 52-55.*

Woodward, I.F. (1987) *"Climate and Plant Distribution". Cambridge Univ. Press. New York.*

Wyputta, U., McAvaney, B.J. (2001) *Influence of vegetation changes during the LastGlacial Maximum using the BMRC atmospheric general circulation model. Clim. Dyn., 17(12), 923-932, 2001.*

7. LIST OF ACRONYMS

AABW - Antarctic Botton Water
ALB - Albedo Modeling Experiment
AGCM - Atmospheric General Circulation Model
AOGCM - Atmospheric-Ocean General Circulation Model
BP - 1,000 years Before Present
CGCM - Coupled Global Climate Models
CLD - Convective Layer Depth
CLIMAP - Climate: Long-range Investigation, Mapping and Prediction
COADS - Comprehensive Ocean-Atmospheric Data Set
CO2 - CO_2 Modeling Experiment
CTR - Control Climate Simulation
DJF - December-January-February
D-O - Dansgaard-Oeschger Cycle
EKE - Eddy Kinetic Energy
EMIC - Earth Model of Intermediate Complexity
GLAMAP - Glacial Atlantic Ocean Mapping
$\mathbf{H}_{Atm}$ - Atmospheric meridional heat transport
$\mathbf{H}_{Oce}$ - Oceanic meridional heat transport
$\mathbf{H}_{total}$ - Total meridional heat transport
IPCC - Intergovernmental Panel on Climate Change
JJA - June-July-August
kyr - 1000 years before present
LCDW - Lower Circumpolar Deep Water
LGM - Last Glacial Maximum
LGM - Last Glacial Maximum Experiment
NADW - North Atlantic Deep Water
NCEP - National Center for Environmental Prediction
NH - Northern Hemisphere
ORB - Orbital Parameters Modeling Experiment
SH - Southern Hemisphere
SSS - Sea Surface Salinity
SST - Sea Surface Temperature
THC - Thermohaline Circulation
TOPO - Topography Modeling Experiment
YD - Younger Dryas